

NAVAL POSTGRADUATE SCHOOL Monterey, California



19980727 178

THESIS

**IDENTIFICATION OF RANDOM LOADS IMPINGING
ON THE RAH-66 COMANCHE HELICOPTER
EMPENNAGE USING SPECTRAL ANALYSIS**

by

Patrick H. Mason

June 1998

Thesis Co-Advisors:

E. Roberts Wood
Donald A. Danielson
Joshua H. Gordis

Approved for public release; distribution is unlimited.

REPORT DOCUMENTATION PAGE

Form Approved OMB No. 0704-0188

Public reporting burden for this collection of information is estimated to average 1 hour per response, including the time for reviewing instruction, searching existing data sources, gathering and maintaining the data needed, and completing and reviewing the collection of information. Send comments regarding this burden estimate or any other aspect of this collection of information, including suggestions for reducing this burden, to Washington Headquarters Services, Directorate for Information Operations and Reports, 1215 Jefferson Davis Highway, Suite 1204, Arlington, VA 22202-4302, and to the Office of Management and Budget, Paperwork Reduction Project (0704-0188) Washington DC 20503.

1. AGENCY USE ONLY <i>(Leave blank)</i>	2. REPORT DATE June 1998	3. REPORT TYPE AND DATES COVERED Master's Thesis	
4. IDENTIFICATION OF RANDOM LOADS IMPINGING ON THE RAH-66 COMANCHE HELICOPTER EMPENNAGE USING SPECTRAL ANALYSIS		5. FUNDING NUMBERS	
6. AUTHOR(S) Mason, Patrick H.		8. PERFORMING ORGANIZATION REPORT NUMBER	
7. PERFORMING ORGANIZATION NAME(S) AND ADDRESS(ES) Naval Postgraduate School Monterey CA 93943-5000		10. SPONSORING/MONITORING AGENCY REPORT NUMBER	
9. SPONSORING/MONITORING AGENCY NAME(S) AND ADDRESS(ES)		11. SUPPLEMENTARY NOTES The views expressed in this thesis are those of the author and do not reflect the official policy or position of the Department of Defense or the U.S. Government.	
12a. DISTRIBUTION/AVAILABILITY STATEMENT Approved for public release; distribution is unlimited.		12b. DISTRIBUTION CODE	
12. ABSTRACT <i>(maximum 200 words)</i> The Army RAH-66 Comanche Helicopter is currently undergoing developmental flight testing. The empennage of the aircraft is experiencing buffeting where the horizontal and vertical tail vibrate at resonant frequencies. These high buffet loads are manifested in higher than anticipated fitting loads, particularly on the tail, and vibrations in the crew stations and at the nose cone where the targeting sensors are located. Significant effort has been devoted to identifying the sources of excitation and the nature of the structural response. This thesis determines the location and magnitude of empennage vibratory airloads. Because the nature of the excitation is a random function, spectral analysis is used. To obtain the loads, a three step process was utilized. First, from aircraft differential pressure transducers and accelerometers, the spectral content of the response and excitation was determined. Then, using a NASTRAN model modified to replicate the flight test aircraft, frequency response functions were determined between selected points on the aircraft's tail and the accelerometers. Finally, using this information, a solution was obtained for the vibratory airloads. Having provided information on the nature of the driving forces, structural modifications can be made that move the natural frequencies away from the frequencies of the applied airloads.			
14. SUBJECT TERMS: RAH-66 Comanche Helicopter, Random Vibrations, Comanche Tail Section, Structural Analysis, Spectral Analysis, NASTRAN Analysis		15. NUMBER OF PAGES 155	
17. SECURITY CLASSIFICATION OF REPORT Unclassified		16. PRICE CODE	
18. SECURITY CLASSIFICATION OF THIS PAGE Unclassified	19. SECURITY CLASSIFICATION OF ABSTRACT Unclassified	20. LIMITATION OF ABSTRACT UL	

Approved for public release; distribution is unlimited.

IDENTIFICATION OF RANDOM LOADS IMPINGING ON THE RAH-66
COMANCHE HELICOPTER EMPENNAGE USING SPECTRAL ANALYSIS

Patrick H. Mason
Major, United States Army
B.S., Georgia Institute of Technology, 1986

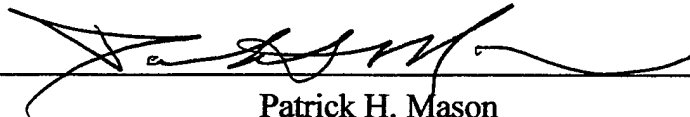
Submitted in partial fulfillment
of the requirements for the degree of

MASTER OF SCIENCE IN AERONAUTICAL ENGINEERING

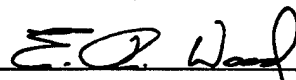
from the

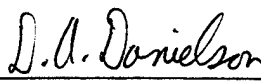
NAVAL POSTGRADUATE SCHOOL
June 1998

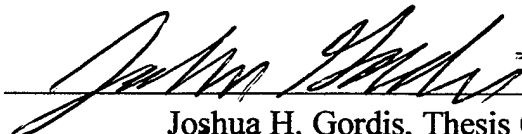
Author:


Patrick H. Mason

Approved by:


E. Roberts Wood, Thesis Co-Advisor


Donald A. Danielson, Thesis Co-Advisor


Joshua H. Gordis, Thesis Co-Advisor


Gerald H. Lindsey, Chairman
Department of Aeronautics and Astronautics

ABSTRACT

The Army RAH-66 Comanche Helicopter is currently undergoing developmental flight testing. The empennage of the aircraft is experiencing buffeting where the horizontal and vertical tail vibrate at resonant frequencies. These high buffet loads are manifested in higher than anticipated fitting loads, particularly on the tail, and vibrations in the crew stations and at the nose cone where the targeting sensors are located. Significant effort has been devoted to identifying the sources of excitation and the nature of the structural response. This thesis determines the location and magnitude of empennage vibratory airloads. Because the nature of the excitation is a random function, spectral analysis is used. To obtain the loads, a three step process was utilized. First, from aircraft differential pressure transducers and accelerometers, the spectral content of the response and excitation was determined. Then, using a NASTRAN model modified to replicate the flight test aircraft, frequency response functions were determined between selected points on the aircraft's tail and the accelerometers. Finally, using this information, a solution was obtained for the vibratory airloads. Having provided information on the nature of the driving forces, structural modifications can be made that move the natural frequencies away from the frequencies of the applied airloads.

TABLE OF CONTENTS

I. INTRODUCTION	1
A. GENERAL	1
B. PROBLEM DEFINITION	3
II. HELICOPTER VIBRATIONS	5
A. GENERAL	5
1. Vibrations at Integral Multiples of Rotor Speed	5
2. Random Aerodynamic Excitation	7
3. Self-Excited Vibrations	8
B. VIBRATION SPECIFICATIONS	8
C. COMANCHE VIBRATION SOURCES	11
1. Main Rotor Hub Forces and Moments	11
2. Aerodynamic Excitation	13
III. SPECTRAL ANALYSIS	19
A. TIME AVERAGING	19
B. FREQUENCY DOMAIN ANALYSIS	22
C. DIGITAL SIGNAL PROCESSING	26
IV. FLIGHT TEST DATA ANALYSIS	33
A. ACCELEROMETERS	33
B. FLIGHT TEST PRESSURE MEASUREMENTS	60
V. STRUCTURAL DYNAMICS	67
A. SINGLE DEGREE OF FREEDOM (SDOF) OSCILLATORS	67
B. MODAL ANALYSIS	71
C. RIGID BODY MODES	74
D. FINITE ELEMENT MODELING	74
VI. RAH-66 NASTRAN ANALYSIS	77
A. NATURAL FREQUENCIES	77
B. MODE SHAPES	80
C. FREQUENCY RESPONSE FUNCTIONS	84
1. Horizontal Tail	85
2. Vertical Tail	90
VII. RESULTS AND ANALYSIS	95
A. SOLUTION METHOD	95
B. MATLAB® PROGRAM	98
C. RESULTS	99
D. ANALYSIS	108

VIII. CONCLUSIONS AND RECOMMENDATIONS	111
A. CONCLUSIONS	111
B. RECOMMENDATIONS.....	113
1. Correlate with Wind Tunnel Testing.....	113
2. Parameter Identification and Correlation with NASTRAN.....	113
3. Additional Airspeed Analysis.....	114
4. Structural Optimization	114
APPENDIX A: TEST FLIGHT PARAMETERS	117
APPENDIX B: PSD AND CSD PROGRAMS	119
APPENDIX C: MODE SHAPES.....	123
APPENDIX D: ACCELEROMETER LOCATIONS & NASTRAN GRIDS	135
APPENDIX E: LOAD CALCULATIONS PROGRAM.....	137
LIST OF REFERENCES.....	143
INITIAL DISTRIBUTION LIST	145

I. INTRODUCTION

A. GENERAL

The RAH-66 Comanche is the United States Army's newest light/attack armed reconnaissance helicopter. It is designed to be a combat multiplier on the joint and combined arms battlefields of the 21st century. The aircraft will be fielded to both corps and division cavalry and attack battalions/squadrons with the assigned missions of armed reconnaissance and attack, both with an embedded air to air capability. Mission profiles include day, night, reduced visibility, from ships, and in desert and non-desert environments. The aircraft is shown in Figure 1.1.

Comanche will contribute to combat effectiveness by its ability to fight for information and disrupt the enemy's tactical intelligence collection effort in the counter reconnaissance role. Key attributes of the aircraft include a five-blade bearingless main rotor, FANTAIL anti-torque system, composite materials, Low Observables (LO), an advanced pilotage and targeting system, and an integrated digital mission equipment package (MEP). These digital systems will allow it to serve as a forward data fusion center and provide near real time information to commanders at all levels.

Designed for two crew members, it is capable of being operated by a single crew member from either station. During missions, the pilot-vehicle-interface (PVI) is designed to support low workload, high situational awareness, human error resistance, and maximum mission productivity. [Ref. 1]

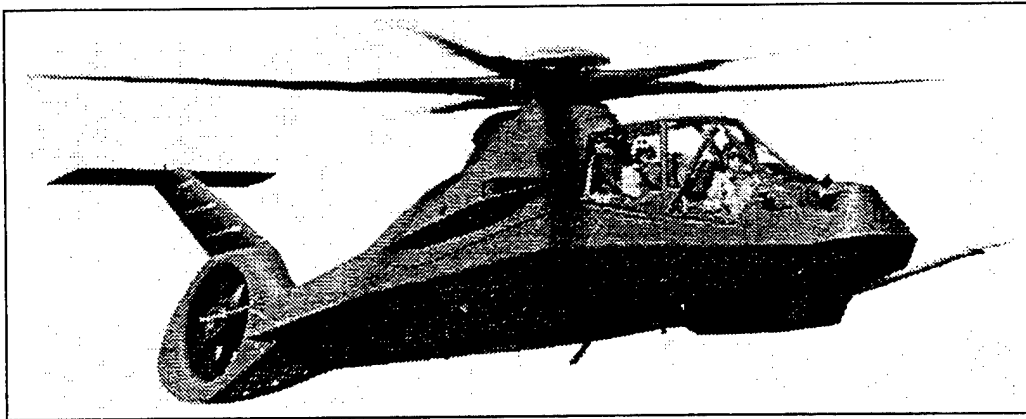


Figure 1.1: US Army RAH-66 Comanche Helicopter.

The Boeing Defense and Space Group's Helicopter Division of Philadelphia, Pennsylvania and United Technologies' Sikorsky Aircraft Division of Stratford, Connecticut were awarded the demonstration/validation (DEM/Val) phase of the contract for the Comanche. These contractors divided the aircraft into two sections for design and fabrication. Boeing has responsibility for the tail section of the aircraft. Sikorsky has responsibility for the forward portion of the aircraft fuselage, to include the integration of both sections.

Currently, the first prototype is undergoing extensive flight testing at the Sikorsky test flight facility in West Palm Beach, Florida. Focused on "envelope expansion", the aircraft had flown approximately 91 hours, reached 171 knots in forward, level flight, achieved bank angles of 45°, and sideward flight of 70 knots as of May, 1998. Prototype #2 is scheduled to begin flight testing in 1999.

B. PROBLEM DEFINITION

During flight testing the empennage of the aircraft experienced buffeting where the horizontal and vertical tail vibrated excessively in certain flight regimes. Observable from both the chase aircraft and on flight data records for strain gauges and accelerometers, these high buffet loads created higher than anticipated fitting loads, particularly in the tail region, and resulted in vibrations in the crew stations and at the nose cone where the targeting sensors are located. Significant effort has been devoted to identifying the sources of excitation and the nature of the structural response. One such method is shown in Figure 1.2. Here, strips of material were placed on the empennage to allow for better visualization of both the airflow and vibration of the structure.



Figure 1.2: Comanche Prototype Test Flight.

Boeing and Sikorsky have also conducted several wind tunnel experiments to better quantify the flow coming from the aircraft fuselage. The first was completed in April 1997 at NASA Langley. Two follow-on tests were executed at the United Technologies' Research Center in Hartford, Connecticut and then Boeing Defense and Space Group's Helicopter Division in Philadelphia, Pennsylvania. These tests consisted of changing aerodynamic surfaces to modify the flow impinging on the tail from the fuselage. Additionally, the flight test aircraft had several structural modifications to stiffen the tail section; notably a bracket to secure the horizontal and vertical tail, use of a rigid flap on the right trailing edge of the horizontal stabilizer, and the adding of tip weights to the horizontal stabilizer.

This research determines the location and magnitude of empennage loads caused by the random excitation. Because the nature of the excitation is assumed to be a random process, spectral analysis is used. To obtain the loads, a three step process is utilized. First, from aircraft differential pressure transducers and accelerometers, the spectral content of the excitation and response is determined. Then, using a NASTRAN model modified to replicate the flight test aircraft, frequency response functions are obtained between selected points on the aircraft's tail and the accelerometers. Finally, using this information, estimates of the airloads are calculated. Having provided information on the nature of the excitation, structural modifications can then be explored to reduce the response of the airframe to the excitation. Potential methods for accomplishing this may be based on shifting airframe natural frequencies, increasing structural damping, or adding vibration control devices.

II. HELICOPTER VIBRATIONS

A. GENERAL

As with all helicopters, the RAH-66 experiences vibrations. These forces can significantly impact crew effectiveness, imaging and targeting performance and airframe and equipment reliability and maintainability. With the use of complex digital avionics systems, there is a greater emphasis on vibration reduction. As such, the analysis of dynamic loads and modification of structures to create a low vibration environment is essential. The first step in reducing vibrations is to identify the source of excitation. Once that is known, the aircraft can be modified so that the structural frequencies are offset from the driving frequencies.

Helicopter vibrations fall into three categories. First, there are vibrations due to rotor excitation, which are at frequencies that are integral multiples of the rotor's rotational speed. Second, vibrations due to random aerodynamic excitation where the frequency being observed is a natural frequency of the structure being excited. And finally, self-excited vibrations, such as flutter and ground resonance. [Ref. 2]

1. Vibrations at Integral Multiples of Rotor Speed

The primary source of helicopter fuselage vibrations is the rotor system. Here, harmonics of aerodynamic loads on the blade give rise to vibratory response of the blade. Since the blade is restrained at the root, the blade responses result in root shears, which feed from the rotor head into the fuselage as vibratory shears and moments. As the forces go from the rotating to the fixed fuselage system, the rotor system tends to act as a filter.

For an N blades rotor system, the frequencies which will filter through are those at N and $2N/\text{rev}$. Since the amplitudes of the lower harmonics of blade loading are greater than the higher, the N/rev vibration of the fuselage is most critical. It can be shown that N/rev fuselage vibrations in the fixed system are the result of the $N-1$, N , and $N+1/\text{rev}$ vibratory response of the blades in the rotating system.

In addition to the N/rev or NP vibration, there are secondary excitation frequencies which also must be taken into account. Any unbalance of the rotor system, such as blades out of track, will give rise to $1/\text{rev}$ or $1P$ excitation of the fuselage. Dissymmetry of blade dampers may cause troublesome $2/\text{rev}$ excitation. Also important is the $1 \times$ tail rotor rotational speed.

Forward speed plays a critical role in vibrations. Figure 2.1 is a typical plot of the variation in vibration levels as a function of airspeed. The increase in vibrations levels in the 30 to 45 knot range can be attributed to blade vortex interaction due to the proximity of the rotor to its wake and the resulting non-uniform induced velocity field.

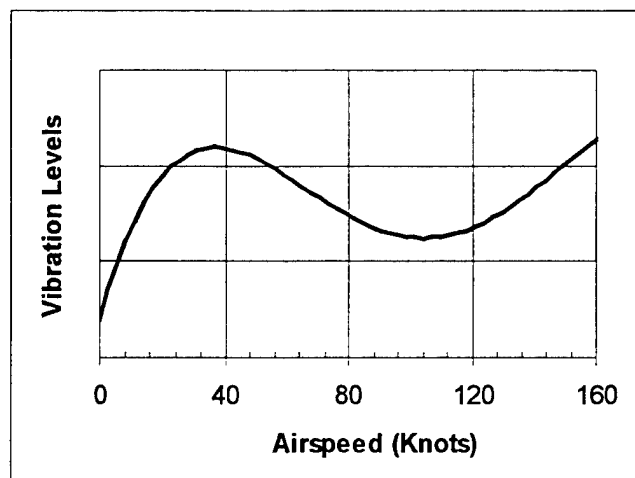


Figure 2.1: Typical Helicopter Vibration Levels Versus Airspeed. After Ref.[2].

In the high speed flight regime, the increase in vibration with increase in airspeed is attributed to two sources. First, the aerodynamic excitation due to impingement of the rotor's wake on the helicopter's horizontal empennage. Second, amplification of blade section aerodynamic loads associated with increased cyclic pitch accompanied by increasing differences in dynamic pressure per blade revolution. Figure 2.2 shows the non-distorted rotor wake geometry for both low and high forward flight speeds.

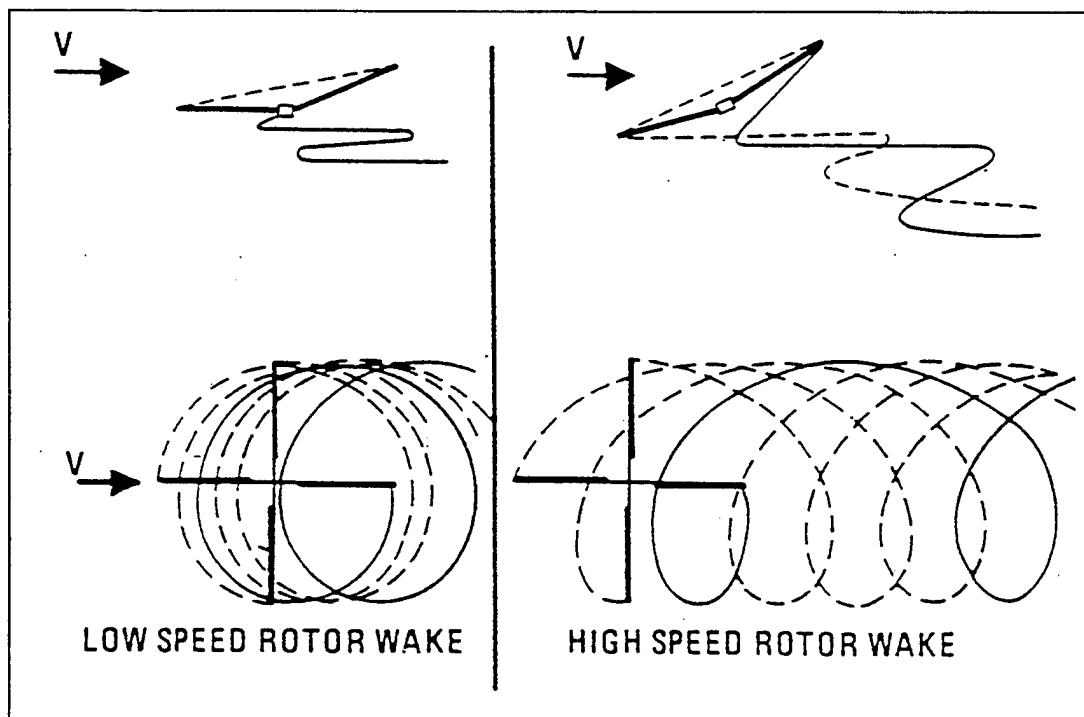


Figure 2.2: Rotor Wake Geometry. From Ref.[2].

2. Random Aerodynamic Excitation

This type of vibration is often associated with the turbulent downwash from the rotor, which impinges on the fuselage and its components. Similar to white noise, this excitation contains many harmonics that can excite fundamental fuselage or empennage modes. Often, an interesting characteristic of this type of excitation is that it is present

only within a certain range of airspeeds. Successful solutions of this problem have included modifying the structure excited and by altering the flow from the rotor.

3. Self-Excited Vibrations

A self-excited vibration is one that results in divergent oscillations where the system damping is negative. In the case of negative damping, the damping force, which is now a driving force, does positive work on the system. The work done by this force is converted into the additional kinetic energy of the increased vibration. A self-excited vibration cannot exist without an external source of energy. In the case of flutter, the airflow provides the source of energy.

B. VIBRATION SPECIFICATIONS

Vibration specifications for Army aircraft are governed by Aeronautical Design Standard (ADS) – 27 and MIL-STD-810D [Ref. 1]. Human factors vibration requirements are expressed by ADS-27 in terms of an intrusion index which is the square root of a weighted sum of squares of four vibration components in each direction. The purpose of this is to bring together the twelve most significant crew vibration components into a single number for evaluation. A separate specification exists to capture the lower frequency one per main rotor revolution, or 1P, vibration.

The changes in vibrations that result for airspeed and maneuvering are addressed in ADS-27 by defining limits in terms of flight regions. There are three defined regions, with the first being normal flight up to cruise speed, then maneuvers having a duration less than 3 seconds, and lastly maneuvers having a duration greater than 3 seconds. There is also a

region for gunfire vibration. The specifications for the RAH-66 crew seat are listed in the Performance Weapon System Specification [Ref. 1] and are shown in Table 2.1.

Additionally, Figures 2.3 and 2.4 display the currently measured intrusion index in the Pilot's and Copilot's crew station versus the specification.

	Intrusion Index	MR1P (in/sec)
Flight Region I	1.2	.15
Flight Region II	3.0	.30
Flight Region III	4.0	.40
Weapons Firing Increment	+2.0	N/A

Table 2.1: Crew Seat Intrusion Index and MR1P Vibration Limits.

Because of the frequency bands that are used to calculate the intrusion index, any random, broad band, excitation occurring between main rotor 1P and NP is not totally captured. Therefore, the intrusion index does not indicate the contribution of the broad band excitation to total response.

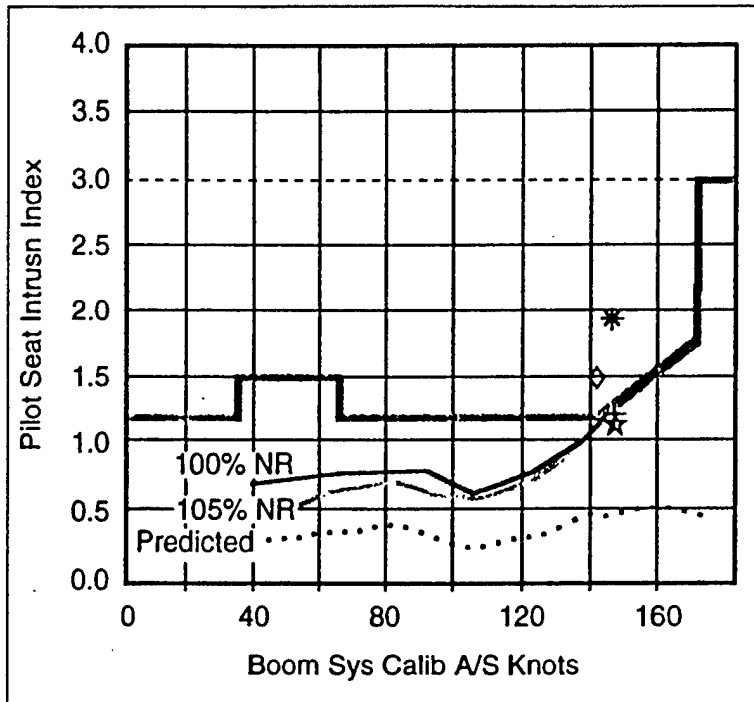


Figure 2.3: Intrusion Index – Pilot’s Station.

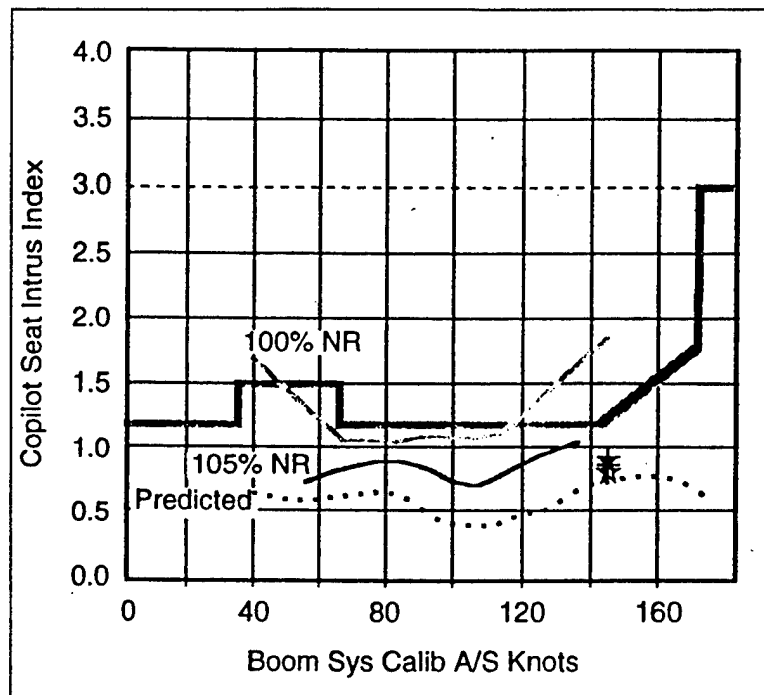


Figure 2.4: Intrusion Index – Copilot’s Station.

C. COMANCHE VIBRATION SOURCES

1. Main Rotor Hub Forces and Moments

As noted earlier, the primary source of helicopter fuselage vibrations is the rotor system. As the forces and moments are transmitted from the rotating to the fixed fuselage system, the rotor system tends to act as a filter. It can be shown for an "N" bladed rotor system that, assuming all blades see the same loading at the same azimuth position, only $N\Omega$ frequency will be seen in the fixed system. This $N\Omega$ frequency in the fixed system can arise from either $N-1$, N , or $N+1$ excitation in the rotating system. Figure 2.5 is a schematic of the hub showing the mechanism of blade-fuselage coupling.

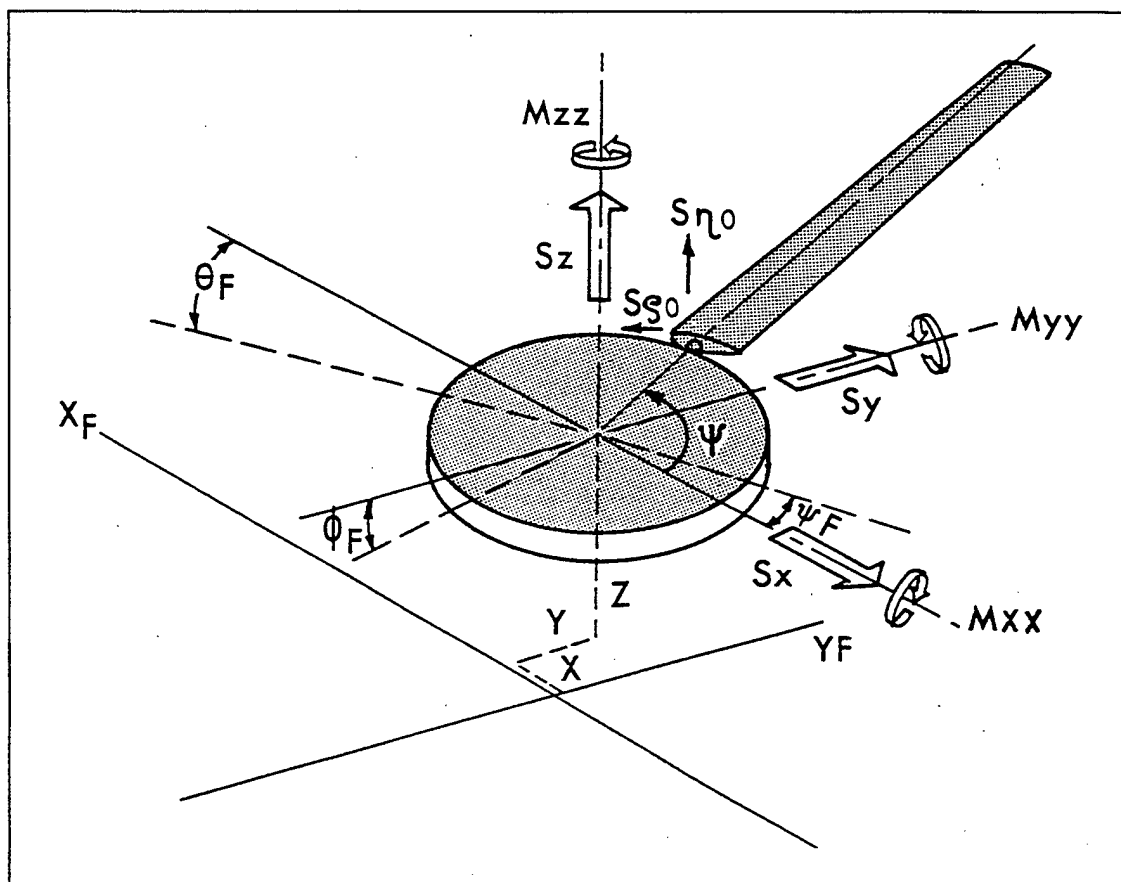


Figure 2.5: Blade-Fuselage Coupling. From Ref.[2].

With the coordinate system given in Figure 2.5, forces in the rotating blade coordinate system can be related to forces in the fixed fuselage using the following transformation:

$$\begin{bmatrix} S_x \\ S_y \\ S_z \\ M_{xx} \\ M_{yy} \\ M_{zz} \end{bmatrix} = \begin{bmatrix} 0 & \frac{5}{2}j & 0 & 0 & 0 & -\frac{5}{2}j \\ 0 & \frac{5}{2} & 0 & 0 & 0 & \frac{5}{2} \\ 0 & 0 & 5 & 0 & 0 & 0 \\ \frac{5}{2}ej & 0 & 0 & 0 & -\frac{5}{2}ej & 0 \\ \frac{5}{2}e & 0 & 0 & 0 & \frac{5}{2}e & 0 \\ 0 & 0 & 0 & 5e & 0 & 0 \end{bmatrix} \begin{bmatrix} S_{\eta 04} \\ S_{\zeta 04} \\ S_{\eta 05} \\ S_{\zeta 05} \\ S_{\eta 06} \\ S_{\zeta 06} \end{bmatrix}$$

or $\{s_F\} = [\lambda]\{s_{\eta 0}\}$

where $[\lambda]$ is the transformation relating forces in the rotating η, ζ system to forces in the fixed X, Y, Z system.

Thus for the five-bladed Comanche helicopter:

- 4/rev and 6/rev flapwise blade root shears result in 5/rev hub pitching and rolling moments in the airframe.
- 5/rev flapwise blade root shears feed into the fuselage directly as 5/rev vertical forces.
- 4/rev and 6/rev chordwise root shears produce 5/rev airframe hub forces in the fore and aft and lateral directions.
- 5/rev chordwise root shears results in 5/rev hub yawing moments.

For the RAH-66, the nominal rotor speed is 354.9 rpm. This places the 1/rev or 1P excitation at 5.915 Hz, with the 5P blade passage frequency occurring at 29.575 Hz.

[Ref. 3]

2. Aerodynamic Excitation

Aerodynamic excitation to the airframe and empennage arises from several sources:

- Main rotor wake impingement.
- Main and tail rotor downwash (induced flow) impingement.
- Flow from around the main rotor hub and pylon assembly structure
- Flow from attached aerodynamic surfaces.
- Flow from protruding irregular fuselage structure, ranging from FABS (forward avionics bays) to as small as a canopy or door handles.

The interaction of this flow is a complex subject, very difficult to predict, and the subject of numerous ongoing research projects. Rotorcraft can have problems where rotor airloads affect airframe loads and, in turn, the airframe effects rotor airloads and blade dynamic response. Some examples: The Sikorsky H-3 had a lateral tail shake that had its onset at about 120 knots. The problem was solved by installing a fairing or “beanie” on top of the main rotor hub to smooth out the flow from this region which was impinging on the aft fuselage.

In development of the Boeing YUH-61 and Sikorsky YUH-60 helicopters, both companies obtained a significant improvement in N/rev vibration levels by “raising the

mast”, that is, increasing the separation between the main rotor hub and the fuselage. In development of the Hughes YAH-64, the initial T-tail design was scrapped and a movable horizontal stabilator installed to eliminate an excessive vibration problem associated with the T-tail. A visual summation of the typical sources of tail excitation is shown in Figure 2.6.

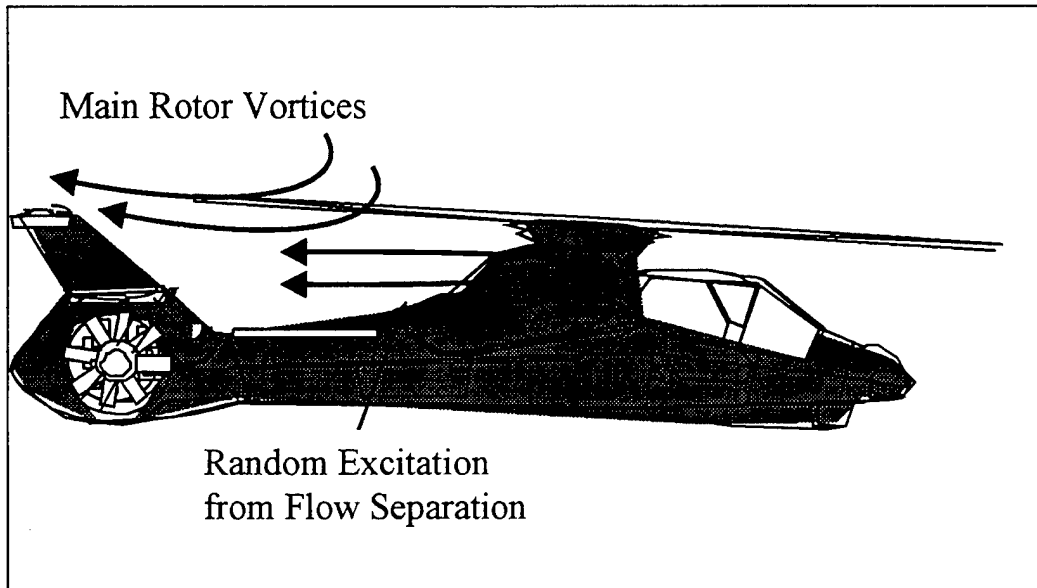


Figure 2.6: Typical Sources of Tail Excitation

An experimental investigation of the interactions between a rotor and a T-tail empennage was conducted by Lieshman and Moedersheim [Ref. 4] at the University of Maryland Rotorcraft Center in 1997. Using a 1/6 scale four-bladed helicopter rotor with generic body shape, a T-tail empennage was placed down stream of the rotor hub as illustrated in Figure 2.7. Both the vertical and horizontal tail surfaces used the NACA 0012 airfoil section with a constant chord of .203 meters. The horizontal tail was located

in two different positions, a high and low plane configuration, with zero degrees angle of attack. Additional parameters of the wind tunnel test are contained in Reference 4.

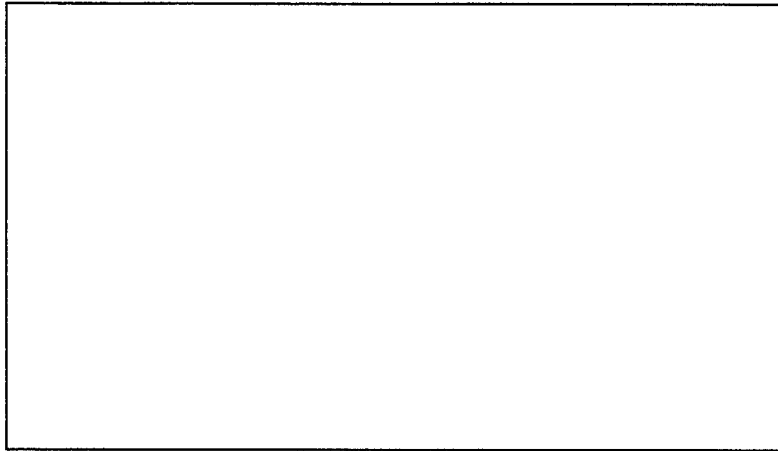


Figure 2.7: Schematic of Rotor/Body/Empennage System. From [Ref. 4].

Through their analysis, they drew the following conclusions:

- Flow behind the rotor was highly asymmetric. The two low pressure regions trailing from the edges of the rotor disk provided evidence of the wake rolling-up into two larger vortex bundles.
- At low advance ratios the flow over the horizontal tail was stalled. The flow gradually reattached as the advance ratio was increased. Airloading was asymmetric primarily due to the difference in strength of the two trailing vortex bundles trailing from the sides of the rotor disk. In some test conditions, a sharp trailing edge peak pressure was observed at the trailing edge of the horizontal tail. This indicated the potential of a junction vortex originating at the junction of the vertical and horizontal tail.
- Measured time-varying pressures showed the flowfield near the horizontal tail was highly unsteady. Below advanced ratios of .15 the unsteady pressure response was low. As the wake transitioned on to the tail, unsteady pressures increased significantly.
- Unsteady pressure responses are characterized by two events, unsteady lift produced by the rotor wake and disturbances caused by the convection of individual vortices.

For the RAH-66, the rotor wake transitions above the T-tail between 40 and 60 knots, as shown in Figure 2.5 [Ref. 3]. Beyond this airspeed range the actual wake is not impinging on the horizontal stabilizer. From Leishman's research; however, there can be convected vortices associated with the passage of blades that can induce disturbances and oscillating loading conditions.

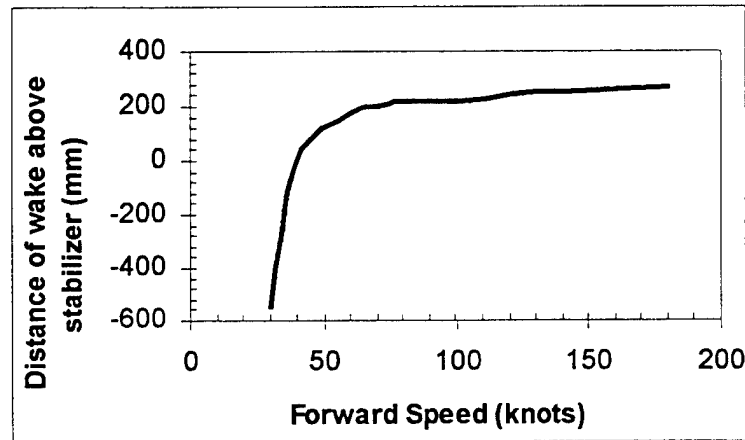


Figure 2.8: Rotor Wake Distance from Horizontal Stabilizer. After Ref. [3].

In addition to the rotor vortices, the wake behind the rotor hub constitutes a low-pressure sink that can draw the flow off of the upper fuselage and produce separation [Ref. 5]. The frequency content of this excitation is often determined by modeling the rotor hub as a circular cylinder where vortices are shed as a Karman vortex street. Through the Strouhal number, a non-dimensional constant, vortex shedding frequency can be related to freestream velocity and the diameter of a two dimensional cylinder. [Ref. 5]

The relationship is given by:

$$f_s = \frac{SU}{D}$$

where f_s = Vortex shedding frequency (Hz)

S = Strouhal number

U = Freestream velocity (ft/sec)

D = Cylinder diameter (ft)

Determination of the Strouhal number from Schlichting [Ref. 5:p:32] requires interpolating from a small plot. Using the results from a wind tunnel experiment done at the Naval Postgraduate School on a two-dimensional cylinder by Small, Hebbbar, and Platzer [Ref. 6], the Strouhal number and vortex shedding frequency can more easily and accurately be determined. In this experiment [Ref. 6], the vortex shedding frequency and Strouhal number were calculated for Reynolds numbers ranging from 2.7×10^4 to 1.9×10^5 . From this, the data presented in Figure 2.9 was generated. The Strouhal number represents the slope of the line and can be used to calculate the frequency of shedding from a known diameter and given velocity.

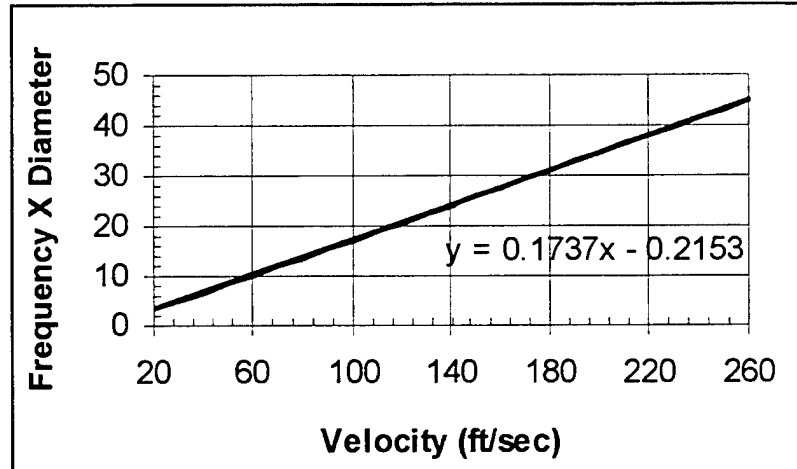


Figure 2.9: Shedding frequency for the Quasi-two-dimensional Cylinder. After Ref. [6].

For the Comanche, at 100 knots (168.78 ft/sec) and with a rotor hub pylon of approximately .75 meters (2.46 ft), the calculated vortex shedding frequency is 11.827 Hz. As the airspeed and point of separation changes, the shedding frequency will be effected, as shown by the equation on the previous page. The area around the main rotor pylon is actually a complex array of surfaces needed to reduce radar signature. Separated flow could occur from any of these surfaces, with varying frequency content of the vortices. In this case, more broadband vortex shedding will occur.

From these factors, RAH-66 response data should show energy associated with main rotor 5P, 29.75 Hz and if a rotor track and balance problem, main rotor 1P at 5.95 Hz. There could also be energy associated with separated flow from the main rotor pylon, centered around 11-12 Hz, and some broad band excitation from the convected rotor vortices impinging on the horizontal tail.

III. SPECTRAL ANALYSIS

Figure 3.1 shows the time history of lateral excitation at the pilot's heels. When analyzed over the full record length of 60 seconds, the data is classified as random. Such random time functions as this data set commonly exist in nature; a typical example being pressure gusts aircraft encountered in flight. The method used to characterize these functions is known as spectral analysis, and a discussion of the theory, from Thomson [Ref. 7], and techniques for digital signal analysis follows.

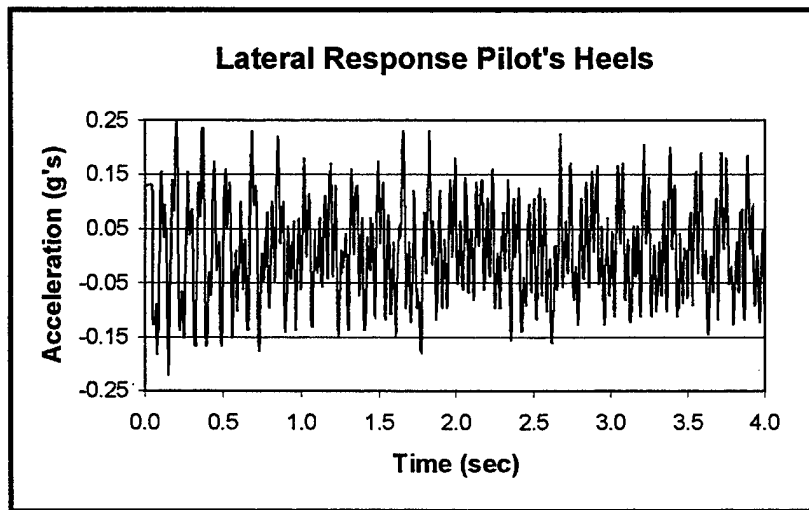


Figure 3.1: Time History of Lateral Acceleration.

A. TIME AVERAGING

Despite the irregular nature of the time history in Figure 3.1, most "random" functions exhibit some degree of statistical regularity and by applying averaging processes, we can characterize the phenomena. In observing the data, each record is referred to as a sample and the collection of samples is the ensemble. If the ensemble average is taken at a

specific time, t_l , and then at another time, $t_l + \tau$, and they remain the same, the process is said to be stationary. Similarly, if the ensemble averages are replaced by time averages, or averaging each sample, and the averages from different samples remains the same, the random process is ergodic. Key assumptions necessary for our analysis is that the random response phenomena exhibited by the aircraft is stationary and ergodic. As such, statistical properties can be derived from single time histories of sufficient length. [Ref. 7]

To derive these properties a review of statistics is required. From the time histories, we can define the expected value (mean):

$$E[x(t)] = \lim_{T \rightarrow \infty} \frac{1}{T} \int_0^T x(t) dt$$

For the case of discrete variables, the expected value is given by the following equation:

$$E[x] = \lim_{n \rightarrow \infty} \frac{1}{n} \sum_{i=1}^n x_i$$

We can then apply the averaging process to the mean square value, also referred to as the square of the expected value.

$$E[x^2(t)] = \overline{x^2} = \lim_{T \rightarrow \infty} \frac{1}{T} \int_0^T x^2 dt$$

Linking this back to basic statistics, with the variance defined as:

$$\sigma^2 = \overline{x^2} - (\bar{x})^2$$

$$\sigma^2 = \lim_{T \rightarrow \infty} \frac{1}{T} \int_0^T (x - \bar{x})^2 dt$$

the mean square value (MSV) is simply the variance when the data has an expected value (mean) of zero. If thought of in terms of a sin wave, or multiple harmonic function, where the mean is removed (detrended) before analysis, then the variance and MSV are the same.

Knowing these statistical properties of a given signal, the correlation, or similarity, between different signals can be determined. This is an important function in time domain analysis as it can help identify signals buried in noise or propagated in time through a structure. Additionally, it provides a transition into Fourier analysis and the frequency domain, where a structure's spectral characters can better be analyzed. The correlation function is computed by multiplying the ordinates of two records at each time and determining the average value by dividing the sum by the number of products. The product is a maximum when the two signals are very similar or identical. For dissimilar records, the products will be negative and positive, so the sum will be small. If two signals are identical with one shifted by some time, we can compute the correlation by taking just a single time record and multiplying it by itself, with the specified time delay τ . This is called the autocorrelation function, and is defined by the following formula.

$$R(\tau) = E[x(t)x(t + \tau)] = \langle x(t)x(t + \tau) \rangle = \lim_{T \rightarrow \infty} \frac{1}{T} \int_{-T/2}^{T/2} x(t)x(t + \tau) dt$$

If the time delay $\tau = 0$, the equation reduces to the mean square value or variance.

$$R(0) = \overline{x^2} = \sigma^2$$

If the two records are truly dissimilar, we call their product the cross correlation. It is

define it by:

$$R_{xy}(\tau) = E[x(t)y(t + \tau)] = \langle x(t)y(t + \tau) \rangle$$

$$= \lim_{T \rightarrow \infty} \frac{1}{T} \int_{-T/2}^{T/2} x(t)y(t + \tau) dt$$

B. FREQUENCY DOMAIN ANALYSIS

Having defined averaging processes for the time domain, the random function can be transitioned to the frequency domain [Ref. 7]. This will assist in relating the response data back to the sources of excitation discussed earlier.

The time signal $x(t)$ can be expressed in terms of its Fourier series:

$$x(t) = \sum_{-\infty}^{\infty} c_n e^{in\omega_1 t}$$

Because the record is periodic it can be represented by the Fourier series:

$$x(t) = \text{Re} \sum_{n=1}^{\infty} C_n e^{in\omega_1 t} = \frac{1}{2} \sum_{n=1}^{\infty} (C_n e^{in\omega_1 t} + C_n^* e^{-in\omega_1 t})$$

where C_n a complex function and C_n^* is its complex conjugate. It can then be proven [Ref. 7] that the mean square value of the function is given by

$$\overline{x^2} = \sum_{n=1}^{\infty} \frac{1}{2} C_n C_n^*$$

From this, it can be seen that the MSV can be computed in either the time or frequency domain, depending on which technique provides better analysis of the data.

The mean square value (MSV) represents contributions from the entire frequency band of the signal. If only a certain frequency range is of interest, the MSV for that range of frequency, Δf , is the power spectrum (PS). The power spectrum, $P(f_n)$, is then just the product of the Fourier coefficients from the frequency range of interest, f_k , with the mean square value being the sum of the power spectrum across the entire bandwidth. [Ref. 7]

$$P(f_n) = \frac{1}{2} C_n C_n^* \qquad \overline{x^2} = \sum_{n=1}^{\infty} P(f_n)$$

If the power spectrum is divided by the frequency interval, Δf , the result, defined as the discrete power spectral density(PSD) $S(f_n)$, gives the contribution to the power spectrum from an even more narrow frequency band. This can be extended for a continuous spectrum as the limiting case of $S(f_n)$ as $\Delta f \rightarrow 0$.

$$S(f_n) = \frac{P(f_n)}{\Delta f} = \frac{C_n C_n^*}{2\Delta f}$$

The mean square value can then be computed from the PSD by

$$\overline{x^2} = \sum_{n=1}^{\infty} S(f_n) \Delta f$$

The root mean square (RMS), synonymous with the standard deviation, can be found by taking the square root of the mean square value (MSV).

$$RMS = \sqrt{\overline{x^2}}$$

As we are dealing with non-periodic functions over discrete time intervals, use of the Fourier integral, a limiting case of the Fourier series, is required. The Fourier Integral and Fourier transform of $x(t)$ are defined respectively as

$$x(t) = \int_{-\infty}^{\infty} X(f)e^{i2\pi ft} df \qquad X(f) = \int_{-\infty}^{\infty} x(t)e^{-i2\pi ft} dt$$

Using Parseval's theorem, the MSV of the discrete signal in the time domain can be equated to the Fourier transform of the signal multiplied by its complex conjugate. If $x_1(t)$ and $x_2(t)$ are real valued time functions and their Fourier transforms are given by $X_1(f)$ and $X_2(f)$ then

$$\int_{-\infty}^{\infty} x_1(t)x_2(t)dt = \int_{-\infty}^{\infty} X_1(f)X_2^*(f)df$$

If $x_1(t) = x_2(t) = x(t)$ the MSV and PSD can be expressed in terms of the Fourier transform

$$\overline{x^2} = \lim_{T \rightarrow \infty} \frac{1}{T} \int_{-T/2}^{T/2} x^2(t)dt = \int_{-\infty}^{\infty} \lim_{T \rightarrow \infty} \frac{1}{T} X(f)X^*(f)df = \int_{-\infty}^{\infty} S(f)df$$

As with the Fourier coefficients, the MSV and RMS of the signal can be determined from the Fourier transforms. Additionally, the autocorrelation function, symmetric about the origin, can be related to the spectral density function via the Wiener-Khintchine equation. [Ref. 7]

$$S(f) = 2 \int_0^{\infty} R(\tau) \cos 2\pi f \tau d\tau$$

The cross-spectral density (CSD), defined as the Fourier transform of the cross-correlation function:

$$S_{xy}(f) = \int_{-\infty}^{\infty} R_{xy}(\tau) e^{-i2\pi f \tau} d\tau$$

Can also be determined by multiplying the Fourier transforms of the two signals of interest.

$$S_{xy}(f) = \lim_{T \rightarrow \infty} \frac{1}{T} X^*(f) Y(f)$$

Given all of these tools, the one of major interest in analyzing the flight test data is the power spectral density (PSD). This function of frequency gives an indication of the contribution to the total response, in our case accelerations, due to a discrete frequency bandwidth. Additionally, the cross-spectral density recaptures the phasing information lost when the Fourier Integral is multiplied by its complex conjugate.

C. DIGITAL SIGNAL PROCESSING

Given this theory, digital signal processing methods have been devised that compute the PSD from discrete time histories. Vectors represent the time histories. In our case, the sampling rate is 300 samples per second and record length is 60 seconds. Therefore, the vector of the discrete signal has 18,000 data points.

To convert this time signal into either a PSD or CSD, the first step is to decide how many points, N , are needed in the Fast Fourier Transform (FFT). For computational speed and accuracy, FFTs are done in power of two. The number of points also determines what the effective bandwidth of the processed information will be. Bandwidth, Δf , is defined as $1/\text{Time}$, and for a discrete signal, $\text{Time} = N \times \Delta t$ (time increment). The time increment, Δt , is equal to $1/\text{sampling rate}$, or, in our case, $1/300$ sec. If a 1024 point FFT is utilized, $\Delta f = 300/1024 = .293$ Hz. As the number of points in the FFT increases, the bandwidth decreases and you get finer frequency resolution.

There is a penalty when working with random data to increasing the number of points in the FFT. Based on N , the signal is divided into n_d records or windows and has any linear trend removed. As N increases, the number of windows, n_d , decreases and there is less averaging occurring. This is demonstrated when computing the expected value.

To suppress leakage of the signal from one frequency range to the next, time windows are used that taper the time history data. This eliminates discontinuities at the beginning and end of the record to be analyzed. A commonly used window, that is used exclusively during this analysis, is the Hanning window. It is given by

$$w(t) = .5 * (1 - \cos(\frac{2\pi t}{N}))$$

and multiplied by the N data points of each n_d segment. Use of the window does reduce the amplitude of the processed signal. In the case of the Hanning window, the output is .375 times smaller. A correction is made in the normalizing of the PSD to account for this.

Variance is introduced by tapering the signal. To reduce this, the n_d segments are overlapped. In terms of the Hanning window, the overlapping brings the "peaks" of each cosine window closer to each other. This process, basically, takes the points that were at the end of one n_d segment, where the window is near zero, and makes it the "main area" for the next. The FFTs are then computed for each tapered, overlapped segment.

From the FFTs, the PSD can be determined using the following formulas:

$$E[|FFT|^2] = \frac{\sum_{i=1}^{n_d} (|FFT|^2)_{n_d}}{n_d} \quad P_{xx} = \frac{2 * E[|FFT|^2] * \Delta t}{(norm(window))^2}$$

The expected value is the sum of the FFTs of each segment multiplied by its complex conjugate, or the magnitude of the FFT squared. Either way, it produces a real

valued function that is then divided by the number of segments, n_d . As discussed earlier, and seen here, increasing N reduces the number of FFT averages in the expected value.

The PSD is then determined by "normalizing" the expected value. This first involves multiplying by 2 as the PSD represents the one-sided autospectral density function. Then, the signal is multiplied by the time increment, Δt (or dividing by the sampling rate, from the definition of Δt) and divided by the norm of the window, squared. The reasons for this come from the definition of the FFT and by canceling several terms. Bendat and Piersol [Ref. 8:p.371] provide the exact proof; however, their notation requires dividing the signal by N and then adjusting for the attenuation caused by a tapering window. The norm of the window (its length in N dimensions) accounts for both elements. For no windowing, computationally done using a boxcar window, the norm^2 is the number of points in the FFT, 1024. For a Hanning window, the $\text{norm}^2 = 1024 \times .375 = 384$. As discussed earlier, this corresponds to the attenuation causing by using a Hanning window. Figure 3.2 and 3.3 provide a visual illustration of the procedure used to compute the autospectral density function (PSD).

For the cross spectral density, the same steps are followed for each time history. Then the FFTs from each signal, $x(t)$ and $y(t)$ are multiplied by each other and the expected value is a complex function. $E[FFT^2]$ is normalized using the same method.

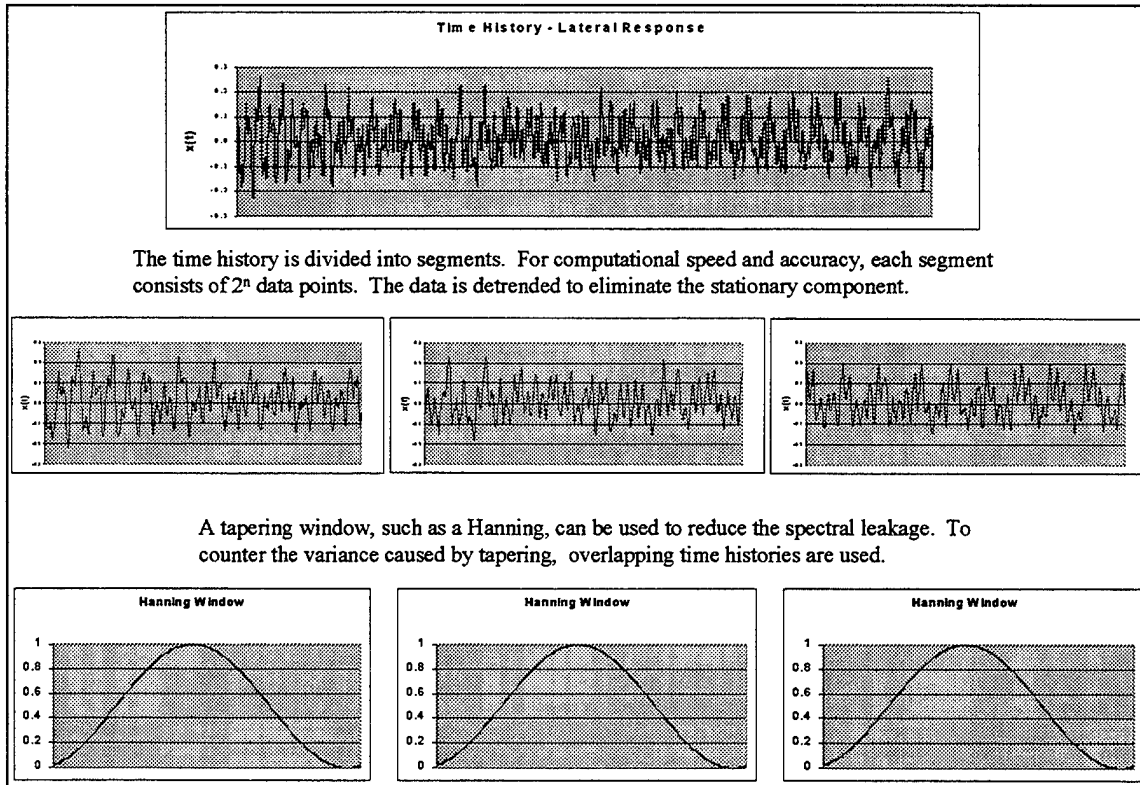


Figure 3.2: PSD Computational Steps – Time Domain.

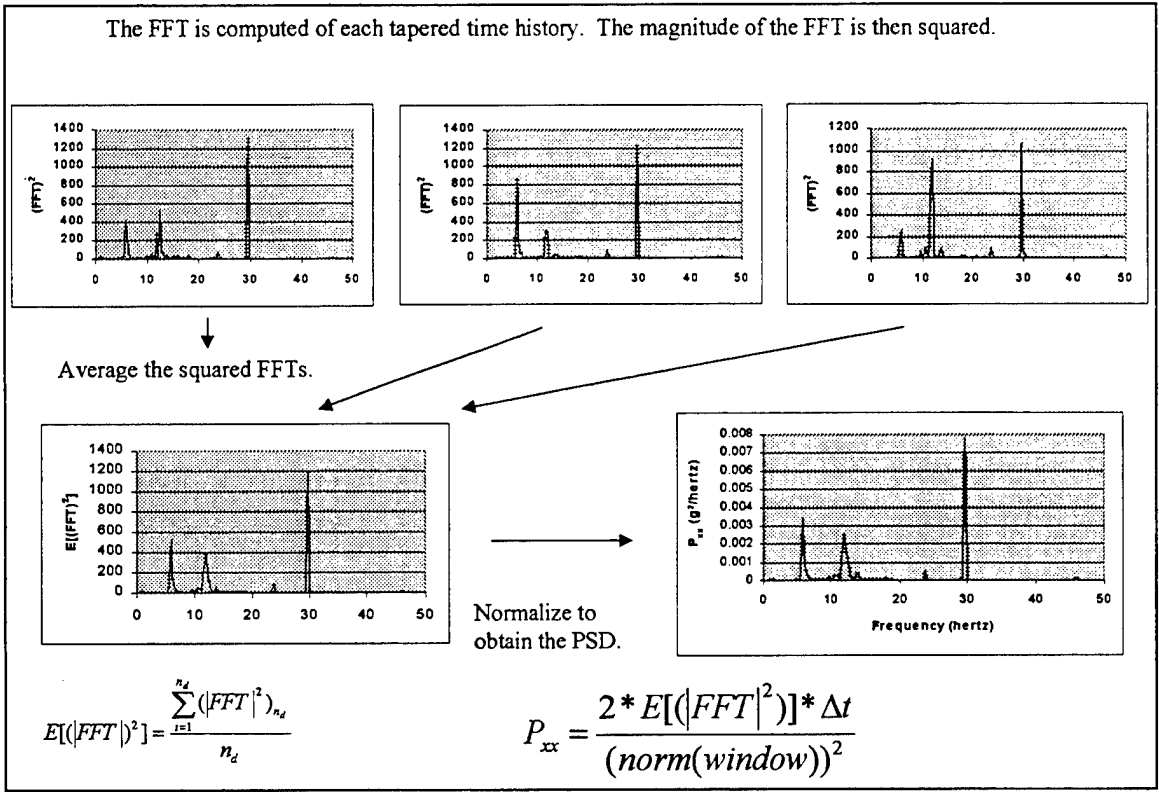


Figure 3.3: PSD Computation – Frequency Domain.

The PSD or CSD output vector is of length $N/2$ with a frequency band from $0:\Delta f:(\text{sampling rate}/2)$. As an example, with N of 1024 points and a sampling rate of 300 Hz, the maximum frequency, commonly referred to as the Nyquist frequency, is 150 Hz. The frequency vector begins at 0 and goes to 150 Hz in increments of $300/1024$ or .293. For each point of the frequency vector, the PSD vector has a corresponding value. This value represents the energy associated with that frequency band. So, in this example, the first value of the PSD vector represents the energy present within the 0 to .293 Hz range.

Units of either the PSD or CSD are $(\text{input units})^2/\text{Hz}$. In the case of accelerometer output, the PSD units are g^2/Hz . With units like this, it is often difficult to grasp an understanding of what the information really means. The RMS is much easier to interpret, which has the same units of the input, in this case, g 's. To compute the RMS, the PSD vector is multiplied by the frequency increment, Δf . This vector is then summed within the frequency range of interest. The resulting scalar is the MSV and the RMS is the square root. If, for example, the RMS between 5-25 Hz is needed, the PSD vector is multiplied by $\Delta f = 300/1024$. Then, only the indices of the vector that represent energy between 5-25 Hz are summed, points 17-86 of the 512 total PSD values. The square root is the RMS and represents the total energy or response between 5 and 25 Hz. Comparing back to the time domain, this RMS value equates to the standard deviation.

IV. FLIGHT TEST DATA ANALYSIS

Time histories of accelerometers and pressure transducers from flight tests were analyzed using both 1024 and 4096 point FFT. For computational speed, 1024 point FFTs were utilized for final analysis. Several different tapering windows were also applied with no noticeable difference. The excitation frequencies are clearly evident and are an order of magnitude higher than the energy of the surrounding frequency bands. Therefore, even when no side lobe reduction techniques were utilized, the frequency content of the response was pronounced. To remain consistent with the methods used by Sikorsky, a Hanning window with 67% overlap was used. This did reduce the spectral leakage and variance associated with windowing and produced a more accurate PSD value.

A. ACCELEROMETERS

Data records at 60, 80, 100, 120, and 140 knots were obtained for the accelerometers listed in Table 4.1. The sampling rate for all signals was 300 samples per second with a 60 second record length. A complete listing of all test flight parameter is contained in Appendix A.

The PSD of each accelerometer through the range of airspeeds was computed. In looking at the energy across the entire frequency spectrum, 0-150 Hz, there was significant energy from 0-30 Hz, and none of magnitude beyond that range. Figure 4.1 through 4.3 display the PSD for nose cone lateral, pilot heel lateral, and copilot heel vertical. The programs used to compute the PSDs and CSDs is in Appendix B.

Accelerometers	
Mnemonic	Measurement
LNOSE:D:300	Lateral Nose
VNOSE:D:300	Vertical Nose
LONOSE:D:300	Longitudinal Nose
LPHEEL:D:300	Lateral Pilot Heel
VPHEEL:D:300	Vertical Pilot Heel
LPF:D:300	Lateral Pilot Floor
VPF:D:300	Vertical Pilot Floor
LOPF:D:300	Longitudinal Pilot Floor
LPOVRHD:D:300	Lateral Pilot Overhead
VCOPHEEL:D:300	Vertical Copilot Heel
LCOPHEEL:D:300	Longitudinal Copilot Heel
VCOPF:D:300	Vertical Copilot Floor
LCPOVRHD:D:300	Lateral Copilot Overhead
LVPYLNT:D:300	Lateral - Vertical Pylon Top
VSTABTLT:D:300	Vertical - Hor Stab Left Tip
LOSTABTL:D:300	Longitudinal - Hor Stab Left Tip
VSTABTRT:D:300	Vertical - Hor Stab Right Tip
LOSTABTR:D:300	Longitudinal - Hor Stab Right Tip

Table 4.1: Accelerometers.

As previously noted, primary excitation for a 5-bladed rotor occurs at 5P, which is 29.6 Hz for the Comanche. As expected for this case, 5P response centered at 29.6 Hz dominates, especially at higher airspeeds. In contrast, the amplitude of the other frequency bands is not discernable. To provide more insight at response due to other than 5P, Figures 4.4 through 4.18 displays the accelerometer response from 5-25 Hz. Within this frequency band, much greater detail in the response data can be discerned. Given on the next 17 pages are plots that indicate the frequencies of excitation along with the expected increase with airspeed.

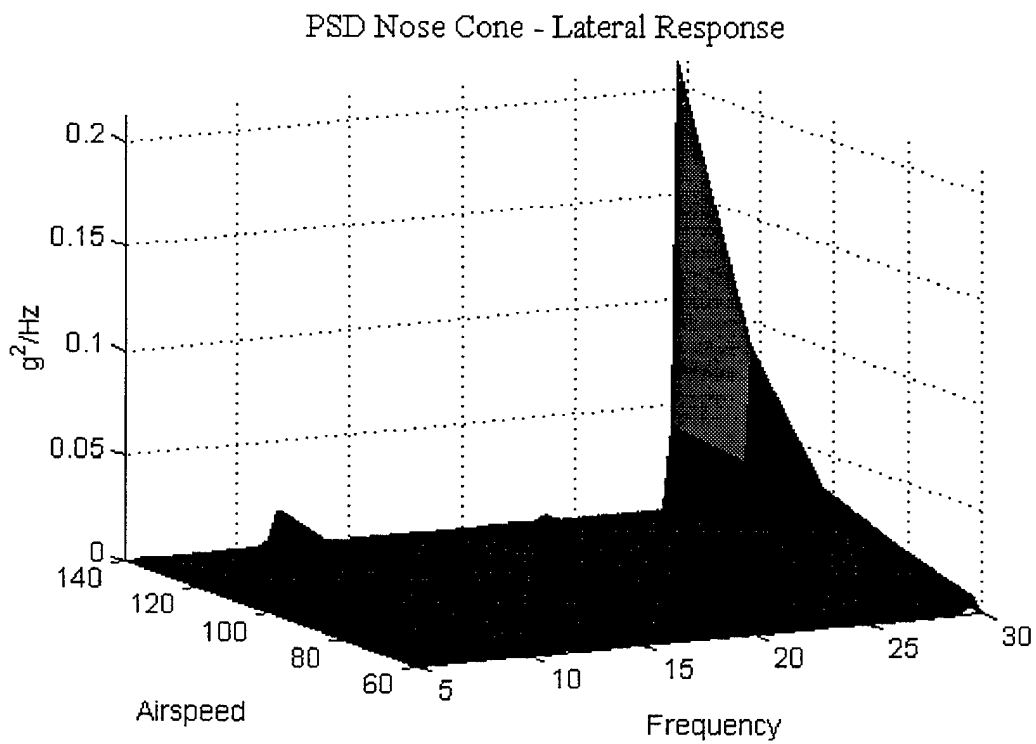


Figure 4.1: Nose Cone – Lateral 5-30 Hertz.

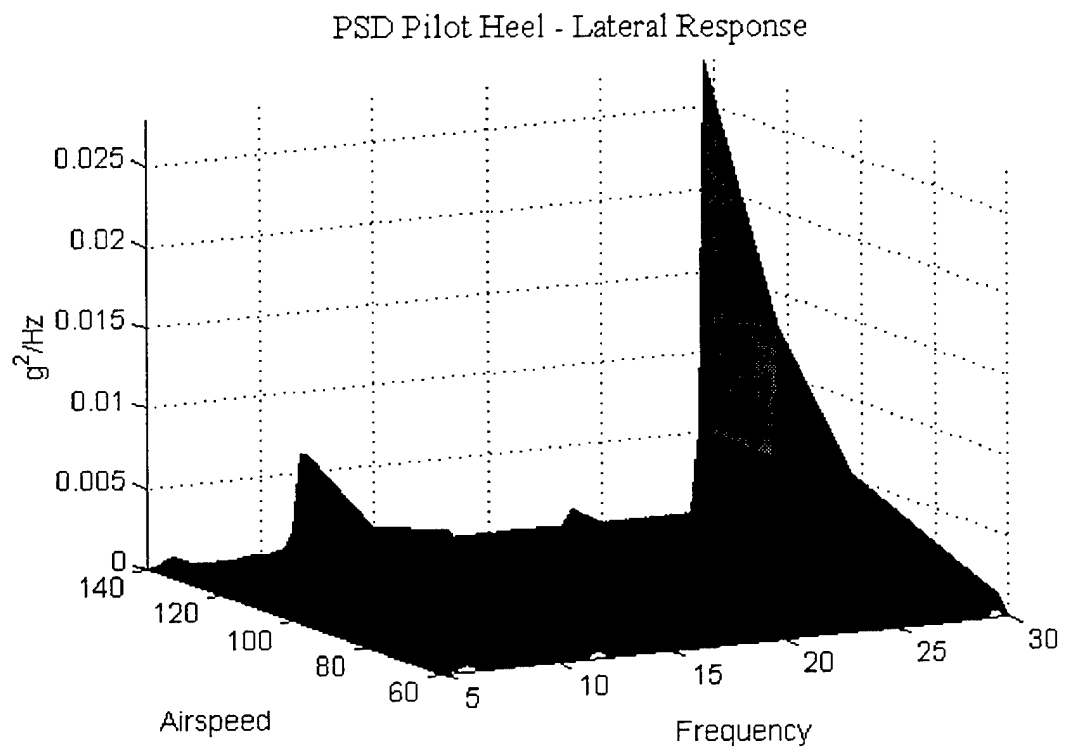


Figure 4.2: Pilot Heel – Lateral 5-30 Hertz.

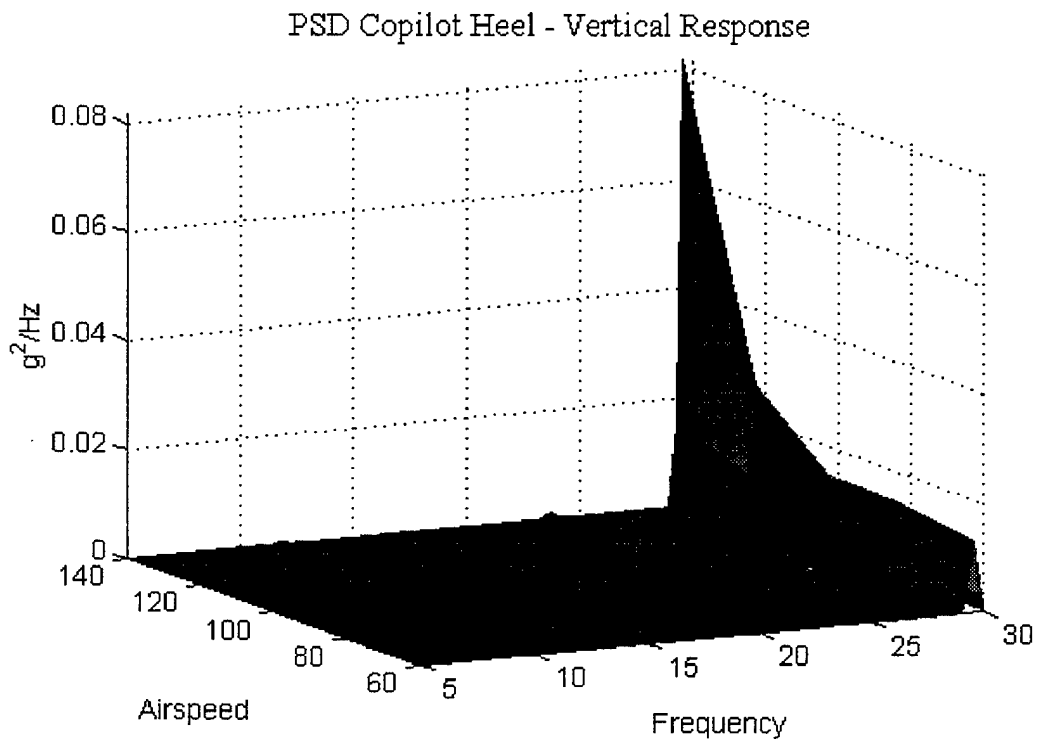


Figure 4.3: Copilot Heel – Vertical 5-30 Hertz.

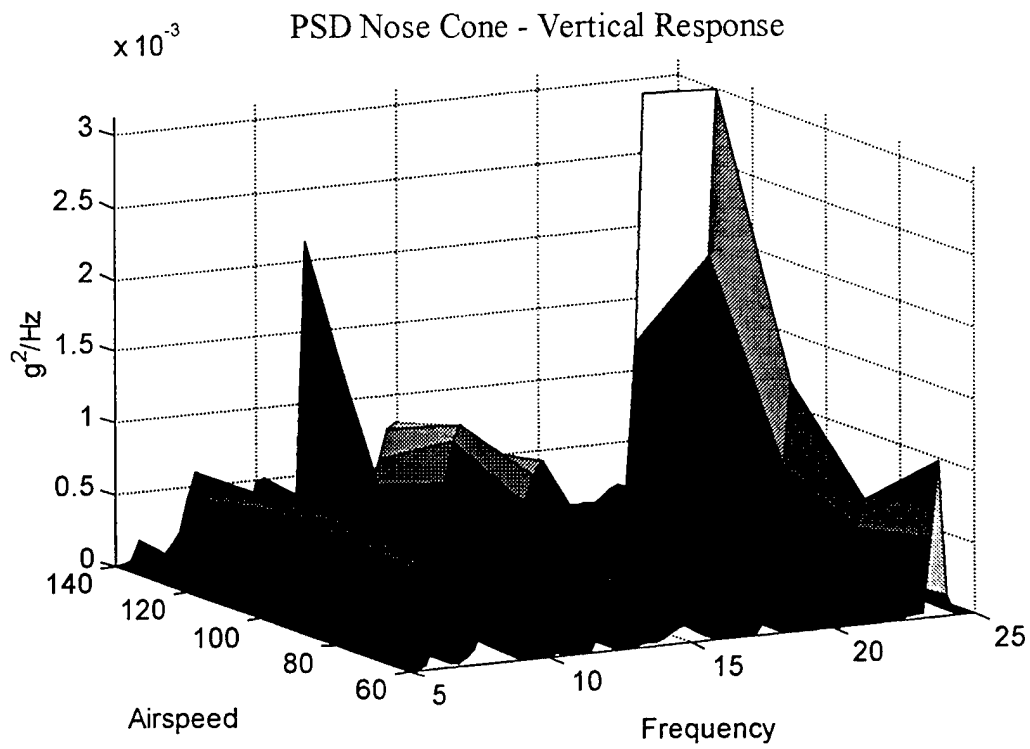


Figure 4.4: Nose Cone - Vertical 5-25 Hertz.

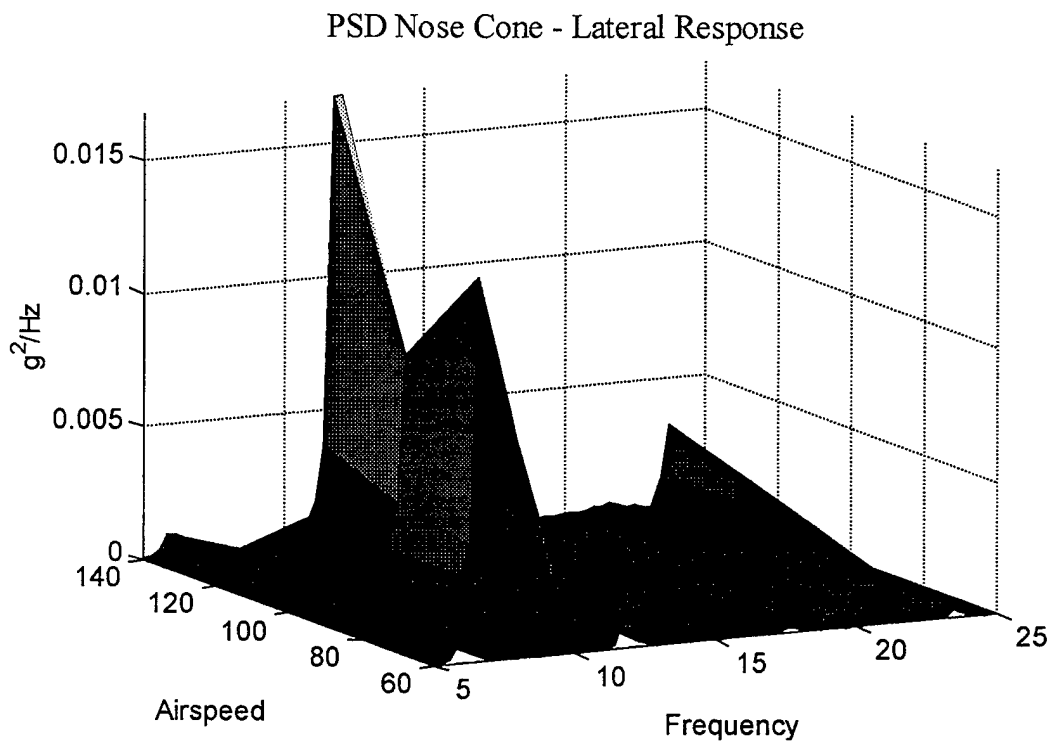


Figure 4.5: Nose Cone – Lateral 5-25 Hertz.

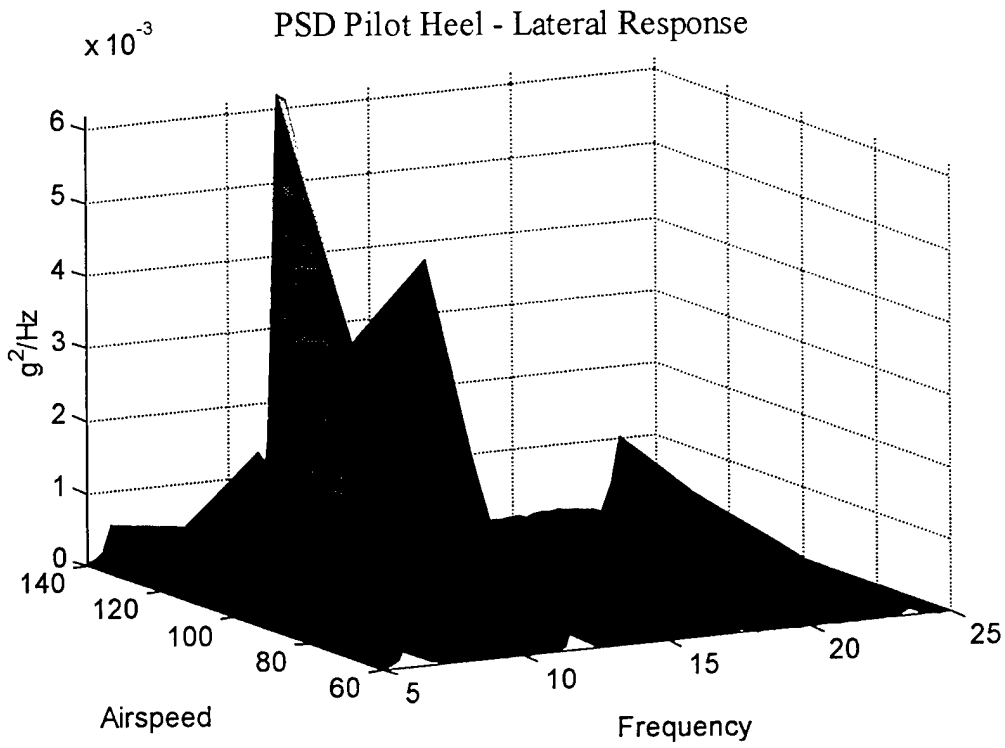


Figure 4.6: Pilot Heel – Lateral 5-25 Hertz.

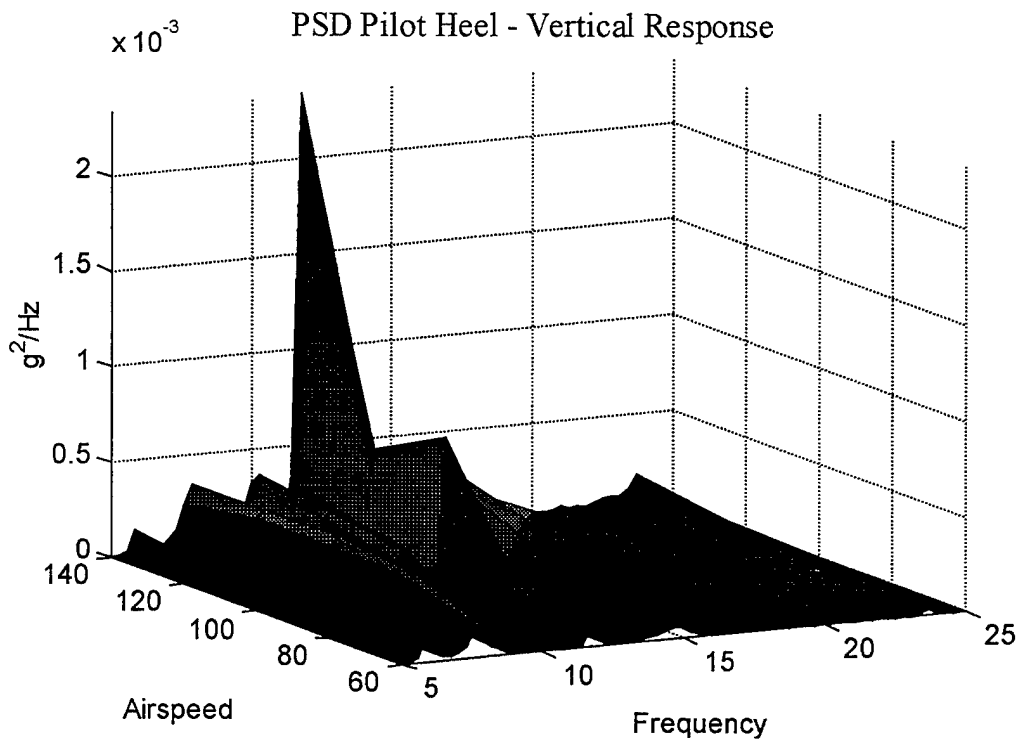


Figure 4.7: Pilot Heel – Vertical 5-25 Hertz.

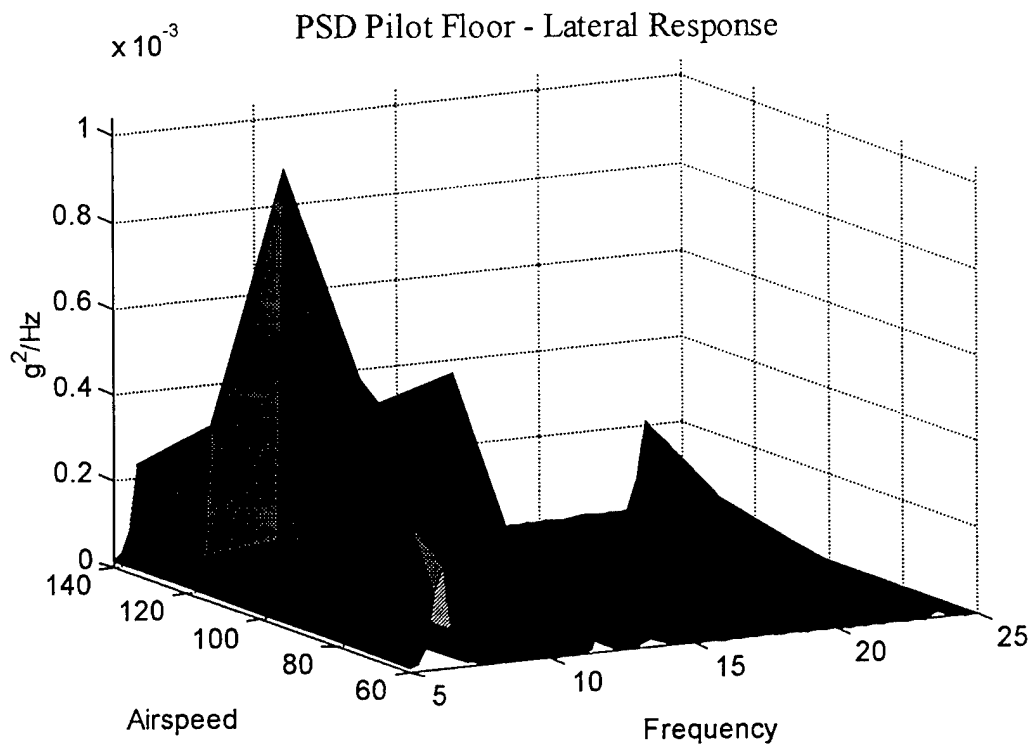


Figure 4.8: Pilot Floor – Lateral 5-25 Hertz.

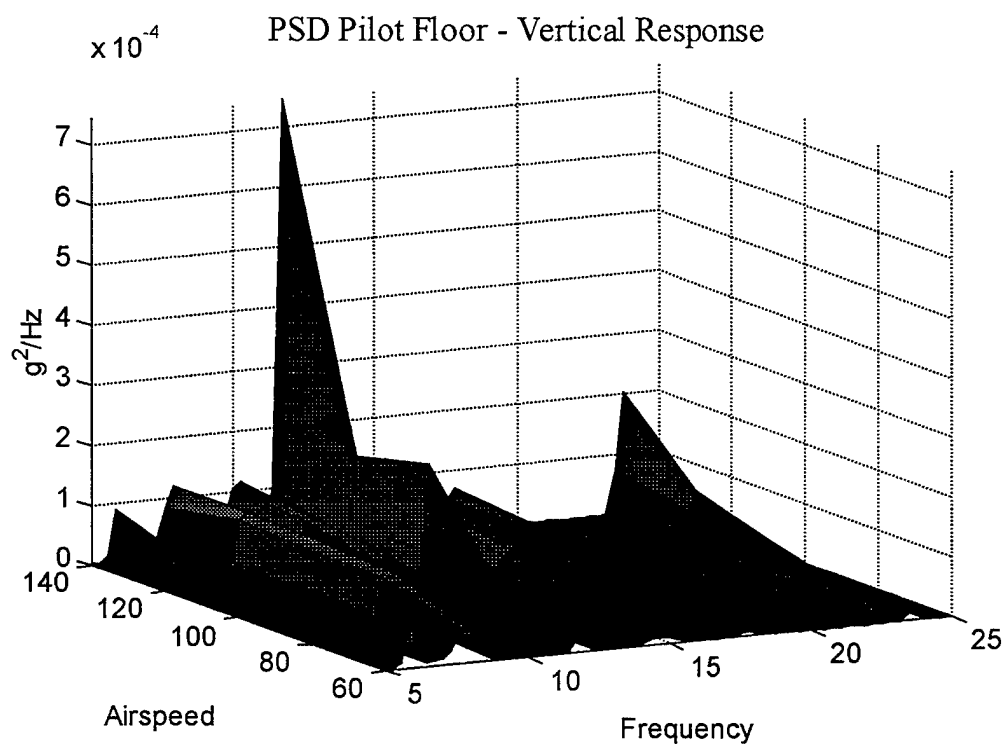


Figure 4.9: Pilot Floor – Vertical 5-25 Hertz.

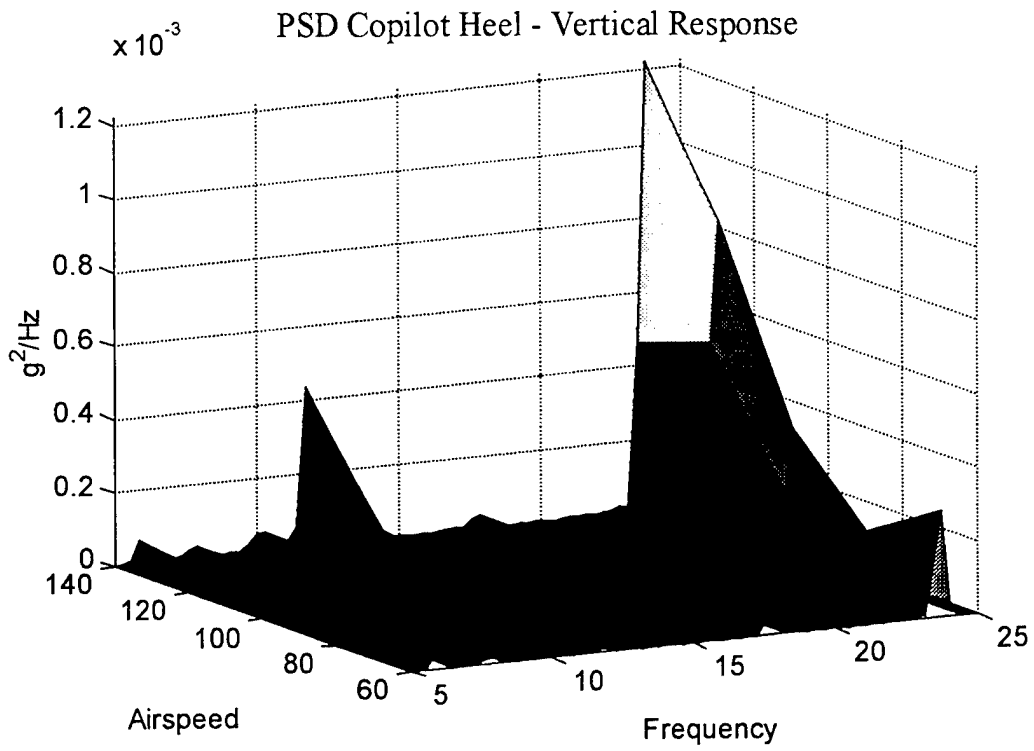


Figure 4.10: Copilot Heel – Vertical 5-25 Hertz.

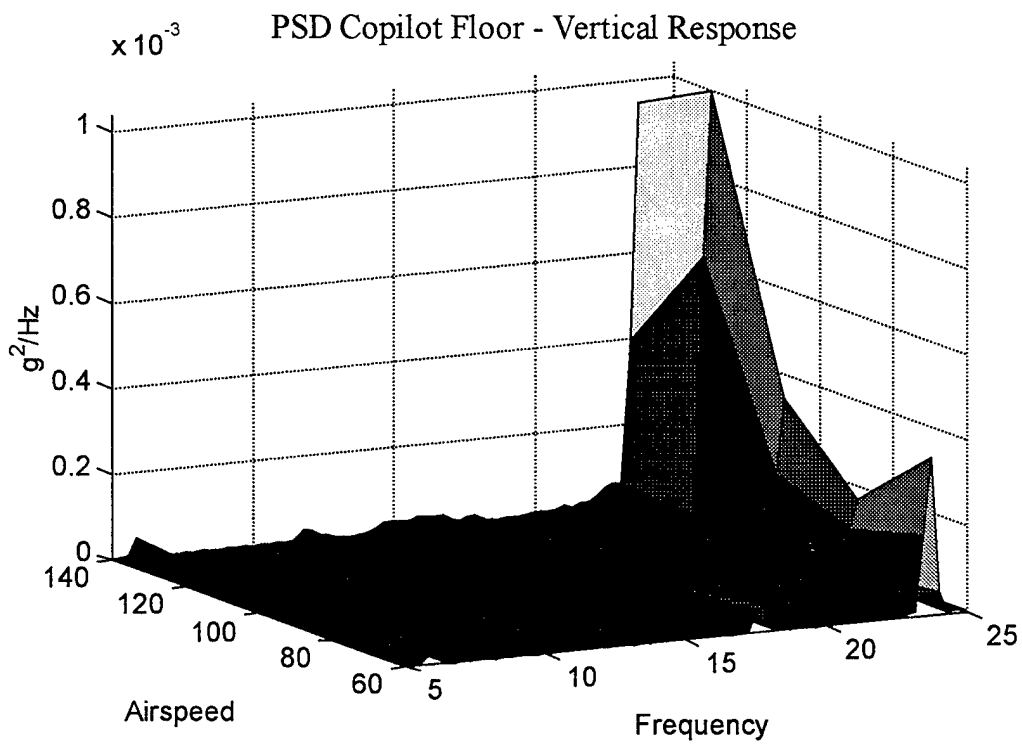


Figure 4.11: Copilot Floor – Vertical 5-25 Hertz.

PSD Pilot Overhead - Lateral Response

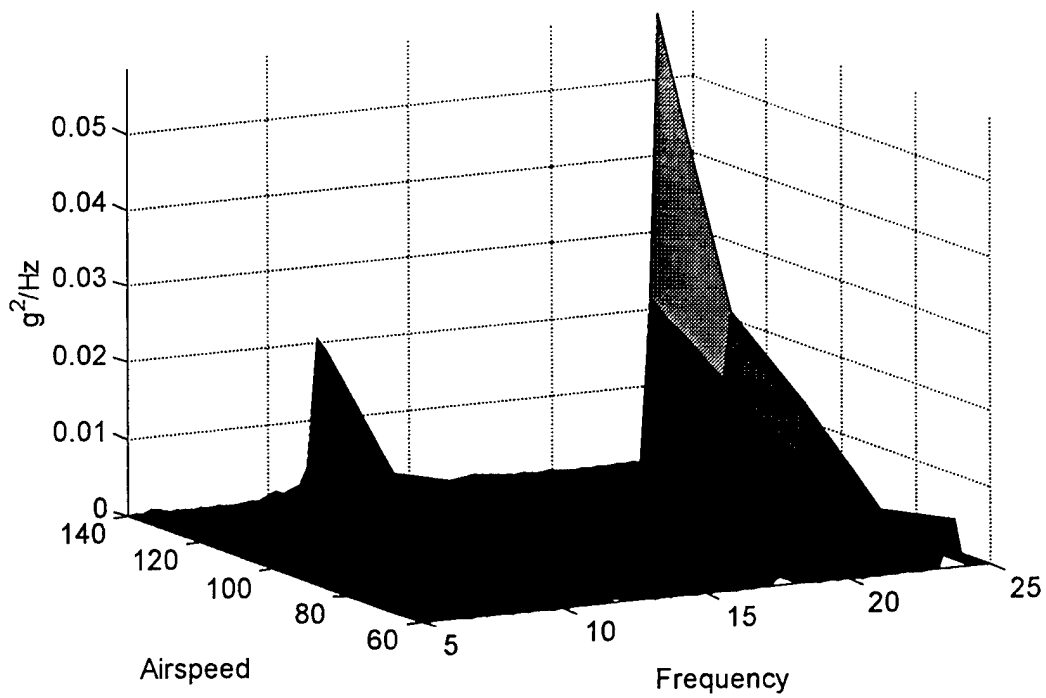


Figure 4.12: Pilot Overhead – Lateral 5-25 Hertz.

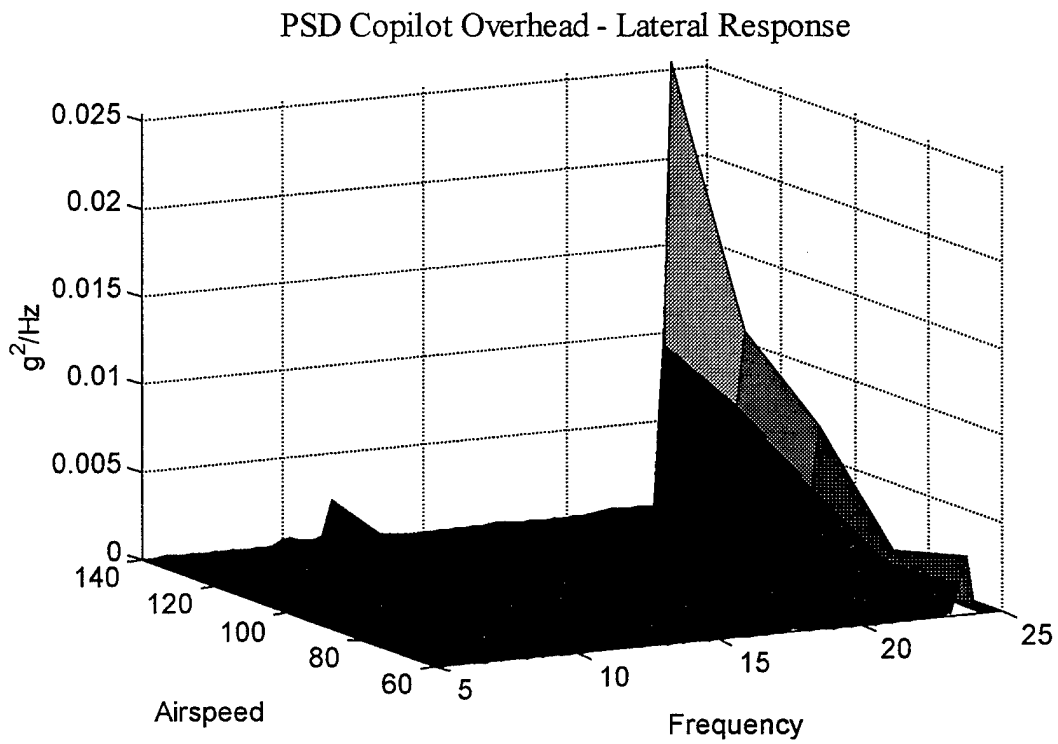


Figure 4.13: Copilot Overhead – Lateral 5-25 Hertz.

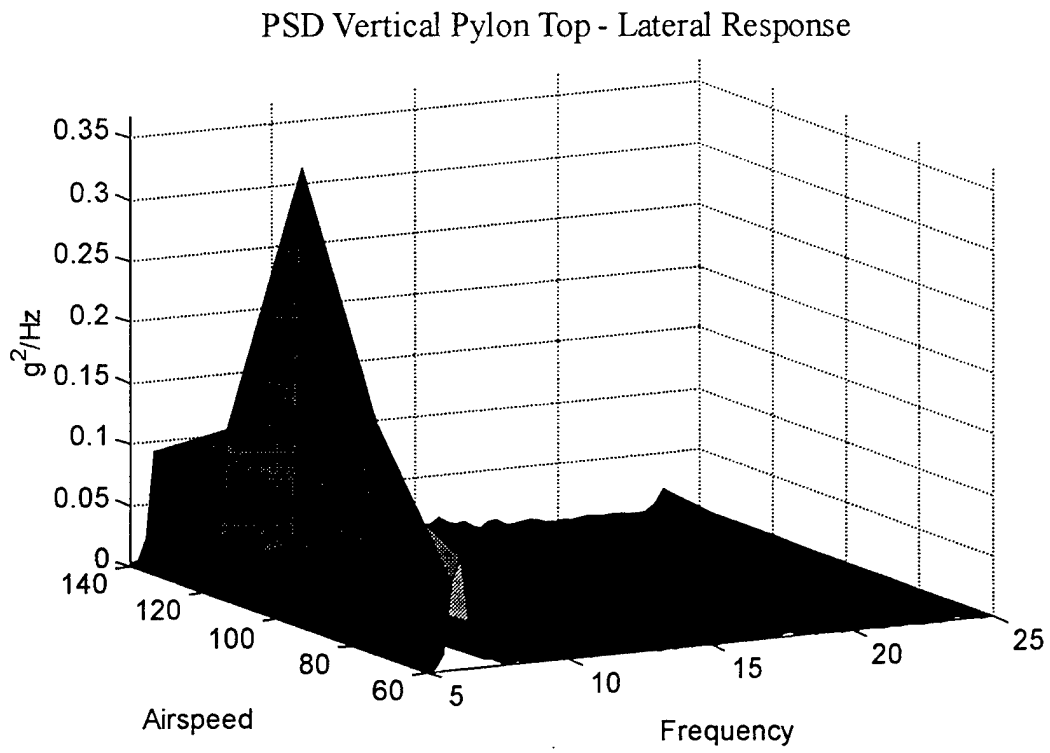


Figure 4.14: Vertical Pylon Top – Lateral 5-25 Hertz.

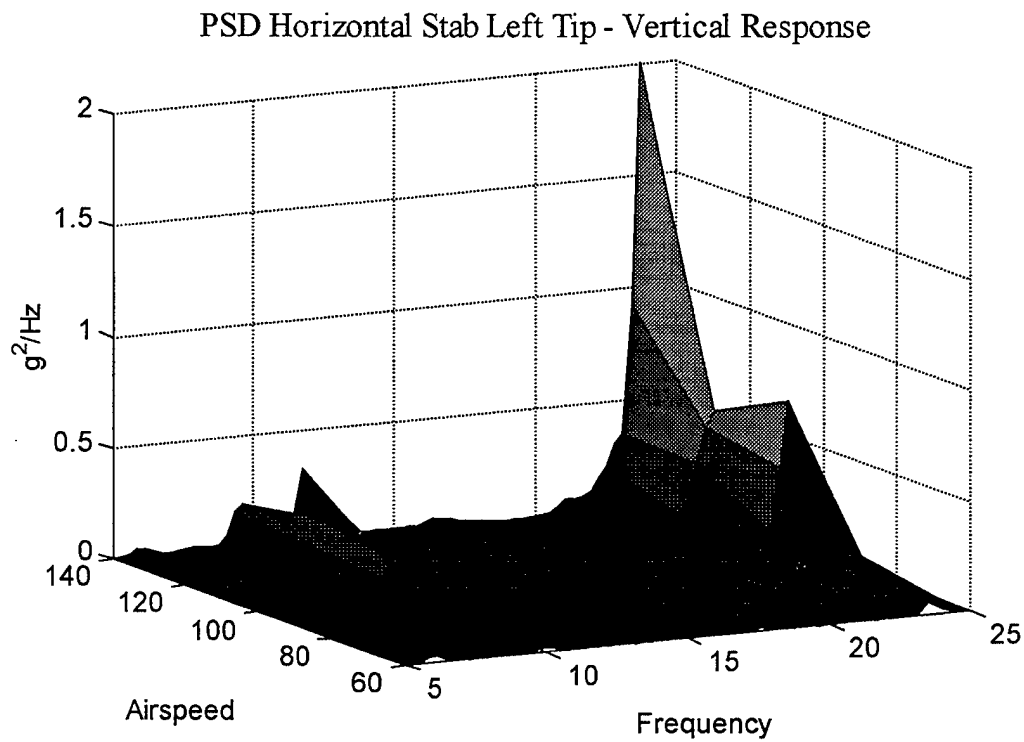


Figure 4.15: Horizontal Stab Left Tip – Vertical 5-25 Hertz.

PSD Horizontal Stab Right Tip - Vertical Response

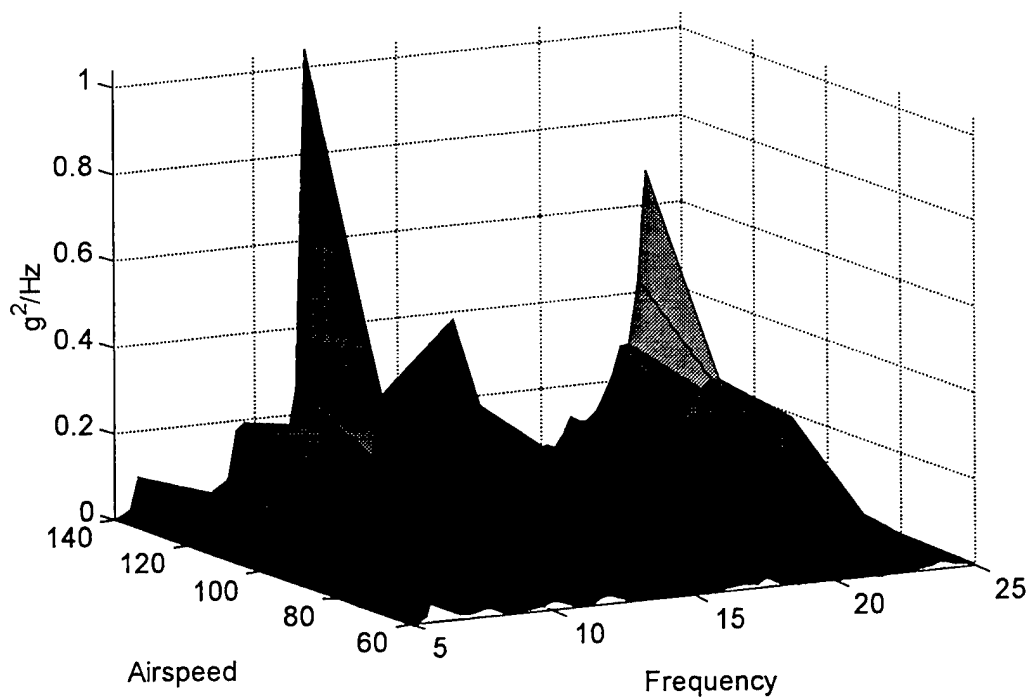


Figure 4.16: Horizontal Stab Right Tip – Vertical 5-25 Hertz.

PSD Horizontal Stab Left Tip - Longitudinal Response

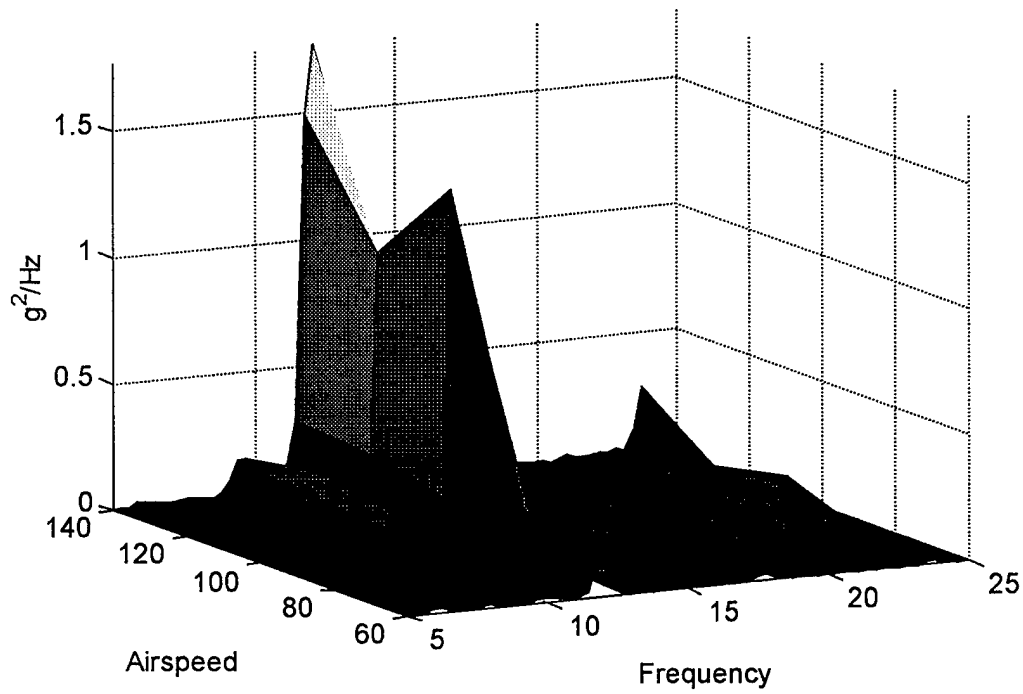


Figure 4.17: Horizontal Stab Left Tip – Longitudinal 5-25 Hertz.

PSD Horizontal Stab Right Tip - Longitudinal Response

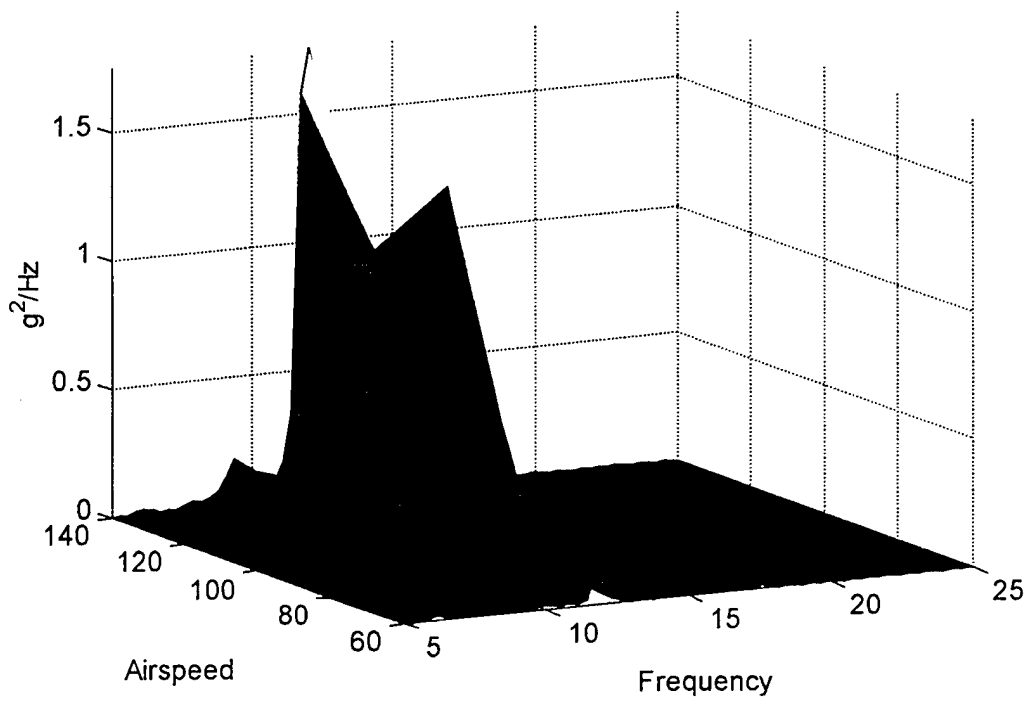


Figure 4.18: Horizontal Stab Right Tip – Longitudinal 5-25 Hertz.

From a review of the plots, there are three frequency bands that continuously display energy. Energy in this context is based upon measured vibration response data as either acceleration in g's or PSD in $(g's)^2/Hz$. The first band is centered around 5-8 Hz, the second from 10-13 Hz, and the last 22-25 Hz. From the PSD data, the RMS for each airspeed was calculated. Figures 4.19 through 4.22 show the computed RMS from the nose cone, pilot's station, and copilot's station. The RMS including and not including 5P is plotted along with both lateral and vertical response. The 5P vibration adds a significant amount to the total response and produces a sharp rise in accelerometer readings acceleration at airspeeds above 100 knots. The total response for the frequency band of 5-25 Hz begins to level off at 100 knots, the slope being much less than the RMS with 5P included. This excitation, not including 5P, is less prevalent at lower airspeeds and significantly increases from 80-100 knots. Past 100 knots, this frequency band energy begins to level off while 5P vibration levels increase significantly. By plotting both lateral and vertical RMS, comparisons as to the more dominant response can be made. Lateral to vertical ratios typically range of the order from 1.25:1 to 2.0:1. In all cases except for the pilot's floor, lateral response dominates. To capture the maximum excitation outside of the 5P range, and minimize 5P response, a more detailed analysis is presented of the PSD at 100 knots.

Figures 4.23 through 4.28 present the PSD for 100 knots. Again, both lateral and vertical responses are plotted together. As was seen in the RMS calculations, the lateral response is dominant. Additionally, the three frequency regions identified earlier are evident.

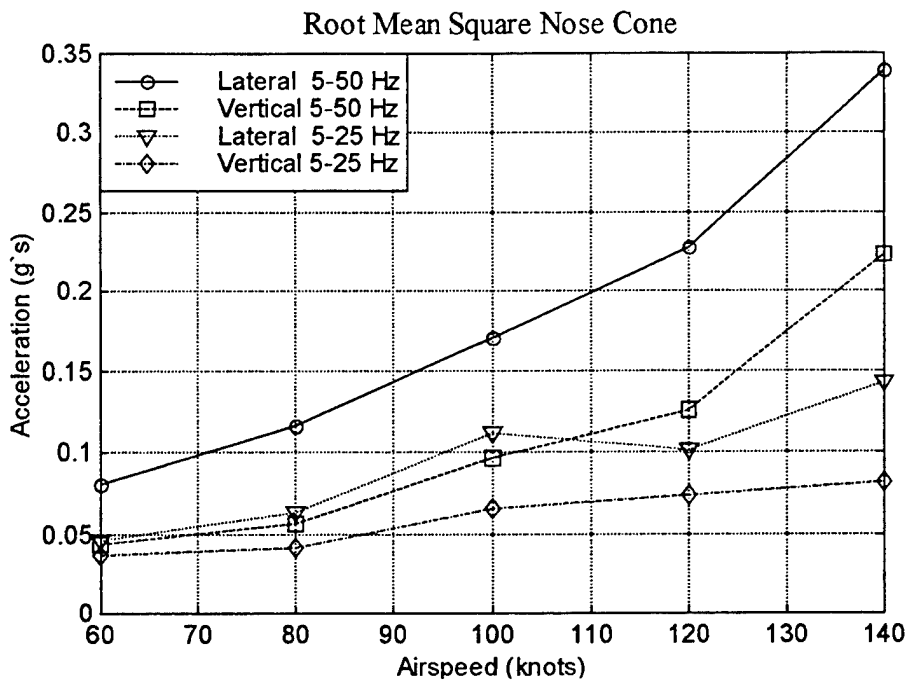


Figure 4.19: Root Mean Square – Nose Cone.

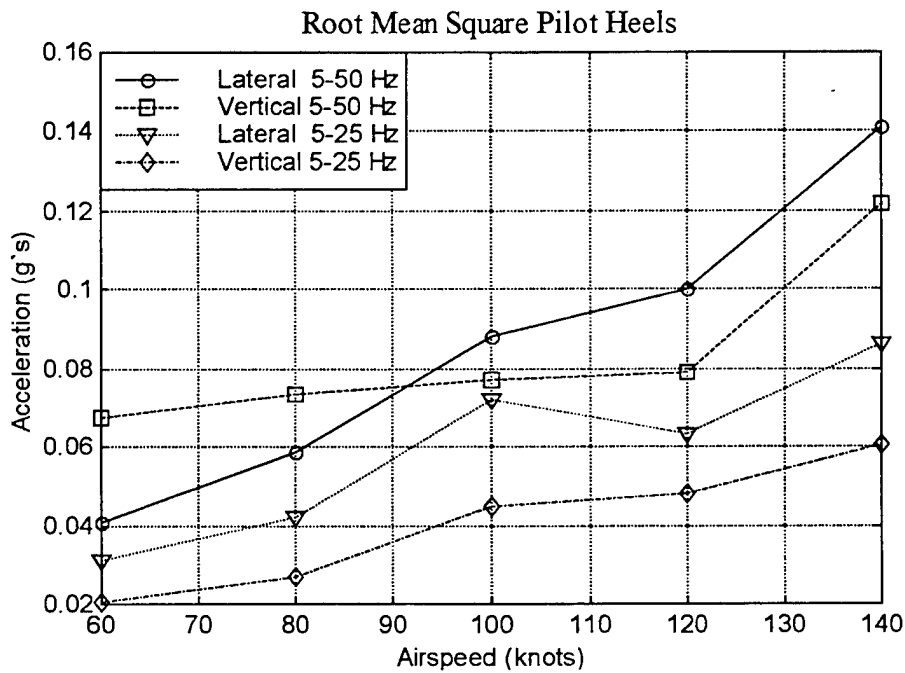


Figure 4.20: Root Mean Square – Pilot Heels.

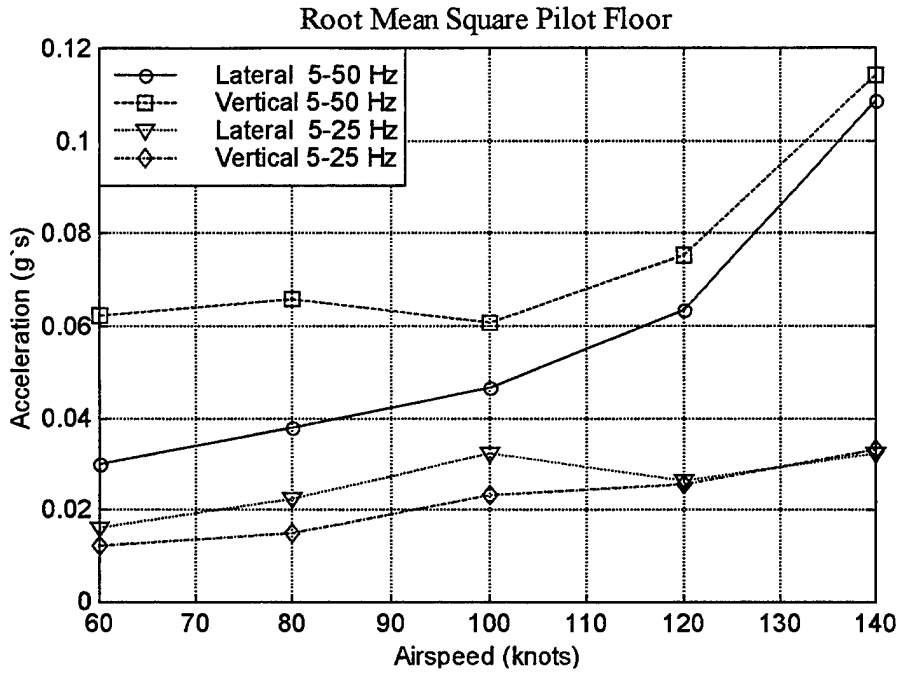


Figure 4.21: Root Mean Square: Pilot Floor.

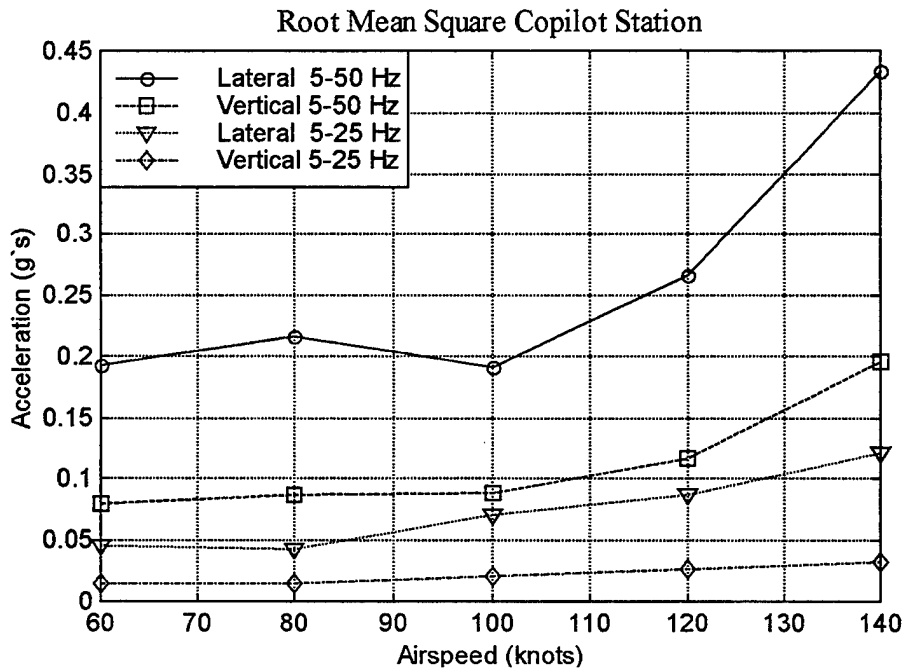


Figure 4.22: Root Mean Square – Copilot Station.

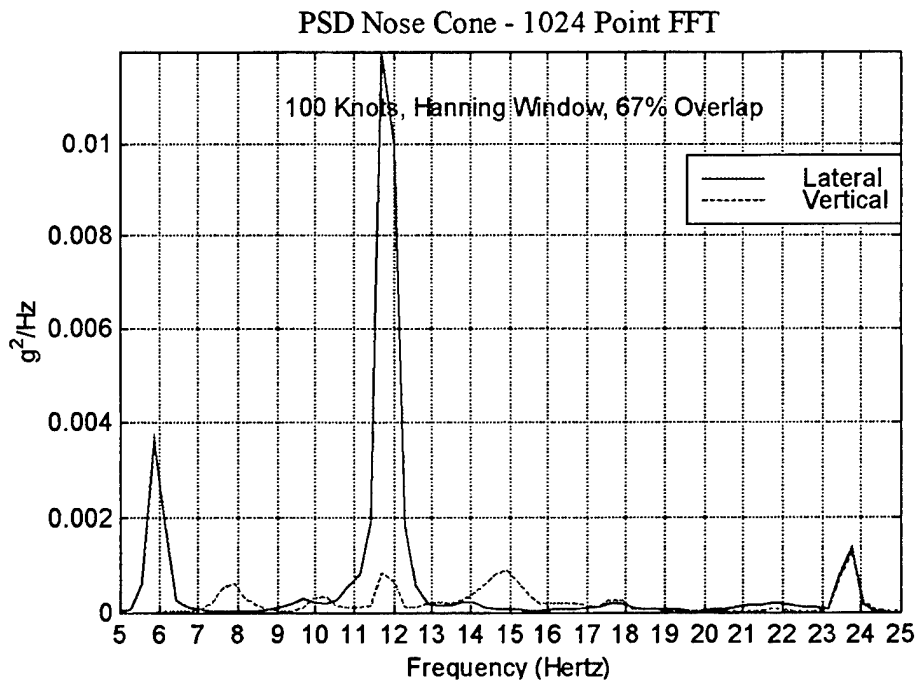


Figure 4.23: Nose Cone – 100 Knots.

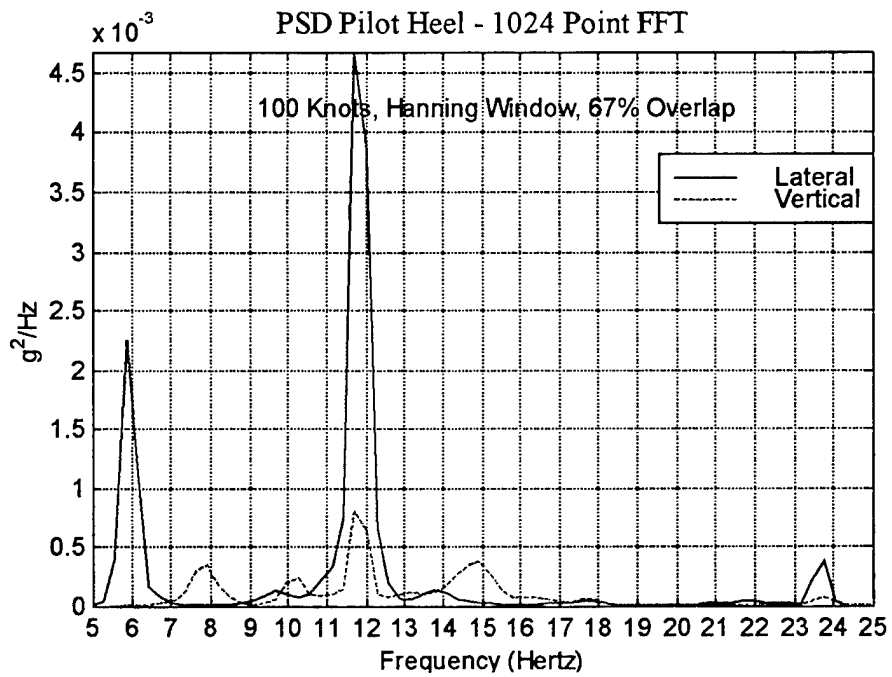


Figure 4.24: Pilot Heels – 100 Knots.

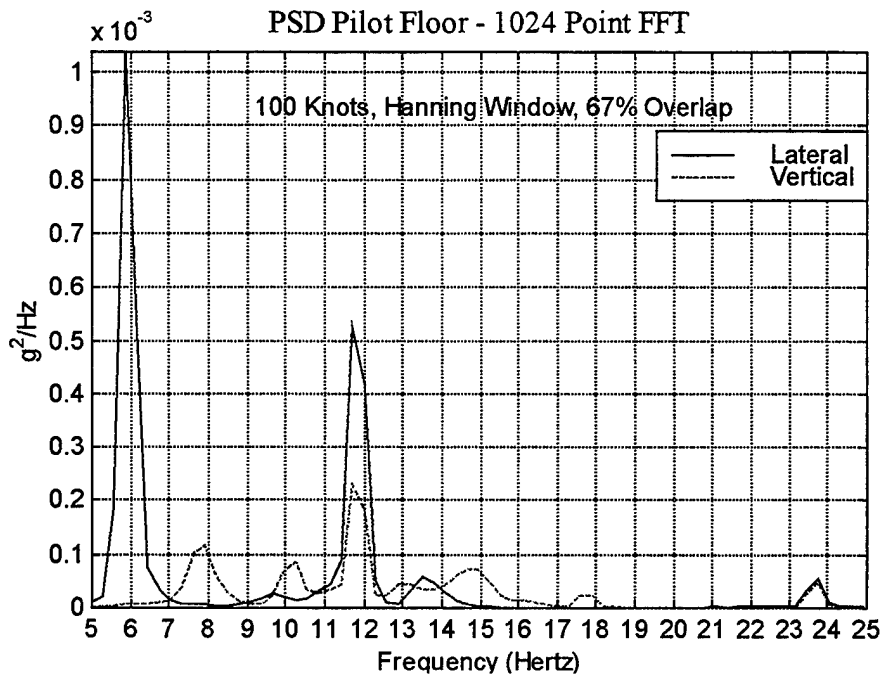


Figure 4.25: Pilot Floor – 100 Knots.

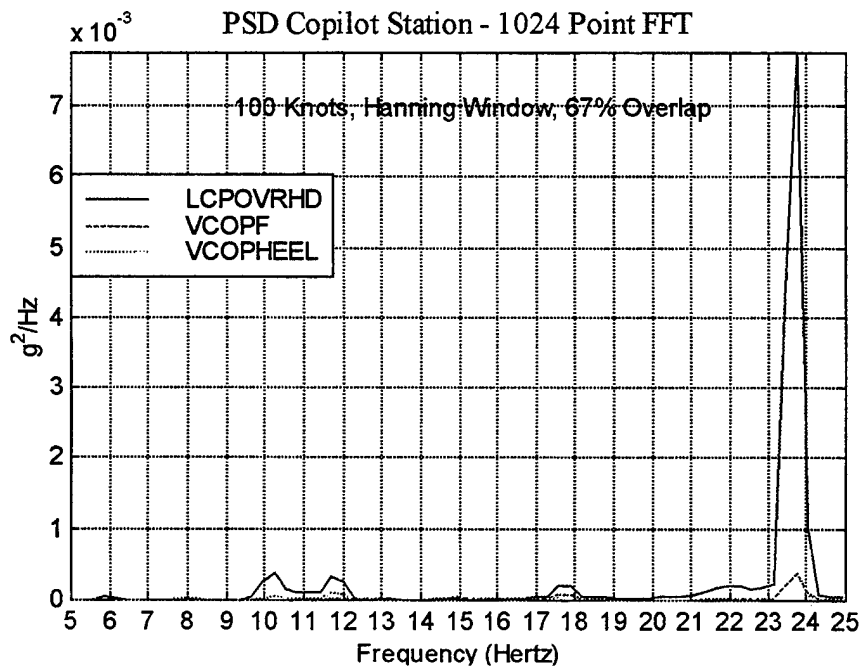


Figure 4.26: Copilot Station – 100 Knots.

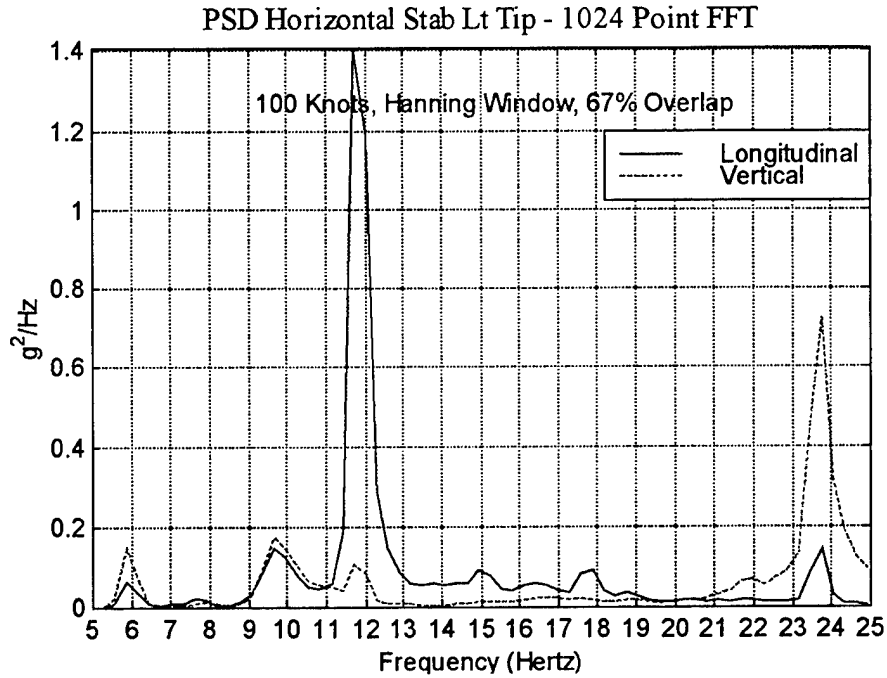


Figure 4.27: Horizontal Stab Left Tip – 100 Knots.

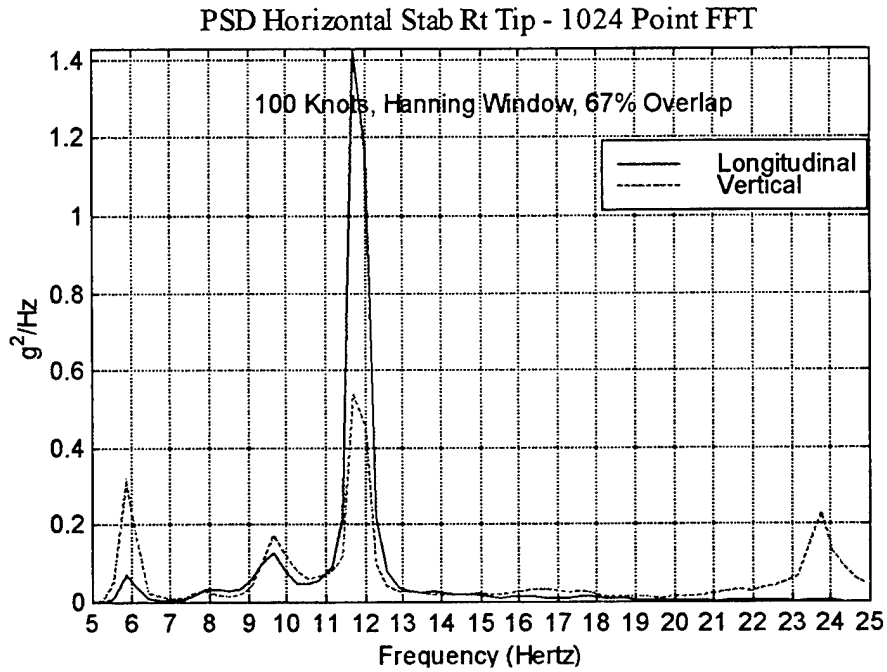


Figure 4.28: Horizontal Stab Right Tip – 100 Knots.

To quantify the amount of response due to these three frequency bands, or bins, RMS values for the discrete ranges of 5-8 Hz, 10-13 Hz, and 22-25 Hz were calculated. Each RMS value was summed and compared to the total RMS, not including 5P response. The data is presented in Table 4.2. Although these three frequency bins represent only 9 Hz, or 45% of the total bandwidth, they constitute from 50% of the total response to as much as 90%. Comparing the bins, the more dominant frequency range was 10-13 Hz, with 60% of the accelerometers having their peak response in this region.

Root Mean Square - 100 Knots - g's				
Accelerometer	Frequency Bins			% Total RMS
	5-8 Hz	10-13 Hz	22-25 Hz	
Nose Cone Vertical	0.0214	0.0310	0.0288	51.87
Nose Cone Lateral	0.0448	0.0920	0.0306	91.54
Pilot Heel Lateral	0.0352	0.0573	0.0159	92.54
Pilot Heel Vertical	0.0161	0.0283	0.0096	57.09
Pilot Floor Lateral	0.0238	0.0191	0.0058	92.73
Pilot Floor Vertical	0.0095	0.0155	0.0050	64.88
CPG Heel Vertical	0.0054	0.0103	0.0147	82.59
CPG Floor Vertical	0.0030	0.0052	0.0162	65.97
Pilot Overhead Lat	0.0215	0.0816	0.0858	88.90
CPG Overhead Lat	0.0061	0.0229	0.0647	92.54
Vert Pylon Top Lat	0.4521	0.1669	0.1024	87.02
HorStab Lt Tip Vert	0.2928	0.5035	0.8355	84.60
HorStab Rt Tip Vert	0.4284	0.7390	0.5327	81.18
HorStab Lt Tip Long	0.2325	1.0588	0.3360	75.25
HorStab Rt Tip Long	0.2354	1.0268	0.0987	86.69

Table 4.2: RMS of Frequency Bins – 100 Knots.

B. FLIGHT TEST PRESSURE MEASUREMENTS

The differential pressure transducer data records that correspond to the accelerometer data are listed in Table 4.3. The sampling rate remained 300 samples per second with a 60 second record length.

Differential Pressures	
Mnemonic	Location
VERTDP2	Differential Pressure, 7% chord, 30% up Vertical Tail
VERTDP4	Differential Pressure, 7% chord, 60% up Vertical Tail
LHORZDP3	Differential Pressure, 7% chord, 60% Span Left Horizontal Tail
RHORZDP4	Differential Pressure, 7% chord, 60% Span Right Horizontal Tail

Table 4.3: Differential Pressure Transducers.

The frequency content of the differential pressures was determined and compared to the response PSDs, findings of Leishman and Moedersheim [Ref. 4], and the approximated shedding frequency of the rotor hub pylon. The analysis also provided insight into which areas of the structure are excited. This aided in focussing the NASTRAN analysis, deriving the transfer functions between the random aerodynamic loading and the response locations, and correlation with mode shapes. This will be addressed in Chapter VI. Figure 4.29 shows the variation of differential pressure from the left horizontal stabilizer as a function of airspeed from 60 to 140 knots.

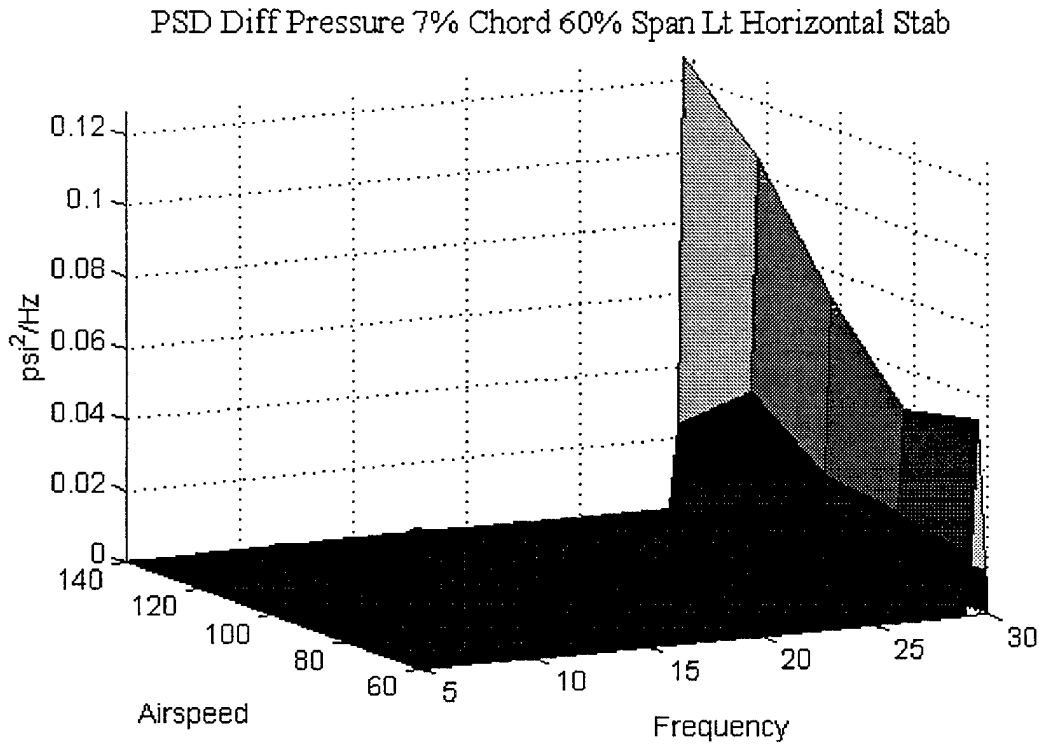


Figure 4.29: Differential Pressure - Left Horizontal Stabilizer.

As with the response data, the magnitude of the 5P differential pressure (29.85 Hz) is an order of magnitudes greater than excitation in any other frequency band. To gain a better appreciation for the vibratory pressures at other than 5P, the transducer output is plotted for the 5-25 Hz range in Figures 4.30 through 4.33.

Given are three dimensional plots of airspeed, frequency and magnitude of the PSD. The asymmetry between the left and right horizontal tail is expected due to the angle of the vertical tail. The right horizontal tail exhibited pressure spikes at the previously noted discrete frequency bands of 5-8 Hz, 10-13 Hz, and 22-25 Hz.

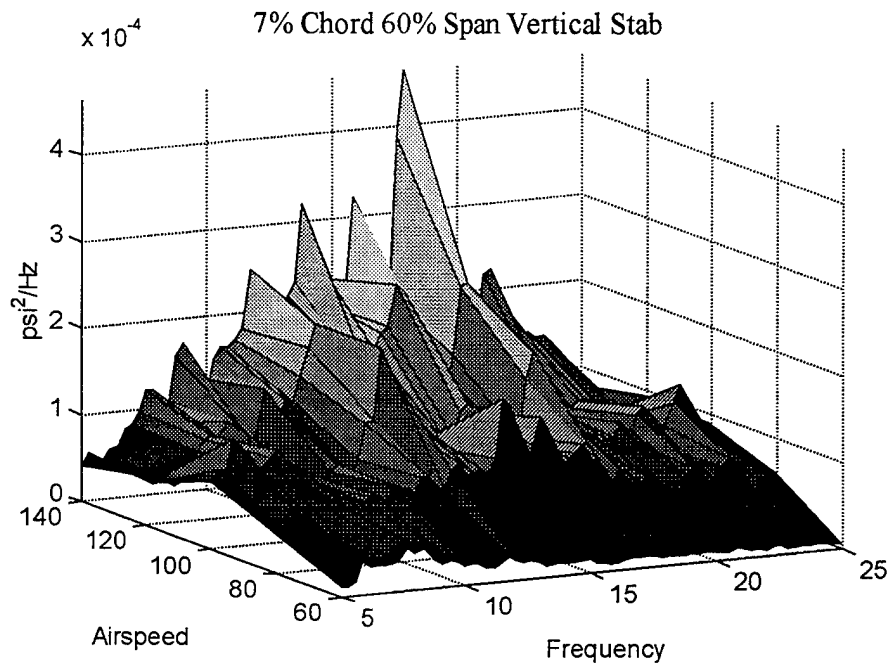


Figure 4.32: Differential Pressure – Vertical Tail.

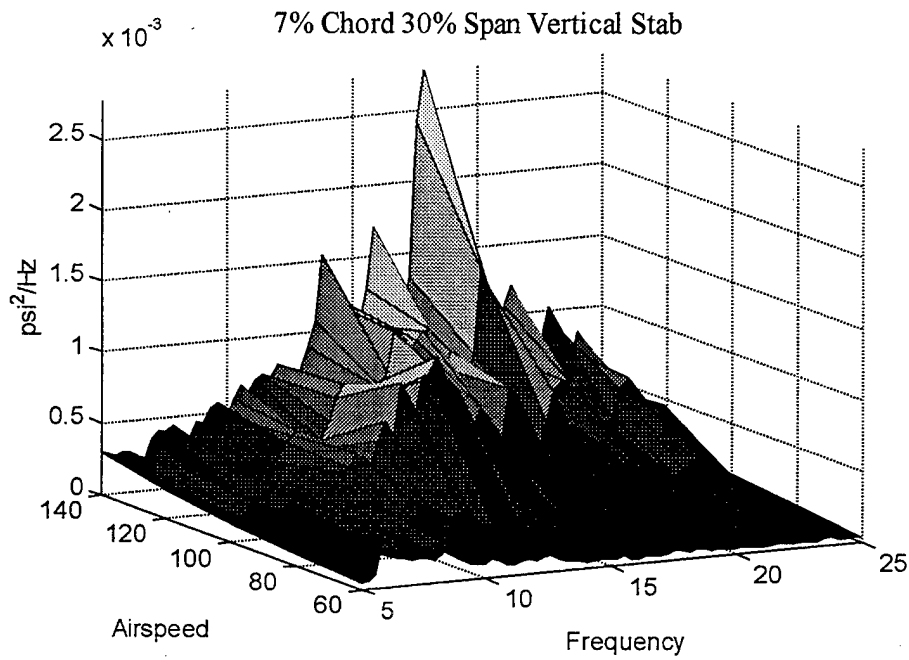


Figure 4.33: Differential Pressure - Vertical Tail.

Unlike the discrete excitation of the right horizontal tail, the left horizontal tail has broad band excitation from 11-19 Hz. Both span locations on the vertical tail show symmetry in the shape of broad band excitation, similar to that of the left horizontal. There is a decrease in magnitude, on the order of 12:1, as you move up the vertical tail, from the 30% to 60% span location.

Figures 4.34 through 4.35 are the PSDs of differential pressures at 100 knots. Both horizontal and vertical transducers are contained in the same plot for better comparison. For the horizontal tail, the magnitude of the pressures seen on the left is much greater than that of the right. The energy is peaked within the 11.5 to 14 Hz band, with an additional peak at 18 Hz. The right displays its peak pressure at 6 Hz, which corresponds with the 1P of the aircraft.

The vertical tail, at both the 30% and 60% span location, have the same frequency distribution as the left horizontal, 11.5 to 14 Hz. As seen earlier, the magnitude of the pressure continues to diminish as you move up the vertical tail. Although the pressure distribution between the vertical tail and left horizontal is similar, the pressures seen at 30% span of the vertical are 3.5 times greater than that of the left horizontal. The pressures at the 60% span of the vertical and the left horizontal are of equal magnitude.

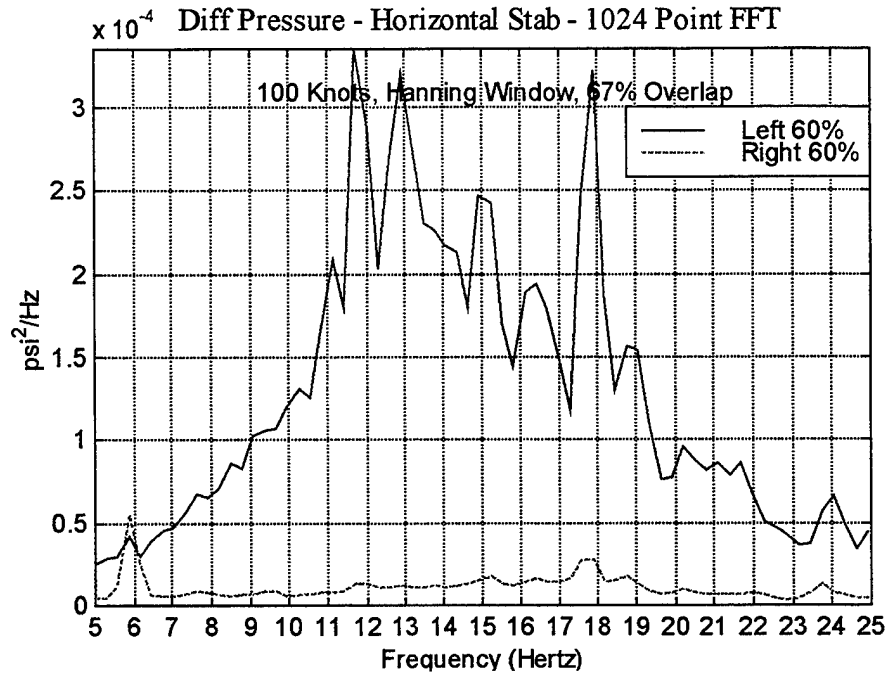


Figure 4.34: Differential Pressure Horizontal Tail - 100 Knots.

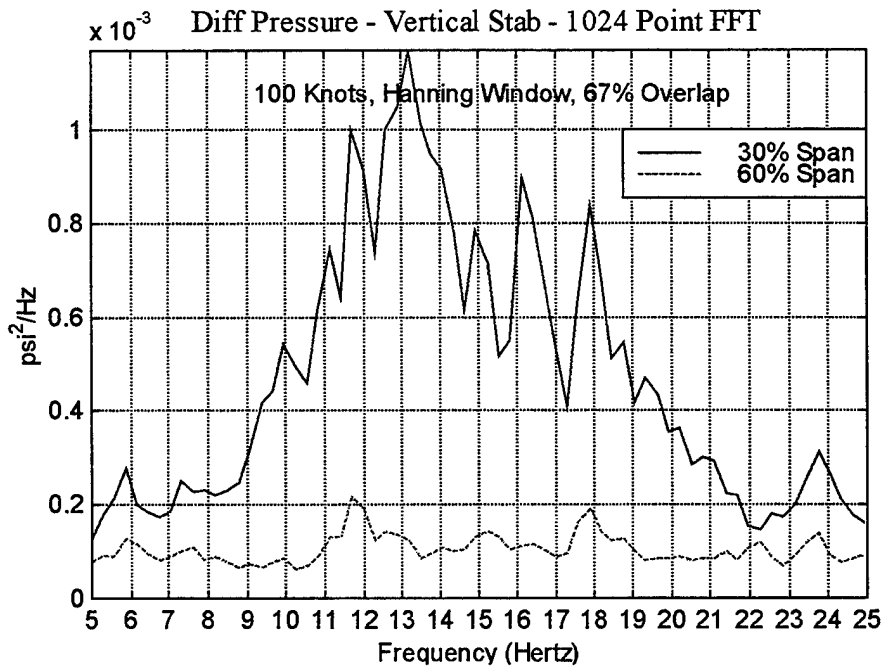


Figure 4.35: Differential Pressure Vertical Tail - 100 Knots.

Linking the pressure distributions back to response data, RMS values were calculated for the discrete frequency bins used earlier. The unit for the RMS of the pressures is psi. Table 4.4 presents both the magnitudes of pressures as you move up the vertical tail and along the horizontal as well as the dominant frequency band.

Root Mean Square - 100 Knots - psi			
Pressure Transducer	Frequency Bins		
	5-8 Hz	10-13 Hz	22-25 Hz
7% Ch 30% Sp Vert	0.0263	0.0503	0.0268
7% Ch 60% Sp Vert	0.0182	0.0206	0.0184
7% Ch 60 % Sp Lt Hor	0.0121	0.0268	0.0135
7% Ch 60% Sp Rt Hor	0.0066	0.0057	0.0048

Table 4.4: RMS of Differential Pressures – 100 Knots.

Understanding the flow over the empennage, even for the limited amount of transducers, assisted in focussing the analysis of the structural response. The following chapter presents the structural analysis and correlation between aerodynamic forces acting on the surface and response at accelerometers.

V. STRUCTURAL DYNAMICS

The dynamics of the multiple degree of freedom (MDOF) Comanche structure govern the transfer of random loads to fuselage response. In order to understand the MDOF system, the single degree of freedom case, also called a single modal oscillator, must first be studied. From these solution methods, the dynamics of the complex structure can then be quantified using a systematic modal analysis approach. Of particular interest is the response of the system to harmonic, or frequency dependent excitation. The quantity that describes this is called the frequency response function (FRF) or, from the Laplace domain, the transfer function evaluated at $(j\omega)$. Working from a vibrations perspective, the FRF for a single DOF system will be computed and then applied to a MDOF Comanche structure.

A. SINGLE DEGREE OF FREEDOM (SDOF) OSCILLATORS

The response of a single degree of freedom system to a forced harmonic excitation can be determined from the equation of motion that describes the system. The SDOF oscillator is characterized by

$$m\ddot{x} + c\dot{x} + kx = F \cos(\Omega t)$$

where

m	Total (modal) mass participating in mode of vibration
k	Total (modal)stiffness participating in mode of vibration
c	Total (modal) damping participating in mode of vibration
F	Magnitude of forcing function

The equation can then be divided by m and is in the generalized form,

$$\ddot{x} + \frac{c}{m}\dot{x} + \frac{k}{m}x = \frac{F}{m}\cos(\Omega t) \quad \text{or} \quad \ddot{x} + 2\zeta\omega_n\dot{x} + \omega_n^2x = \frac{F}{m}\cos(\Omega t)$$

The total solution is comprised of two parts:

$$x(t) = x_{\text{homo}}(t) + x_{\text{part}}(t)$$

The homogeneous solution, also known as the transient or free response is

$$x_{\text{homo}}(t) = e^{-\zeta\omega_n t} (C_1 \cos(\omega_d t) + C_2 \sin(\omega_d t))$$

where the constants C_1 and C_2 are determined by applying initial conditions. The particular solution is found for a specified forcing function. In the case of a cosine forcing function, the solution is

$$x_{\text{part}}(t) = A \cos(\Omega t - \Phi)$$

and the system responds at the frequency of excitation, Ω .

To solve for the amplitude and phase of the response, A and φ , complex algebra is used and the general forcing function becomes

$$F(t) = \bar{F}e^{j\Omega t} = \bar{F}(\cos(\Omega t) + j \sin(\Omega t)) \text{ where } \bar{F} = \frac{F}{m}$$

With this definition, the general equation for the forced response becomes

$$\ddot{x} + 2\zeta\omega_n\dot{x} + \omega_n^2x = \bar{F}e^{j\Omega t}$$

and if the assumed solution for the particular solution is

$$x_{\text{part}}(t) = Ae^{j\Omega t}$$

the necessary derivatives can be taken to find A in terms of known quantities

$$(-\Omega^2 + 2\zeta\Omega\omega_n j + \omega_n^2)A = \bar{F}$$

dividing by the natural frequency squared, ω_n^2 and grouping the real and imaginary parts,

$$\left[\left(1 - \frac{\Omega^2}{\omega_n^2} \right) + 2\zeta \frac{\Omega}{\omega_n} j \right] A = Z(\Omega) \bullet A = \bar{F}$$

with the force amplitude redefined as

$$\frac{\bar{F}}{\omega_n^2} = \frac{F}{k} \Rightarrow \bar{F}$$

The terms inside the brackets represent the complex frequency dependent constant, $Z(\Omega)$, known as the impedance, which is a function of the frequency Ω . The equation can also be written in the form

Converting to polar form and dividing magnitudes and subtracting angles, a solution for A

$$[Z_{\text{real}}(\Omega) + jZ_{\text{imag}}(\Omega)]A = \bar{F}$$

is obtained

$$A = \frac{\bar{F}}{\sqrt{Z_{\text{real}}(\Omega)^2 + Z_{\text{imag}}(\Omega)^2}} e^{j(0-\Phi)}$$

The modal parameters defined in our equation of motion can be substituted in to yield

$$A = \frac{\bar{F}}{\sqrt{\left(1 - \frac{\Omega^2}{\omega_n^2}\right)^2 + \left(2\zeta \frac{\Omega}{\omega_n}\right)^2}} e^{-j\Phi} \quad \text{where} \quad \Phi = \tan^{-1} \left(\frac{2\zeta \frac{\Omega}{\omega_n}}{1 - \frac{\Omega^2}{\omega_n^2}} \right)$$

The particular solution is then defined as

$$x_{\text{part}}(t) = |A| e^{j(\Omega t - \Phi)} = |A| (\cos(\Omega t - \Phi) + j \sin(\Omega t - \Phi))$$

As the forcing function was a cosine function, only the real part is taken and the general solution is

$$x_{\text{part}}(t) = |A| \cos(\Omega t - \Phi)$$

The amplitude of the steady state response is given by

$$|A| = \frac{\bar{F}}{\sqrt{\left(1 - \frac{\Omega^2}{\omega_n^2}\right)^2 + \left(2\zeta \frac{\Omega}{\omega_n}\right)^2}} \quad \text{where} \quad \bar{F} = \frac{F}{k}$$

If the amplitude is then normalized by the static displacement F/k , the frequency response function (FRF) is found

$$H(\Omega) = \frac{1}{\sqrt{\left(1 - \frac{\Omega^2}{\omega_n^2}\right)^2 + \left(2\zeta \frac{\Omega}{\omega_n}\right)^2}}$$

The FRF can then be used to relate any forcing function at a given frequency to the output. If the forcing function is defined as $F(\Omega)$ and the output, say displacement, is $Y(\Omega)$, then the relationship between the two is given by

$$Y(\Omega) = H(\Omega)F(\Omega)$$

B. MODAL ANALYSIS

Knowing how to solve for the FRF of a SDOF system, these methods can be applied to the MDOF systems used to represent complex structures. In order to solve the coupled set of equations associated with MDOF systems, they first must be decoupled into single DOF modal oscillators. Each modal oscillator is then solved in the procedure just described and then combined to form the total solution. This method is called mode superposition and is consistent with the matrix methods currently used for most structural analysis. [Ref. 9]

If the MDOF structure is defined as a set of $N \times N$ coupled equations represented by

$$[\mathbf{M}]\{\ddot{\mathbf{x}}\} + [\mathbf{C}]\{\dot{\mathbf{x}}\} + [\mathbf{K}]\{\mathbf{x}\} = \{\mathbf{F}(t)\}$$

The solution to this equation is first found by solving the homogeneous eigenvalue problem with no damping, C. Substituting an assumed solution of the form $\{\mathbf{x}\} = \{\phi\} Q e^{j\omega t}$ and dividing by the mass, the eigenvalue problem is defined as

$$[[\mathbf{M}]^{-1} [\mathbf{K}] - \omega^2 [\mathbf{I}]]\{\Phi\} = \{0\}$$

The non-trivial solution of the eigenvalue problem produces a vector of length N that contains the natural frequencies squared, ω_n^2 with units of $(\text{rad}/\text{sec})^2$. The mode shapes, or eigenvectors $\{\phi\}$, can be easily solved for and combined into the modal matrix.

$$[\Phi] = [\{\Phi^1\} \{\Phi^2\} \{\Phi^3\} \dots \{\Phi^N\}]$$

The modal matrix, although not an orthogonal matrix, is orthogonal with respect to the mass and stiffness matrix. As such, the mass and stiffness matrices can be transformed by the modal matrix to diagonal matrices that decouple the equations of motion and yield N - SDOF modal oscillators. The coordinate system must also be transformed to modal coordinates, q

$$\{x\} = [\Phi]\{q\}$$

Pre-multiplying by the transpose of the modal matrix and substituting for x , the equation of motion, minus the damping becomes

$$[\Phi]^T [\mathbf{M} \Phi] \{\ddot{q}\} + [\Phi]^T [\mathbf{K} \Phi] \{q\} = [\Phi]^T \{F\}$$

Defining the modal mass, stiffness, and force as

$$[\Phi]^T [\mathbf{M} \Phi] = [\tilde{\mathbf{M}}], \quad [\Phi]^T [\mathbf{K} \Phi] = [\tilde{\mathbf{K}}], \quad \{\tilde{F}\} = [\Phi]^T \{F\}$$

The modal equation of motion is

$$[\tilde{\mathbf{M}}]\{\ddot{q}\} + [\tilde{\mathbf{K}}]\{q\} = \{\tilde{F}\}$$

These diagonal matrices now represent the N modal oscillator SDOF equations of motion.

A solution for each can easily be obtained.

Damping is re-introduced on a modal basis. As each differential equation is solved, the damping associated with that particular natural frequency, or mode, is applied. This is consistent with the techniques used in parameter identification where damping ratios are determined on a modal basis. The response in physical coordinates is found by multiply each modal solution by the modal matrix

$$\{\mathbf{x}\} = [\Phi]\{q\}$$

If interested in the frequency response function (FRF) between only certain points, i and j , on an MDOF system, the following method is used

$$\mathbf{H}_{ij}(\Omega) = \sum_{r=1}^{\text{"p" modes}} \frac{\Phi_i^r \Phi_j^r}{\omega_r^2 - \Omega^2 + j2\zeta_r \omega_r \Omega}$$

Once the FRF is known for those points, the magnitude of the response, A , due to a harmonic excitation of amplitude F and at a driving frequency of Ω , can be determined by multiplying the FRF and F .

C. RIGID BODY MODES

Unconstrained systems have rigid body modes. This occurs when the structure translates or rotates without any deformation. Numerically, this appears in the solution as natural frequencies, ω_n , of zero. The reason for this is based on the relationship between the stiffness matrix, \mathbf{K} , and the strain energy of the system. If the MDOF system moves without deforming, no strain energy is produced. The stiffness matrix, \mathbf{K} , becomes positive semi-definite with a determinate of zero. As such, the solution to the eigenvalue problem has as many trivial solutions, zero, as there are rigid body modes. For an aircraft, there are six rigid body modes, which is the case for the dynamics of any body in three-dimensional space.

D. FINITE ELEMENT MODELING

To determine the frequency response functions using modal analysis, the Comanche structure was modeled using the software package NASTRAN. The National Aeronautics and Space Administration (NASA) initially developed NASTRAN in the 1960s. NASTRAN is an acronym for NASA STRUCTURAL ANALYSIS. Originally written in FORTRAN, it uses the finite element method (FEM) to analyze structural models [Ref. 10]. The foundation of this is the discretization of the structure's stiffness and mass. The FEM provides the basis for algorithms that can efficiently analyze complex structures such as the Comanche. A detailed discussion of the Finite Element method and its relationship to structural dynamics is contained in Reference 11. NASTRAN version 70 was used for this analysis.

The results generated using NASTRAN were viewed using PATRAN 7.0, an integrated computer-aided engineering (CAE) tool. The menu-driven graphical interface makes model manipulation easy and aids in visualization of mode shapes and model geometry.

VI. RAH-66 NASTRAN ANALYSIS

A NASTRAN finite element model of the RAH-66 was provided by Sikorsky. This model, yrahj157_reinf_2kg.dat, was modified by engineers at Boeing to replicate the configuration of the prototype aircraft. The name of the model is very important as Sikorsky manages many configurations and models, each with different stiffness and mass properties. The model used in this analysis included additional stiffening to the tail of the aircraft and 2.2 kg tip weights on both sides of the horizontal tail. With this, the natural frequencies, mode shapes, and frequency response functions (FRF) could be determined that most closely represented the actual aircraft. This was critical as these FRFs were later used with accelerometer and pressure transducer data to compute estimates of the loads. A PATRAN representation of the NASTRAN model is shown in Figure 6.1.

A. NATURAL FREQUENCIES

Hover frequency response testing of the test flight aircraft was conducted at West Palm Beach to support aeroservoelastic analysis. The purpose was to identify actual natural frequencies and modal damping. Through flight control frequency sweeps from 5-15 Hz, actual fuselage natural frequencies and percent critical damping were determined for selected modes.

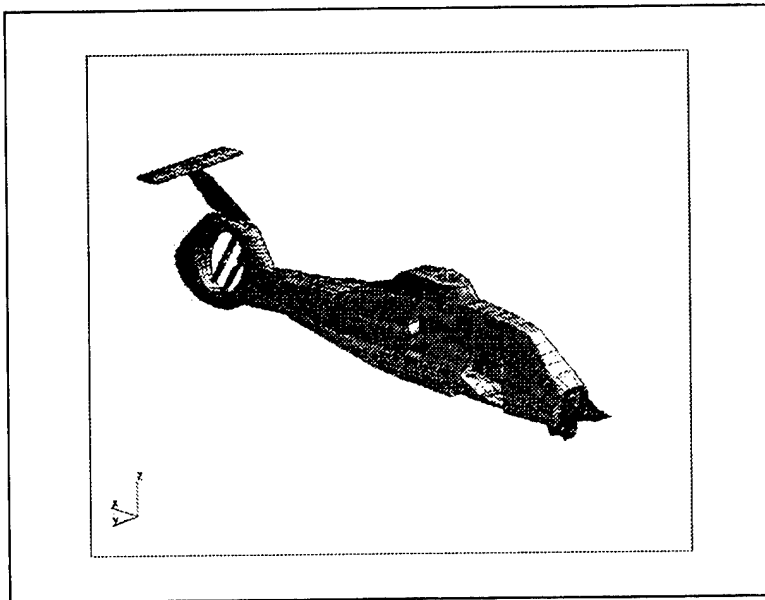


Figure 6.1: RAH-66 NASTRAN Model.

Rather than adjusting the stiffness and mass properties of the NASTRAN model to return the actual natural frequencies, engineers at Boeing demonstrated that if the mode shapes from the original NASTRAN model were used along with adjusted natural frequencies, the resulting displacements and accelerations matched actual test flight response data. The method used to accomplish that was to first run the NASTRAN analysis deck. Then, during a restart using DMAP commands, the eigenvalue matrix (representing NASTRAN natural frequencies) was altered to actual frequencies. The resulting accelerations from application of harmonic loads closely matched actual response due to harmonic sweeps of the tail fan. Table 6.1 displays the NASTRAN natural frequencies and actual natural frequencies and damping, for selected modes, as determined from flight test.

Mode	NASTRAN Freq (Hz)	Description	Flight Test	
			Freq (Hz)	Damping % Critical
7	6.32	Aft Fuselage Lat/Torsion	6.00	
8	7.77	Fuselage Vertical Bending	7.70	2.34%
9	8.53	Pilot Vert/Pitch		
10	8.70	Pilot Lat/Yaw		
11	10.24	Horiz Stab Roll	9.50	2.90%
12	10.88	Copilot Vert/Pitch		
13	10.98	Copilot Lat/Yaw		
14	12.84	Horiz Stab Yaw	11.60	3.33%
15	13.67	Tail Rotor Drive Shaft Mode		
16	14.52	2 nd Fuselage Vertical		
17	14.99	Quill Shaft		
18	15.75	Tail Rotor Drive Shaft		
19	15.95	Fuselage Head Vertical		
20	16.07	2 nd Fuselage Lateral		
21	16.55	Pilot Seat Lateral Roll		
22	16.84	Main Xmsn Lat/Roll		
23	17.10	Tail Rotor Drive Shaft		
24	17.82	Tail Rotor Drive Shaft		
25	18.24	Ammo Bay		
26	18.82	Copilot Lat/Roll		
27	18.89	Main Xmsn Lat/Roll		
28	20.45	Fuselage Mode		
29	21.12	Pilot Seat		
30	21.56	Stab Vertical Bending		
31	21.78	Tail Rotor Driveshaft		
32	21.80	Head Lateral		
33	21.87	Tail Rotor Driveshaft		
34	23.05	Copilot Sidearm		
35	24.02	Weapons Door		
36	24.04	Fuselage		
37	24.23	Weapons Door		
38	24.53	ECU Mode		
39	24.61	Pilot Seat/Sidearm		
40	24.74	Canopy		

Table 6.1: Aircraft Natural Frequencies.

B. MODE SHAPES

Selected mode shapes for free response from the original NASTRAN solution are contained in Appendix C. Again, as the flight test derived natural frequencies were only slightly different from the NASTRAN frequencies, it is assumed that the NASTRAN mode shapes are accurate. Three critical mode shapes are shown in Figure 6.2 through 6.5. The first two mode shapes were identified in test flight and have large lateral response in frequency bins previously discussed. The third mode shape is outside of the frequency range; however it correlates well with the response seen in the 22-25 Hz range.

Figure 6.2 is the aft fuselage lateral torsion mode. This motion is consistent with the accelerometer output in the 5-8 Hz bandwidth. Referring to Table 4.2, correlation can be made between the flight test output and the free response. There is large response in this frequency bin from the accelerometer at the top of the vertical stabilizer. This same motion occurs in the 6 Hz mode shape.

The horizontal stabilizer yaw mode at 11.6 Hz, displayed in Figure 6.3, has significant lateral response at the base of the vertical tail and at both the pilot station and nose cone. The RMS of accelerometer output from both the pilot station and nose cone have the largest magnitude in the 10-13 Hz bandwidth.

There is no mode shape within the 22-25 Hz bandwidth that correlates well with the flight test data. Figure 6.4 shows the horizontal stabilizer bending mode at 26.02 Hz. In the baseline NASTRAN model, yrahj170, the frequency is 22.08 Hz. This response is consistent with flight data and is characterized by vertical motion of the horizontal stabilizer and lateral response of the CPG station and pilot overhead.

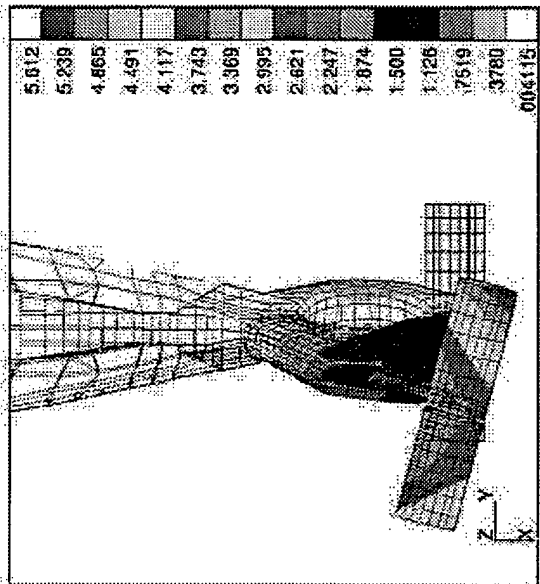
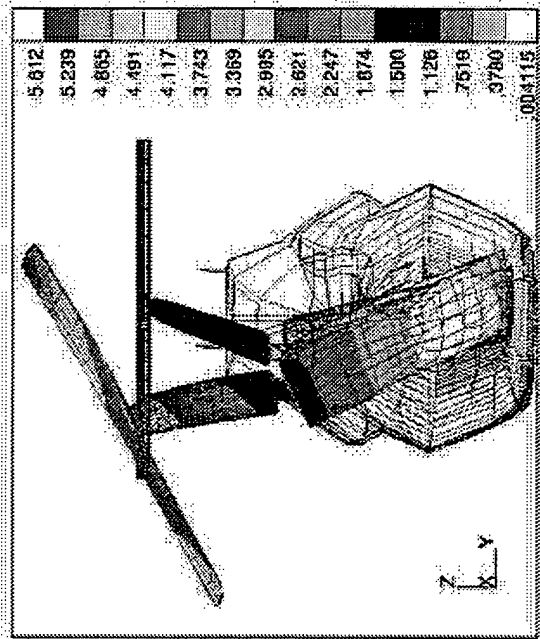
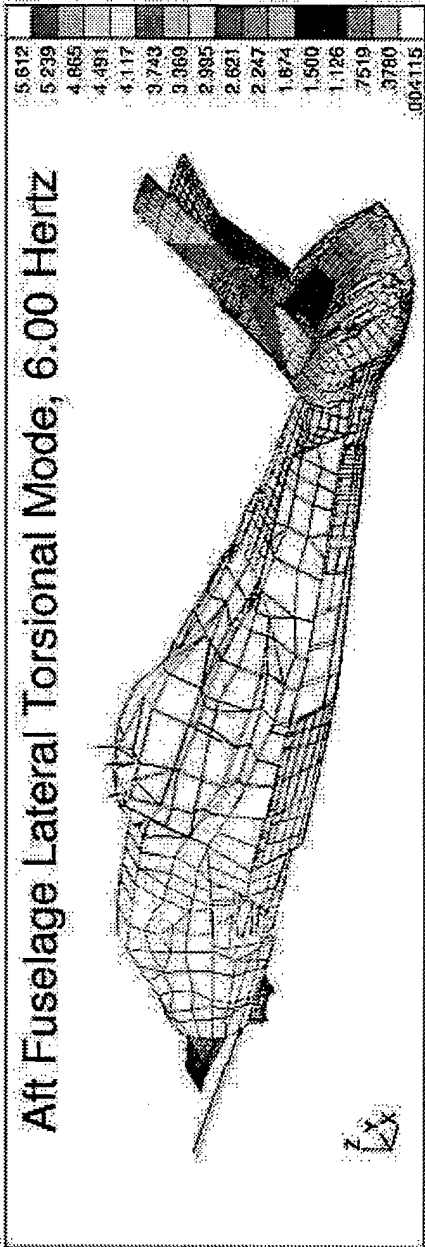


Figure 6.2: Aft Fuselage Lateral Torsion Mode Shape.

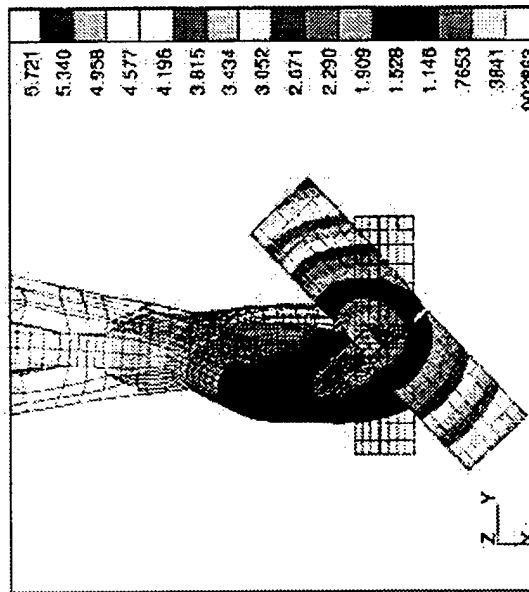
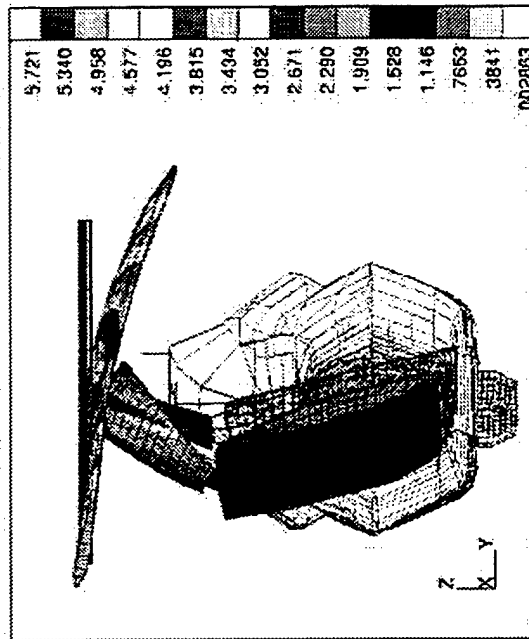
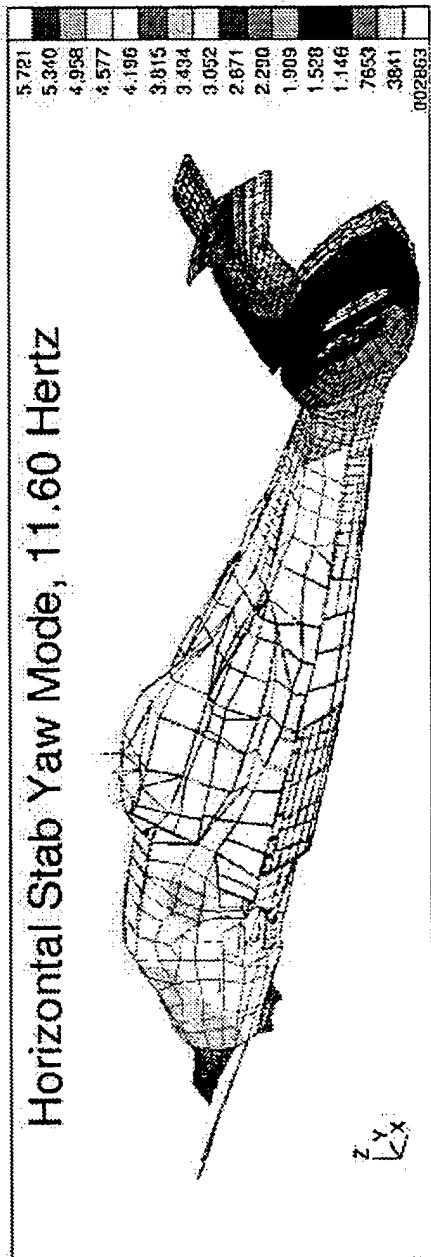


Figure 6.3: Horizontal Stabilizer Yaw Mode Shape.

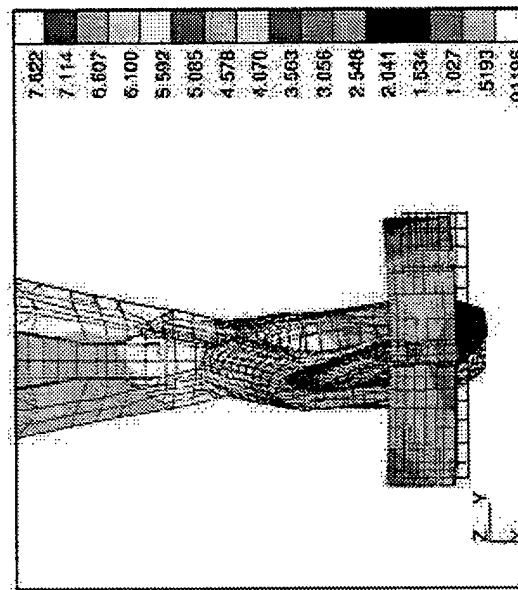
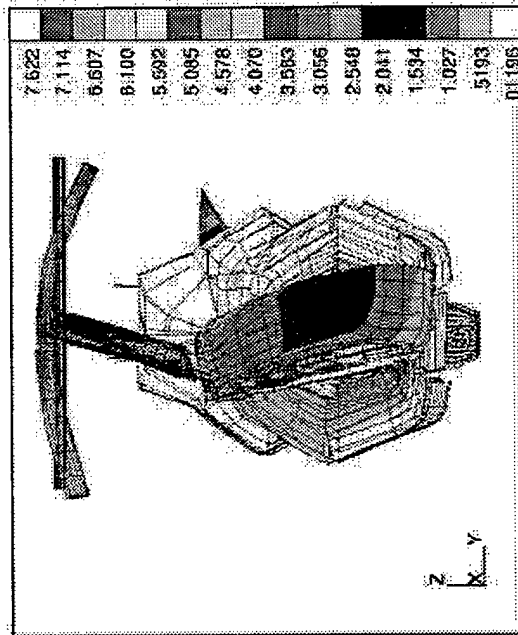
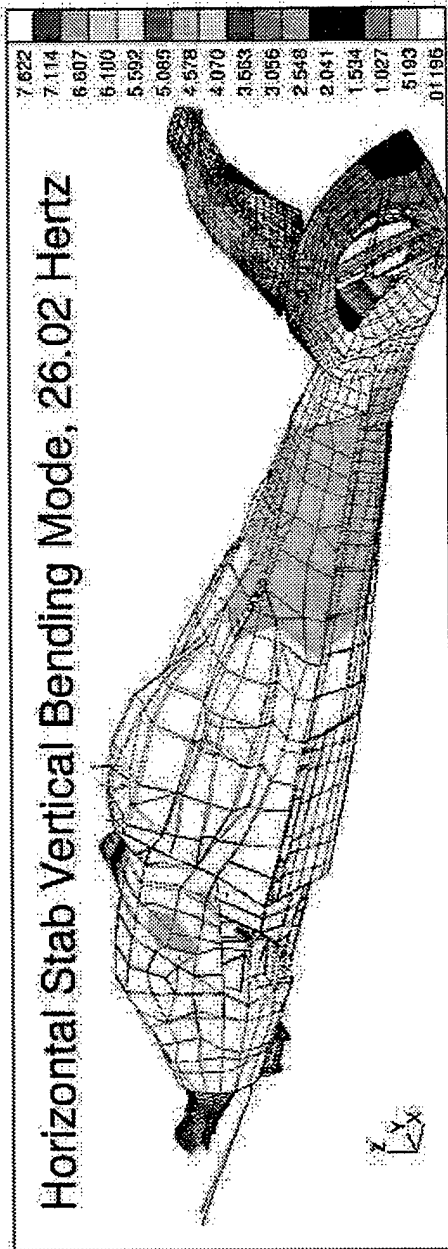


Figure 6.4: Horizontal Stabilizer Vertical Bending Mode.

C. FREQUENCY RESPONSE FUNCTIONS

Frequency response functions were determined between the horizontal and vertical tail and accelerometers. To compute the FRFs, accelerometer locations had to be correlated to NASTRAN grids. Sikorsky provided a list, contained in Appendix D, of accelerometer locations and suggested NASTRAN grids. A partial list of the NASTRAN grid points used is shown in Table 6.2.

Accelerometer/NASTRAN Correlation	
Location	NASTRAN Grid
Nose Cone	61641
Pilot Heel	6505
Pilot Floor	7246
Copilot Heel	7608
Copilot Floor	8948
Pilot Overhead	7514
Copilot Overhead	8614
Vertical Pylon Top	32341
Hor Stab Left Tip	41108
Hor Stab Right Tip	48108

Table 6.2: Accelerometer Locations in NASTRAN Model.

A one pound force was applied at these nodes with a frequency sweep of 5-25 Hz. Accelerations, in g's and in all three directions, were found at each accelerometer location. The FRFs were written to a .pch file, converted into matrices compatible with MATLAB, and stored as .mat files for use in solving for PSDs and CSDs of loads.

1. Horizontal Tail

The NASTRAN nodes along the quarter chord of the horizontal tail are shown in Figure 6.5. Only one loading condition, loads applied in the z direction, was used. In addition to determining the FRF at each grid point along the quarter chord and the accelerometer locations, a chordwise investigation was conducted. At five different span locations, the FRF was found for each node along the chord. This provided no additional information as the FRF varied minimally from leading edge to trailing edge. Therefore, it is not included.

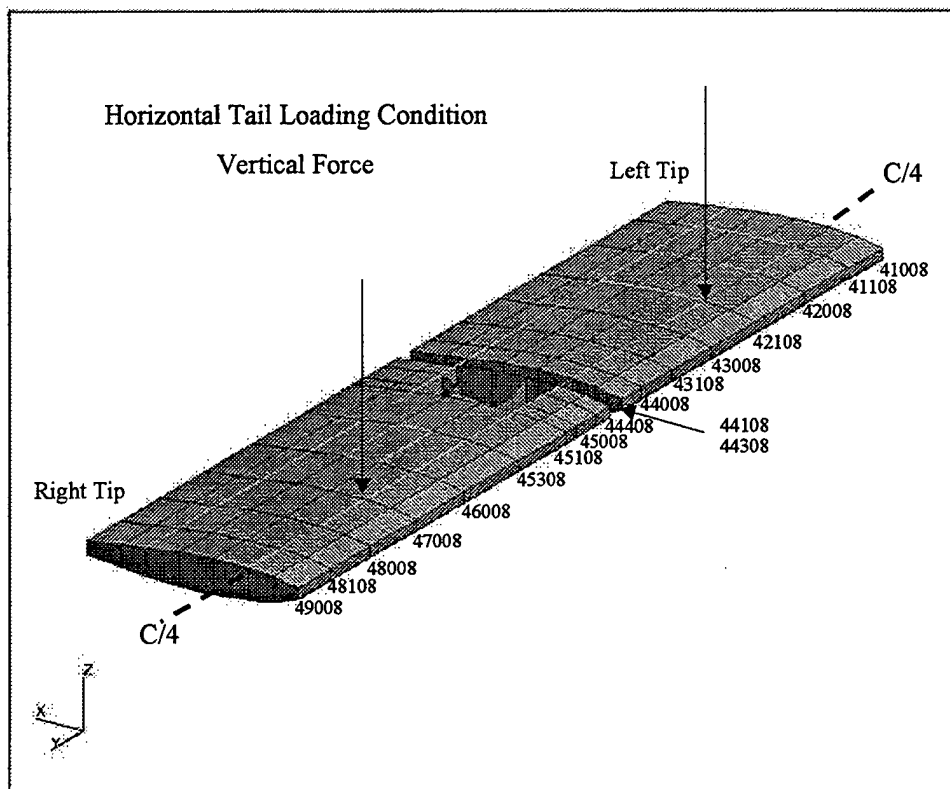


Figure 6.5: Horizontal Tail Nodes and Loading Condition.

Figures 6.6 and 6.7 show the FRF between the horizontal stabilizer and the pilot heels lateral and vertical. Although the FRF was determined from 5-25 Hz, the magnitude beyond 20 Hz was extremely small. For better resolution in the plot, the axis was reduced to 5-20 Hz. The span axis represents every node along the quarter chord, with the right tip defined as 0% span and the left tip representing 100%. As expected, the peak FRFs are aligned with the natural frequencies.

In Figure 6.6, the lateral FRF has the greatest magnitude at 6 Hz on the right tip of the stabilizer. All other FRFs are less than this value. As the load was moved along the tail, the magnitude continued to decrease until a minimum at mid-span. This is expected as loads directly over the vertical tail induce very small moments, and the lateral motion throughout the fuselage reduces. Continuing out the left horizontal, the magnitude continues to increase; however, never reaches the amplitude from the right side.

Figure 6.7 shows the FRF between the applied load and the vertical acceleration at the pilot heels. The FRF does have symmetry across the tail; however, the magnitude is substantially less than the lateral.

Figures 6.8 and 6.9 display the FRF between the same points but at the discrete frequencies of 6 and 11.6 Hz. The magnitude was normalized to the maximum amplitude FRF. Comparisons can now be more easily drawn for relative values of each FRF. These plots indicate the significant role the right side of the horizontal tail plays in transferring energy at both 6 and 11.6 Hz.

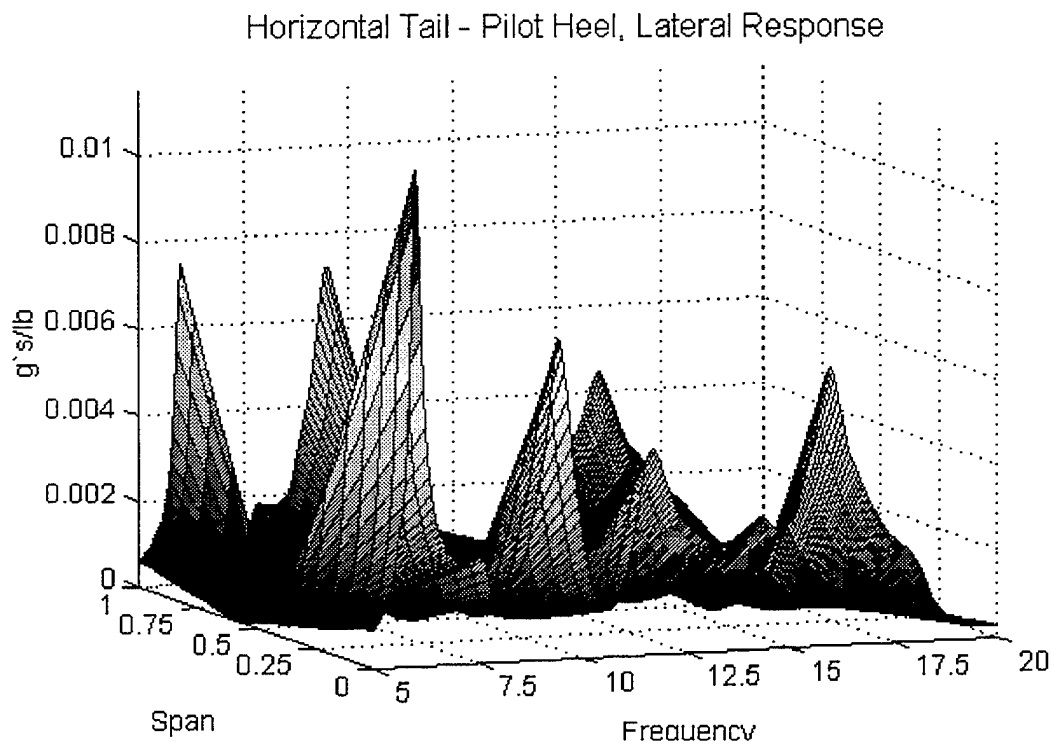


Figure 6.6: FRF Horizontal Tail to Pilot Heel - Lateral Response.

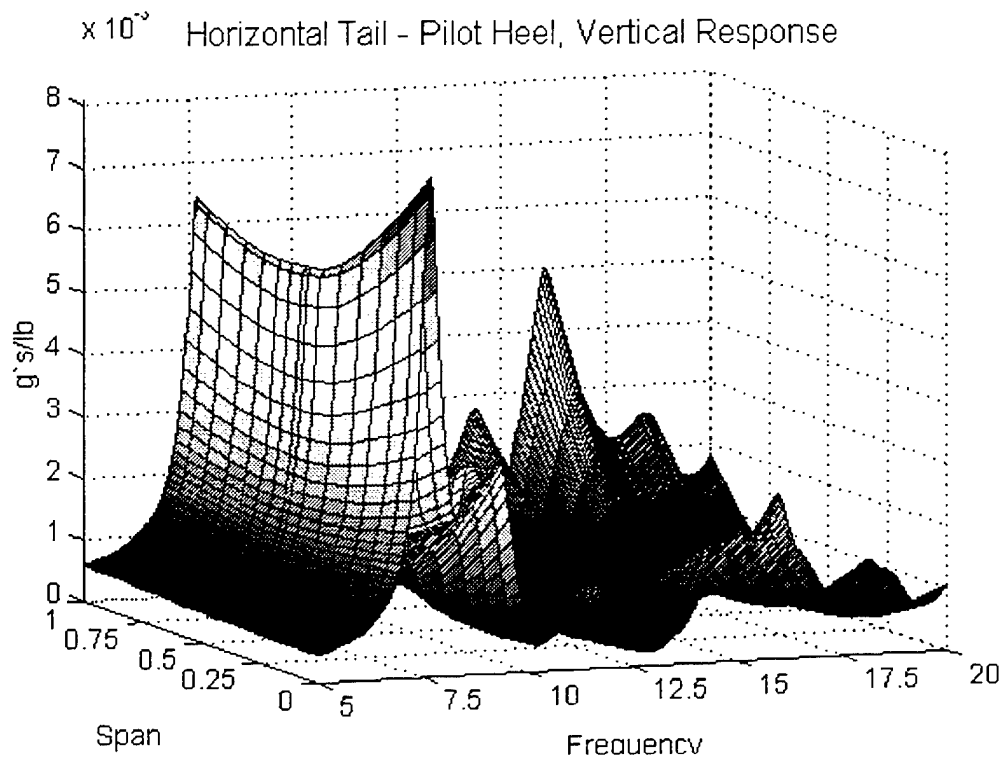


Figure 6.7: FRF Horizontal Tail to Pilot Heel – Vertical Response.

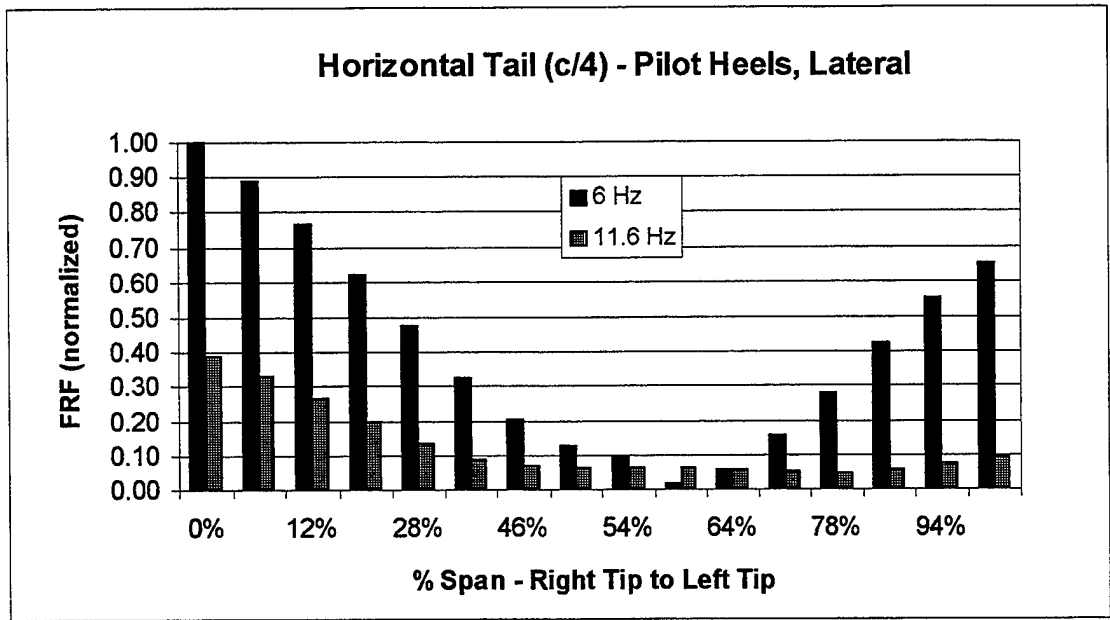


Figure 6.8: FRF Horizontal Tail to Pilot Heel – Lateral.

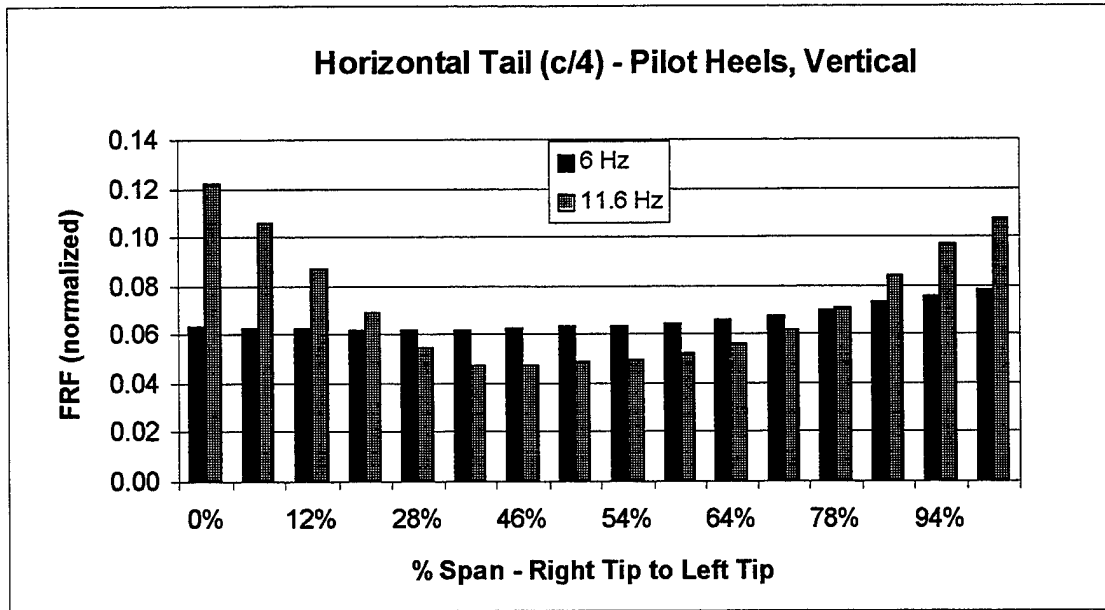


Figure 6.9: FRF Horizontal Tail to Pilot Heel – Vertical.

2. Vertical Tail

The loading condition and NASTRAN nodes along the quarter chord of the vertical tail are shown in Figure 6.10. Again, only one loading condition, loads applied in the y direction, was used. As with the horizontal tail, a chordwise investigation was conducted. Similarly, the FRF chordwise at five span locations varied only slightly. Those results are not presented.

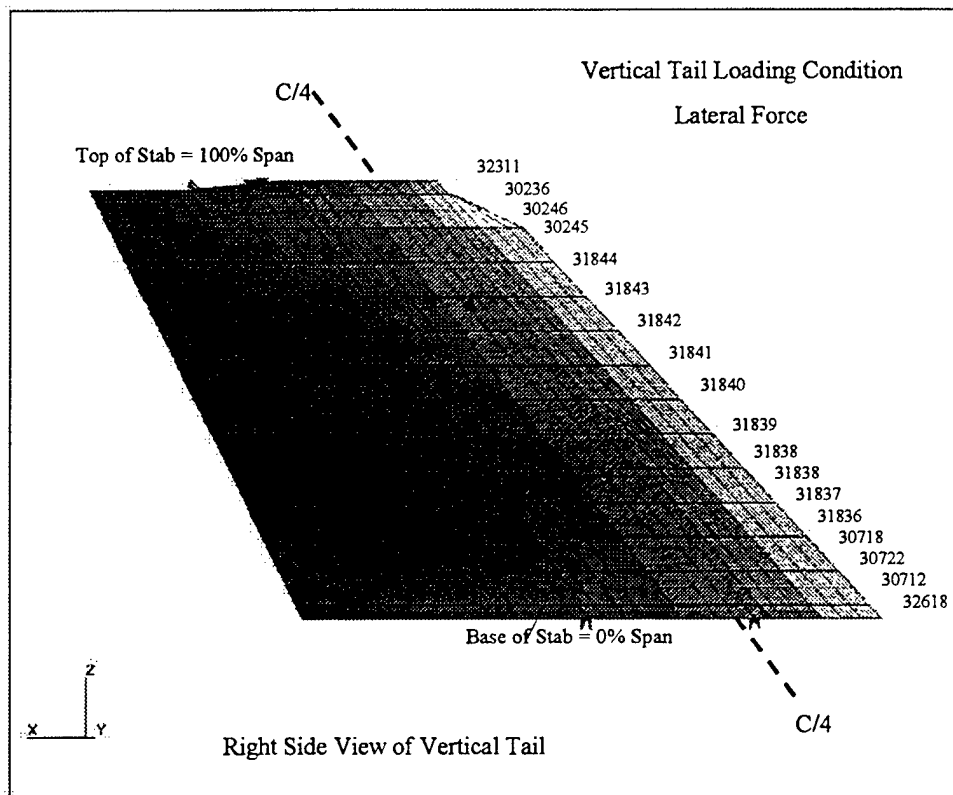


Figure 6.10: Vertical Tail Nodes and Loading Condition.

Figures 6.11 and 6.12 show the FRF between the vertical stabilizer and the pilot heels lateral and vertical. As with the horizontal, no significant response level was evident in the 20-25 Hz range. The span axis represents every node along the quarter chord, with the base of the tail defined as 0% span and the top representing 100%.

In Figure 6.11, the lateral FRF of greatest magnitude is at 6 Hz. This occurs at the top of the vertical tail. All FRFs decreased as the load was moved down the tail, except at 11.6 Hz. The FRF for this frequency reached a maximum at the base of the vertical tail.

Figure 6.12 shows the FRF between the applied load and vertical acceleration at the pilot heels. It is consistent with the information from the previous plot. Magnitudes at all but 11.6 Hz decrease as the load was moved down the tail. The amplitudes are substantially less than lateral.

Figures 6.13 and 6.14 display the FRF between the same points but at the discrete frequencies of 6 and 11.6 Hz. As with the horizontal stabilizer, the magnitude was normalized to the FRF of maximum amplitude, which occurred on the right tip of the horizontal stabilizer.

The top of the vertical has the same magnitude at 6 Hz as does the right tip of the horizontal. The base of the vertical tail has the dominant FRF at 11.6 Hz. Comparing this with the pressure transducer data, the right horizontal tail had the most energy concentrated in the 5-8 Hz bandwidth. This is where the 6 Hz FRF is a maximum. For the base of the vertical tail, the pressure energy was broadband from 11-19 Hz. The 11.6 Hz FRF is a maximum at this location.

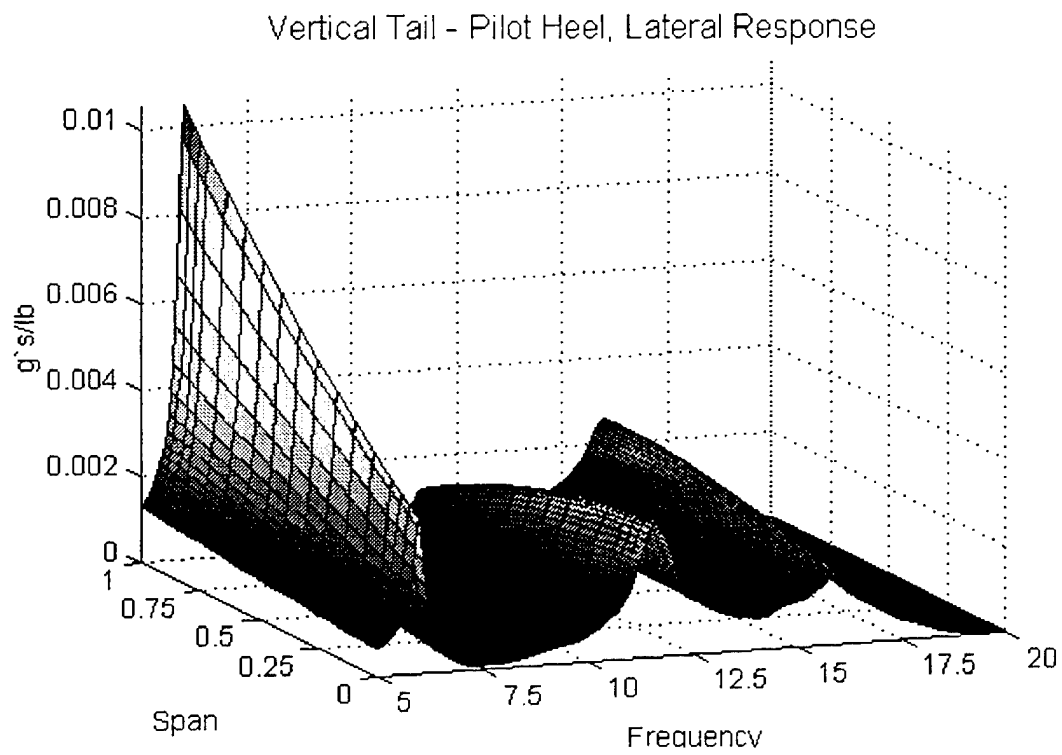


Figure 6.11: FRF Vertical Tail to Pilot Heel – Lateral Response.

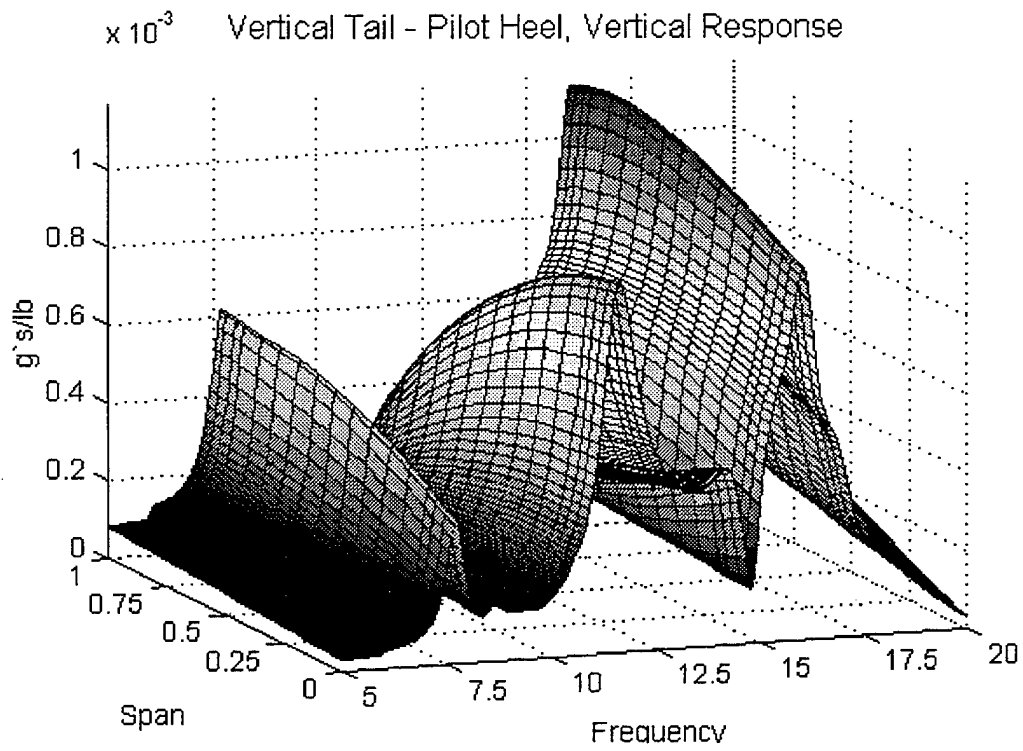


Figure 6.12: FRF Vertical Tail to Pilot Heel – Vertical Response.

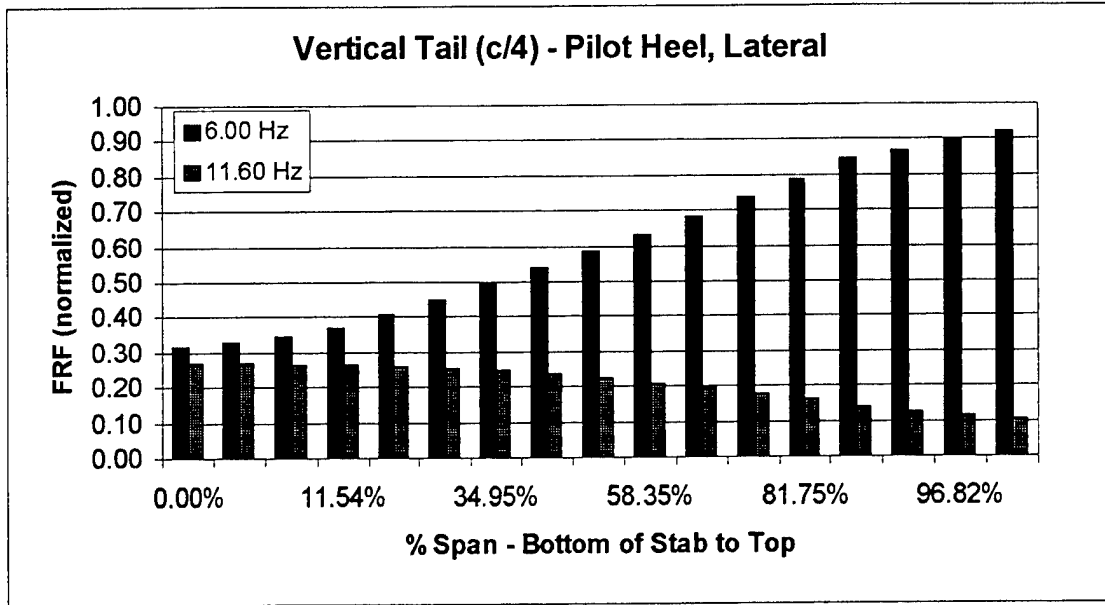


Figure 6.13: FRF Vertical Tail to Pilot Heel – Lateral.

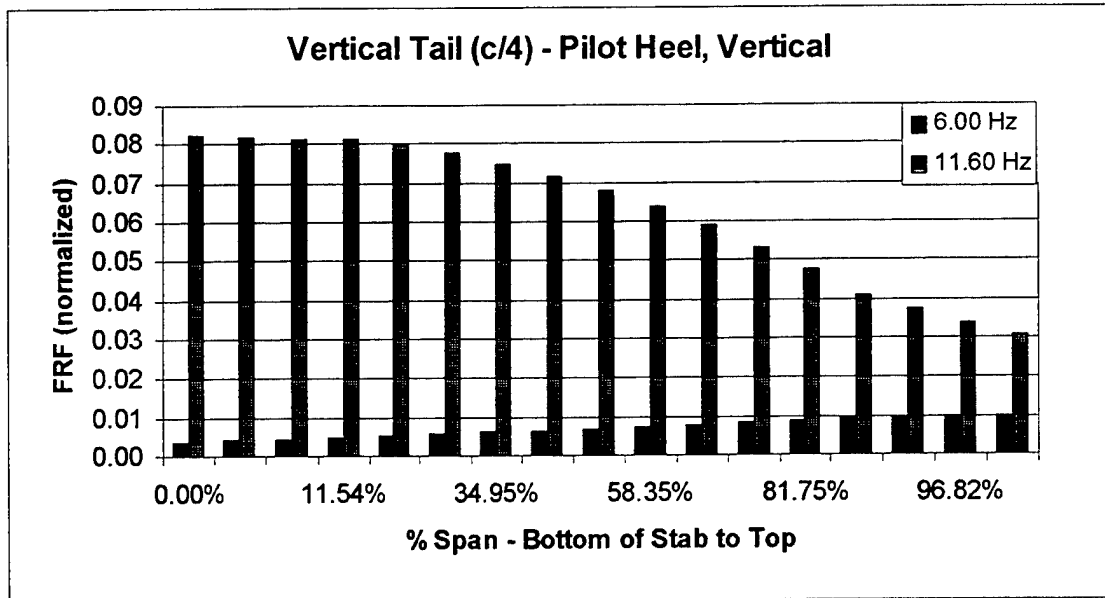


Figure 6.14: FRF Vertical Tail to Pilot Heel – Vertical.

VII. RESULTS AND ANALYSIS

A. SOLUTION METHOD

Having obtained the PSDs of the response and the structural frequency response functions, a solution can be obtained for the spectral content of the applied loads. The method for accomplishing this is provided by Bendat and Piersol [Ref. 8:p. 240]. A summary of this method follows.

\mathbf{X} is defined as a column vector representing the Fourier transform of q input records, and \mathbf{Y} the Fourier transform of k output records;

$$\mathbf{X} = \begin{bmatrix} X_1 \\ X_2 \\ \vdots \\ \vdots \\ X_q \end{bmatrix} \quad \mathbf{Y} = \begin{bmatrix} Y_1 \\ Y_2 \\ \vdots \\ \vdots \\ Y_k \end{bmatrix}$$

$\mathbf{X}^*, \mathbf{Y}^* =$ complex conjugate of the vectors \mathbf{X}, \mathbf{Y}

$\mathbf{X}', \mathbf{Y}' =$ transpose of the vectors \mathbf{X}, \mathbf{Y}

The input and output spectral density matrices can then be defined as

$$\mathbf{G}_x = \frac{2}{T} E\{\mathbf{X}^* \mathbf{X}'\} = \text{input spectral density matrix}$$

$$\mathbf{G}_y = \frac{2}{T} E\{\mathbf{Y}^* \mathbf{Y}'\} = \text{output spectral density matrix}$$

The notation used by Bendat and Piersol for G_{xx} and G_{yy} simply means that the PSDs and CSDs of each input and output record are contained with these matrices.

Another method for representing these terms, and useful for programming is

$$\mathbf{G}_{xx} = \begin{bmatrix} G_{11} & G_{12} & \cdots & G_{1q} \\ G_{21} & G_{22} & \cdots & G_{2q} \\ \vdots & & & \vdots \\ G_{q1} & G_{q2} & \cdots & G_{qq} \end{bmatrix}$$

$$\mathbf{G}_{yy} = \begin{bmatrix} G_{y_1y_1} & G_{y_1y_2} & \cdots & G_{y_1y_k} \\ G_{y_2y_1} & G_{y_2y_2} & \cdots & G_{y_2y_k} \\ \vdots & & & \vdots \\ G_{y_ky_1} & G_{y_ky_2} & \cdots & G_{y_ky_k} \end{bmatrix}$$

Both \mathbf{G}_{xx} and \mathbf{G}_{yy} are Hermitian matrices, with $G_{ij} = G_{ji}^*$ for all i and j . Each element in both matrices represents either the PSD or CSD for the inputs and responses. When the subscripts are the same, as with G_{11} , the value is a real number and represents the PSD for the load at point one. The other elements of the matrix are complex, such as G_{12} which is the CSD between the loads at point one and two. The same is true for the response matrix, with the diagonal being the PSDs for responses and the off diagonal terms are the CSDs between responses.

Finally, the FRF, \mathbf{H}_{xy} , where x defines the input and y is the output is given by

$$\mathbf{H}_{xy} = \begin{bmatrix} H_{1y_1} & H_{1y_2} & \cdots & H_{1y_k} \\ H_{2y_1} & H_{2y_2} & \cdots & H_{2y_k} \\ \vdots & \vdots & & \vdots \\ H_{\varphi_1} & H_{\varphi_2} & \cdots & H_{\varphi_k} \end{bmatrix}$$

Depending on the number of inputs and outputs used in the solution set, the FRF matrix may not be square. Using this definition of \mathbf{H}_{xy} , it follows that the output \mathbf{Y} is related to the input \mathbf{X} by the relationship

$$\mathbf{Y} = \mathbf{H}'_{xy} \mathbf{X} \text{ where } \mathbf{H}'_{xy} \text{ is the transpose matrix to } \mathbf{H}_{xy}$$

Having defined these terms, the following derivation is required to arrive at a solution for \mathbf{G}_{xx} .

$$\begin{aligned} \mathbf{Y} &= \mathbf{H}'_{xy} \mathbf{X} \\ \mathbf{Y}' &= (\mathbf{H}'_{xy} \mathbf{X})' = \mathbf{X}' \mathbf{H}_{xy} \\ \mathbf{Y}^* &= (\mathbf{H}'_{xy} \mathbf{X})^* = \mathbf{H}'_{xy} \mathbf{X}^* \\ \mathbf{Y}^* \mathbf{Y} &= (\mathbf{H}'_{xy} \mathbf{X}^*) (\mathbf{X}' \mathbf{H}_{xy}) \end{aligned}$$

Taking the expected value of both sides and multiplying by $(2/T)$ gives

$$\begin{aligned} \mathbf{G}_{yy} &= (\mathbf{H}'_{xy} \mathbf{X}^*) \mathbf{G}_{xx} (\mathbf{H}_{xy}) \\ \text{It follows that} \\ \mathbf{G}_{xx} &= (\mathbf{H}'_{xy} \mathbf{X}^*)^{-1} \mathbf{G}_{yy} (\mathbf{H}_{xy})^{-1} \end{aligned}$$

Assuming the required inverse matrices exist, a solution can be obtained for the spectral content of the applied loads. In the case of unequal inputs and responses, where \mathbf{H}_{xy} is not square, the solution, \mathbf{G}_{xx} , is found using gaussian elimination. Conditioning of the matrices becomes critical during the computations.

B. MATLAB® PROGRAM

Using this formulation, a MATLAB® code was written, contained in Appendix E, that solved for \mathbf{G}_{xx} . First, the user specified the frequency range of interest. This was limited from 5-25 Hz because of the range of frequency sweeps used to determine the frequency response functions. Then, NASTRAN grid points were selected for application of forces. Finally, response points to be used in the solution set were chosen.

The program looks up, on a frequency by frequency basis, the stored FRFs between force application points and response locations. This created the \mathbf{H}_{xy} matrix. The \mathbf{G}_{yy} matrix was found, again on a frequency by frequency basis, from the selected response points. PSDs and CSDs for each set of accelerometer flight test data was stored in .mat files. This allowed retrieval for use in the appropriate \mathbf{G}_{yy} matrix. Because the frequency interval on FRFs was .05 Hz and on the 1024 point FFT PSDs was .293 Hz, cubic spline interpolation was used to match the data sets.

The solution, \mathbf{G}_{xx} , represented the PSDs and CSDs of the applied loads at discrete frequencies. The frequency band was dependent on what the user had selected for the upper and lower limit. The interval between frequencies, or effective bandwidth was based on \mathbf{G}_{yy} . Hence for this output, with a 1024 point FFT, the interval was .293 Hz.

C. RESULTS

Numerous cases, with different locations of forces and responses, were computed. Some generalities included all forces placed along the quarter chord of either the horizontal or vertical tail. These points are shown in Figures 6.5 and 6.10 and listed in Table 7.1. Additionally, the only response data used was from a 100 knot record, entitled run 24. The response points contained in this data set are also displayed in Table 7.1. Horizontal tail span is defined from the right tip. Vertical tail span begins at the base of the tail.

Solution Parameters			
Response Data	Force Application Points		
Run 24: Accelerometers	Aircraft Location	% Span	NASTRAN Grid
Nose Cone Lateral	Horizontal Tail C/4	12.38	48008
Nose Cone Vertical		28.39	46008
Pilot Heel Lateral		45.84	45108
Pilot Floor Lateral		58.97	44008
Pilot Floor Vertical		70.70	43008
Pilot Overhead Lateral		86.70	42008
Copilot Overhead Lateral	Vertical Tail C/4	80.66	31844
Vertical Pylon Top Lateral		65.05	31842
Hor Stab Left Tip Long		49.45	31840
Hor Stab Right Tip Long		33.85	31838
Hor Stab Left Tip Vertical		18.25	31836
Hor Stab Right Tip Vertical		6.81	30722

Table 7.1: Response Data and Force Application Points.

The first solution set used two forces, one on the right horizontal stabilizer at mid semi-span and the other at mid-span of the vertical tail. Then, additional unknown forces were included, with different response data. For several frequency bands, the condition

number of the FRF matrix, \mathbf{H}_{xy} , became exceedingly high. This occurred when the FRFs were very small or FRFs from different points were of equal amplitude. In these cases, the precision of MATLAB[®] could not distinguish between numbers and interpreted the two rows of the matrix as duplicates of each other. Therefore, the inverse was not reliable.

Using between two and twelve forces, the response locations were varied to produced different solutions. Table 7.2 through 7.8 display the results for seven different loading conditions. In all these cases, every response location that run 24 contained was used. The tables present the RMS for each force within the frequency bands previously identified. In every case, the energy within these three bins represented over 80% of the total energy, throughout the 5-25 Hz range, of the force at that node. The final column indicates the RMS of the total force.

The RMS values were determined for each frequency band and then divided by the largest RMS value of total force. They represent the percentage of the total force that is located at that point on the aircraft and within the frequency range. Similarly, the RMS of total force was normalized to this same value. Hence, the RMS of total force that equals 1.0 represents the location on the tail that had the largest force throughout the 5-25 Hz band. Normalizing the forces was done to aid in comparison of loads between cases. Additionally, the conditioning of the matrices produced highly inaccurate results within certain frequency bands. In these cases, the solution had large amplitude PSDs in frequency ranges containing little response and small FRFs. The loads in nine and twelve force cases, Table 7.7 and 7.8, are highlighted to show the frequency content and magnitudes of the computed loads.

Forcing Function - Normalized (lb/lb)				
Node	Frequency Bin			RMS of Total Force
	5-8 hz	10-13 hz	22-25 hz	
48008	0.34	0.38	0.21	0.44
31840	0.47	1.00	0.52	1.00

Table 7.2: RMS of Two Force Solution Set.

Forcing Function - Normalized (lb/lb)				
Node	Frequency Bin			RMS of Total Force
	5-8 hz	10-13 hz	22-25 hz	
42008	0.36	0.42	0.11	0.60
46008	0.39	0.39	0.20	0.71
31840	0.46	0.71	0.30	1.00

Table 7.3: RMS of Three Force Solution Set.

Forcing Function - Normalized (lb/lb)				
Node	Frequency Bin			RMS of Total Force
	5-8 hz	10-13 hz	22-25 hz	
43008	0.14	0.06	0.12	0.22
46008	0.15	0.19	0.09	0.28
31844	0.51	0.49	0.36	0.88
31836	0.76	0.38	0.26	1.00

Table 7.4: RMS of Four Force Solution Set.

Forcing Function - Normalized (lb/lb)				
Node	Frequency Bins			RMS of Total Force
	5-8 hz	10-13 hz	22-25 hz	
43008	0.22	0.15	0.07	0.30
45108	0.53	0.28	0.06	0.63
46008	0.30	0.16	0.04	0.36
31844	0.50	0.16	0.10	0.60
31836	0.89	0.21	0.13	1.00

Table 7.5: RMS of Five Force Solution Set.

Forcing Function - Normalized (lb/lb)				
Node	Frequency Bins			RMS of Total Force
	5-8 hz	10-13 hz	22-25 hz	
42008	0.03	0.01	0.00	0.03
44008	0.07	0.02	0.01	0.07
46008	0.03	0.01	0.00	0.03
31844	0.48	0.11	0.05	0.47
31840	1.00	0.27	0.09	1.00
31836	0.53	0.17	0.05	0.54

Table 7.6: RMS of Six Force Solution Set.

Forcing Function - Normalized (lb/lb)				
Node	Frequency Bin			RMS of Total Force
	5-8 hz	10-13 hz	22-25 hz	
46008	0.00199	0.00564	0.00034	0.00613
45108	0.01034	0.00795	0.00135	0.01426
44008	0.01581	0.01946	0.00173	0.02596
43008	0.00661	0.01301	0.00036	0.01471
31844	0.19509	0.15047	0.00907	0.25202
31842	0.40794	0.32484	0.01723	0.53204
31838	0.58917	0.56503	0.01648	0.83418
31836	0.60257	0.75681	0.02316	1.00000
30722	0.23072	0.36292	0.01422	0.44914

Table 7.7: RMS of Nine Force Solution Set.

Forcing Function - Normalized (lb/lb)				
Node	Frequency bin			RMS of Total Force
	5-8 hz	10-13 hz	22-25 hz	
48008	0.00027	0.00777	0.00005	0.00818
46008	0.00053	0.02362	0.00015	0.02487
45108	0.00047	0.02538	0.00018	0.02738
44008	0.00148	0.01474	0.00021	0.01830
43008	0.00122	0.01450	0.00018	0.01670
42008	0.00028	0.00363	0.00004	0.00415
31844	0.03813	0.09873	0.00017	0.10854
31842	0.20775	0.47014	0.00037	0.53079
31840	0.43149	0.86229	0.00037	1.00000
31838	0.40227	0.72978	0.00030	0.86572
31836	0.17668	0.29943	0.00009	0.36249
30722	0.03467	0.07152	0.00010	0.08449

Table 7.8: RMS of Twelve Force Solution Set.

Figure 7.1 through 7.4 show the PSDs of loads for the twelve force solution set. The loads on the horizontal tail are within frequency bins which have little response. The magnitudes are much smaller than forces on the vertical and associated with poorly conditioned \mathbf{H}_{xy} matrices. Under the PSD plots is the phase angle between point 31840, where the force of largest magnitude is located, and selected points. They were determined from CSDs which capture the phasing information. Bendat and Piersol [Ref. 8:p. 125] provide a method of determining the phase angle from cross-spectral density functions. Although the plots are difficult to interpret, if viewed at just the modal frequencies earlier identified, 6.0 and 11.6 Hz, the phase relationship can be seen. This is available on the vertical tail where forces at these frequencies are located. The horizontal tail has no forces at these frequencies.

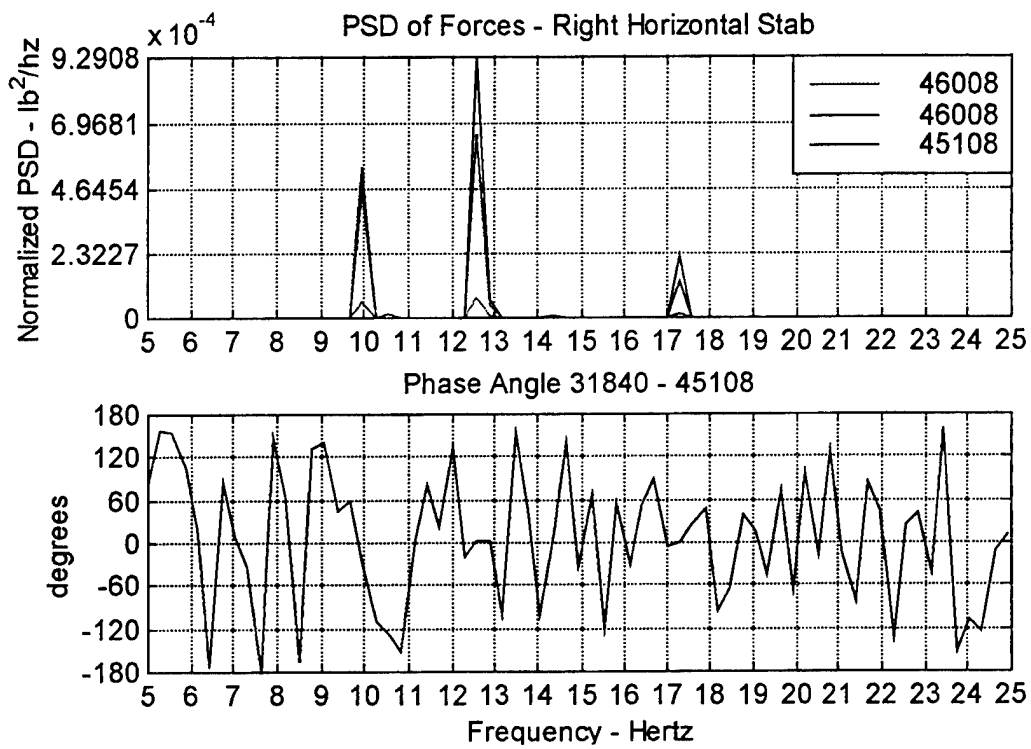


Figure 7.1: PSD of Forces on the Right Horizontal Tail.

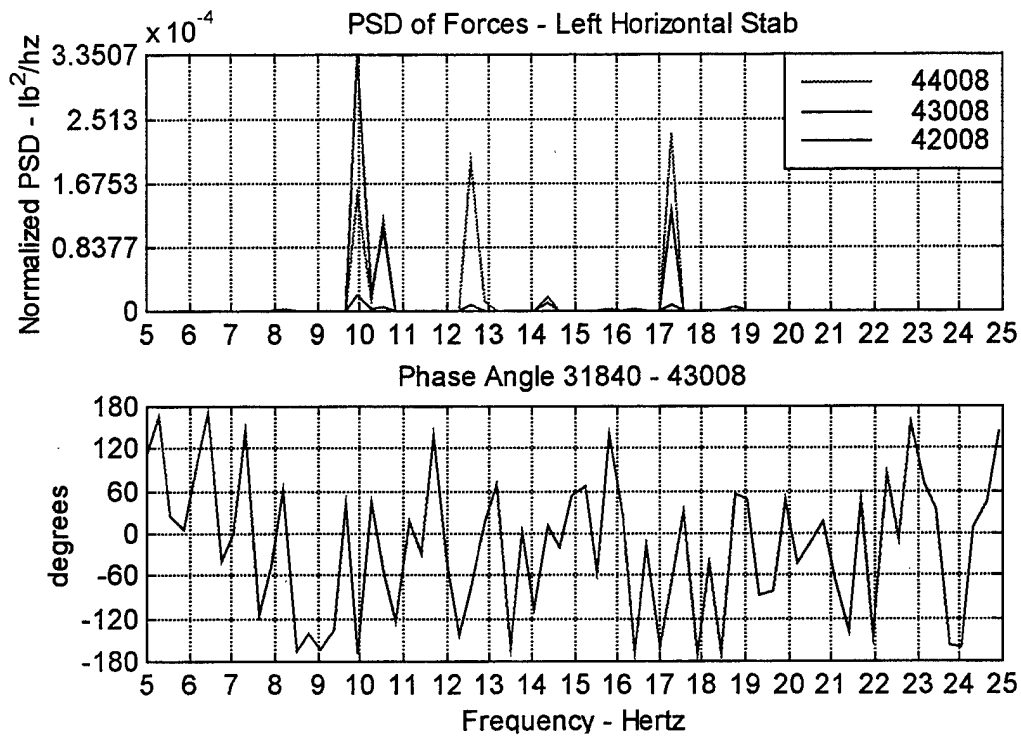


Figure 7.2: PSD of Forces on the Left Horizontal Tail.

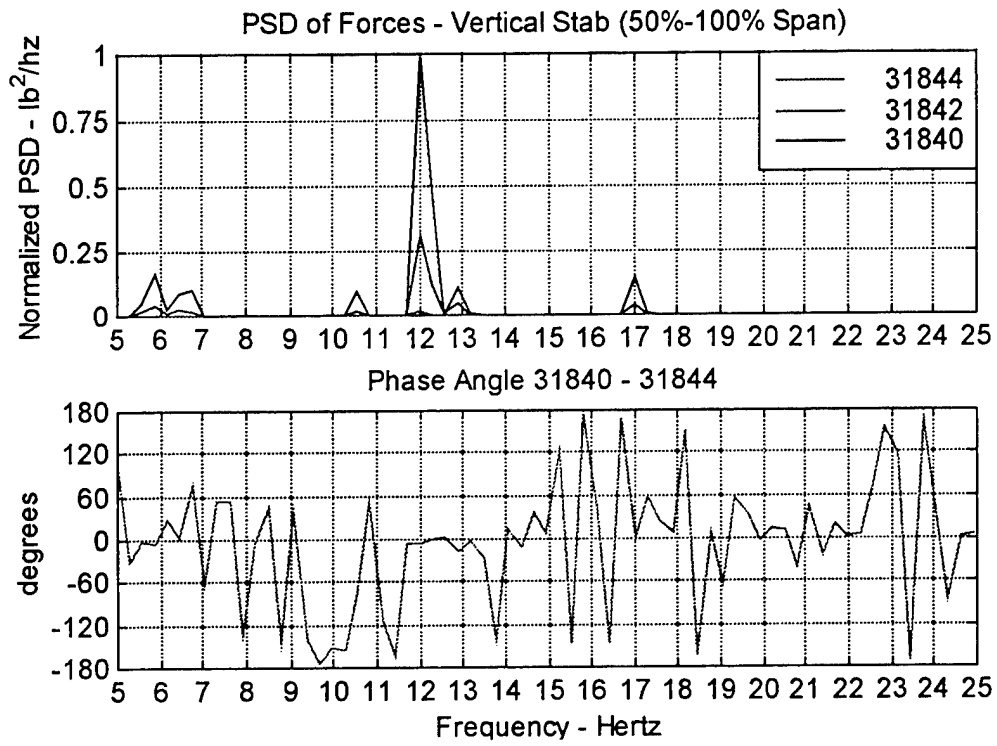


Figure 7.3: PSD of Forces on the Vertical Tail – 50% to 100% Span.

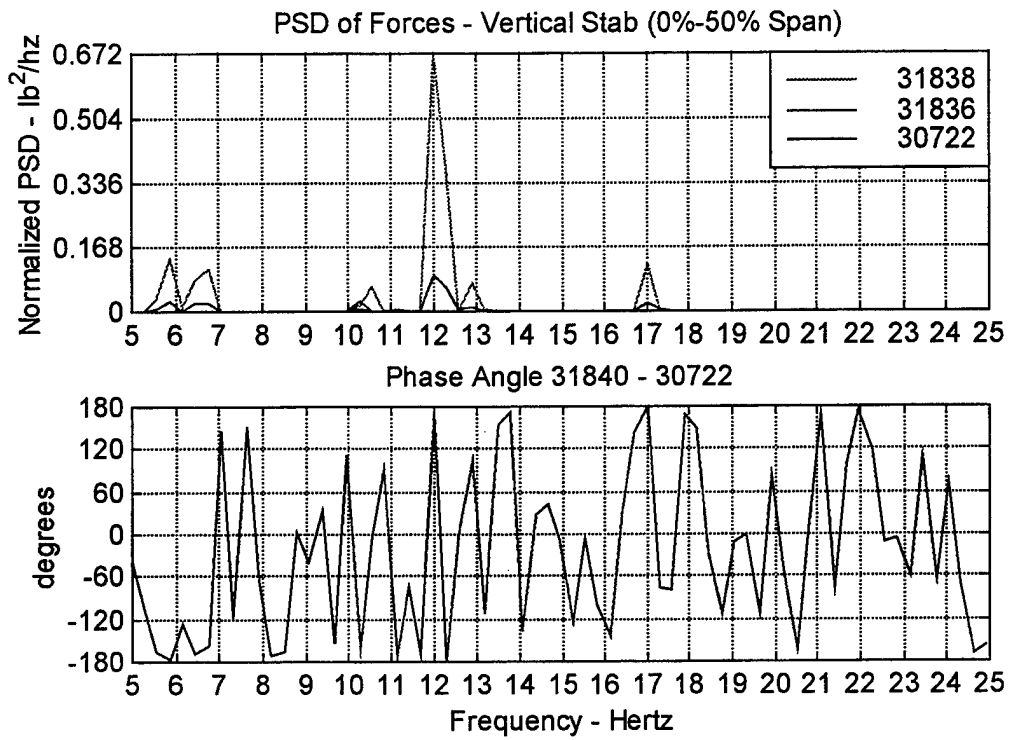


Figure 7.4: PSD of Forces on the Vertical Tail – 0% to 50% Span.

D. ANALYSIS

Beginning with the initial load set and continuing through twelve forces, the computations place the loads of largest magnitude on the vertical tail. Initially, the 10-13 Hz frequency bin had the greatest energy. As more and more forces were added, the magnitude of forces in the 5-8 Hz range grew tremendously. This coincided with a poorly conditioned FRF (\mathbf{H}_{xy}) matrix at 5 Hz. Even when eliminating the contribution to RMS from this frequency, forces from the base of the vertical tail to mid-span, at both 5-8 and 10-13 Hz, play the dominant role in producing the response.

In going from nine to twelve forces, the 10-13 Hz frequency bin, again, became the dominant source of energy. The problems with the conditioning of the FRF matrix, discussed above, were again present in the final solutions. The point where the largest forces were placed was grid 31840. Figures 7.5 and 7.6 display the distribution of forces along the horizontal and vertical tail. It can be seen that more energy was placed on the lower two-thirds of the vertical tail in both the 5-8 and 10-13 Hz frequency band. This is consistent with the results from the nine load case, shown in Table 7.7.

The results also match the information from the analysis of the frequency response functions and pressure transducers. The solution places loads on the fuselage at points that have high magnitude FRFs at 11.6 Hz. Pressure transducers confirm broadband excitation, including this frequency, and of largest amplitude at the base of the vertical tail.

Although the solution indicates a force on the vertical tail in the 5-8 Hz frequency bin, pressure transducers do not support this. The solution also has no forces in the 22-25 Hz range. The lack of NASTRAN modes in this bin has previously been discussed.

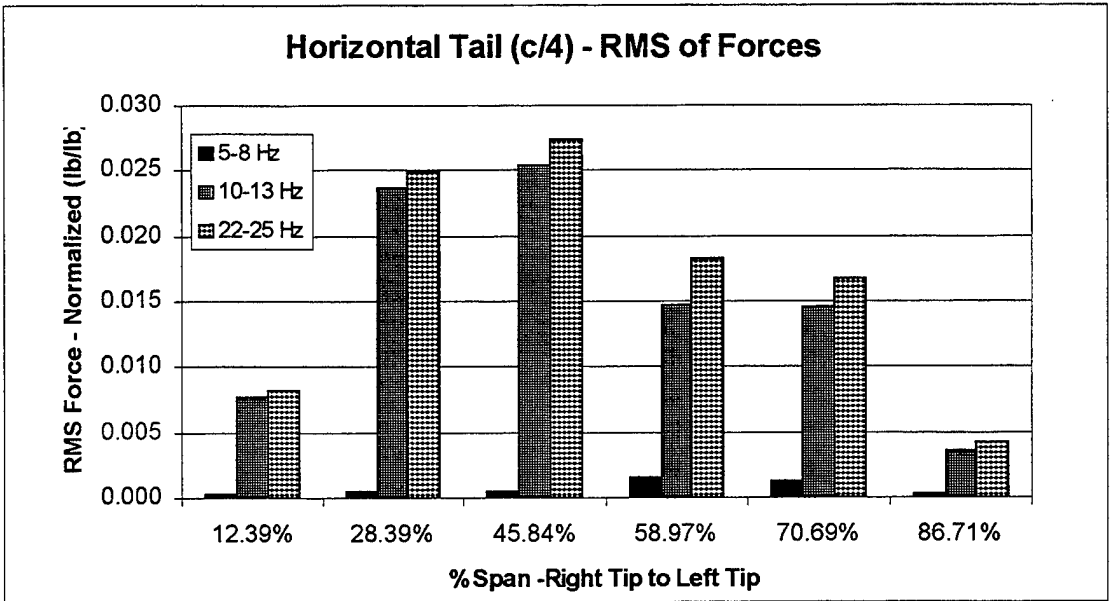


Figure 7.5: Distribution of Forces, 12 Force Solution Set – Horizontal Tail.

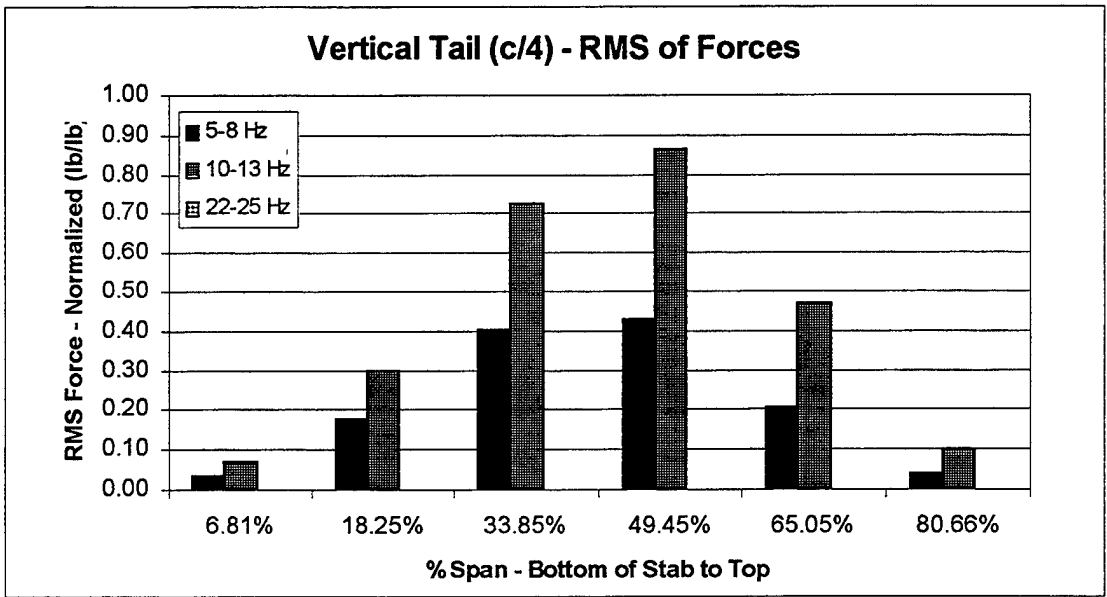


Figure 7.6: Distribution of Forces, 12 Force Solution Set – Vertical Tail.

VIII. CONCLUSIONS AND RECOMMENDATIONS

A. CONCLUSIONS

The goal of this work was to quantify the magnitude and location of aerodynamic loads contributing to the random excitation of the empennage. Then, follow-on efforts would have the proper focus and direction in modifying the structure. This was accomplished by first conducting an extensive analysis of flight test response data and pressure transducers. Due to the nature of the accelerometer time histories, spectral analysis was used. With this accomplished, the mode shapes and frequency response functions of the aircraft were determined. A NASTRAN model, modified to replicate the test flight aircraft, provided this information. Finally, a MATLAB[®] program was written to compute the spectral content of the aerodynamic loads producing the random excitation.

Each portion of the analysis provided insight into the nature of the response, locations of excitations, and the method in which the structure transfers input to output. From all of these elements, combined, conclusions were drawn.

The dominant response is lateral and occurs in three frequency bands or bins. The first bin is 5-8 Hz, then 10-13 Hz, and finally 22-25 Hz. Each accelerometer has its maximum value within one of these bins. The top of the vertical pylon has maximum response at 6.00 Hz. For the nose cone, pilot's station, and horizontal tail, 10-13 Hz excitation is the largest. Finally, the 22-25 Hz response is restricted primarily to the CPG station and vertical acceleration of the horizontal tail.

Within the first two bins, there are mode shapes that correspond with the motion seen in the output of the 22 accelerometers. The aft fuselage lateral torsion mode at 6.00 Hz and horizontal stabilizer yaw mode at 11.6 were identified not only through NASTRAN but also during actual frequency response hover testing. No mode was identified or significant frequency response function found within the 22-25 Hz bin. The horizontal stabilizer vertical bending mode at 26.02 Hz matches the response seen in the 22-25 Hz bin. The actual natural frequency of this mode was not identified during flight test; however, in previous NASTRAN models it is at 22.06 Hz.

From the forces computed through the MATLAB[®] program, good correlation existed with the previous analysis. Numerous loading combinations were applied with maximum loads continuously placed on the vertical stabilizer from the base to 50% span. The 10-13 Hz frequency bin contained the largest force. This agreed with data from differential pressure transducers which showed the highest broadband pressures at the base of the vertical tail.

From this, it can be concluded that forces within the 10-13 Hz bandwidth impinging on the lower two-thirds of the vertical tail play the most significant role in creating the random excitation. This is supported by the differential pressure transducers. Solutions want to place 5-8 Hz forces in this same area. This is not supported by pressure transducers and leads to the conclusion that main rotor 1P is the primary source of 6 Hz excitation. Because the 22-25 Hz excitation is so localized and no FRFs of magnitude are in this region, the least squares solution provides no contributing loads. If the horizontal stabilizer vertical bending mode is not at 26.02 Hz but lower, the broadband excitation

seen in the differential pressure transducers can excite this mode and produce the recorded response.

B. RECOMMENDATIONS

1. Correlate with Wind Tunnel Testing

Boeing and Sikorsky have conducted two wind tunnel tests. The purpose was to quantify the flow impinging on the tail and identify changes to the surface of the aircraft, such as strakes, that would modify the flow and reduce excitation levels. The results of this analysis should be compared to data from the wind tunnel. This could confirm the conclusions of this study about the nature of the aerodynamic loads and their primary locations on the fuselage.

2. Parameter Identification and Correlation with NASTRAN

During hover frequency response testing, actual natural frequencies were identified for three modes. As additional test flight hours become available, more parameter identification can occur. This will better identify the exact frequency of the horizontal stabilizer vertical bending mode, as well as clarify other modes. In addition, the change in natural frequencies due to adding stiffening brackets and tip weights to the horizontal stabilizer can be assessed. With this information, a detailed analysis of the NASTRAN model can be conducted with modification of natural frequencies and mode shapes to replicate the actual aircraft.

3. Additional Airspeed Analysis

The computed solution using the method of Bendat and Piersol was done for only 100 knot records. After receiving additional airspeed records from Sikorsky, the PSDs and CSDs were computed; however, no complete solutions were obtained for the spectral content of forces. Calculating solutions throughout the range of airspeeds can provide further confirm and clarity as to when the random excitation begins and if the 6 Hz response is due to main rotor 1P.

4. Structural Optimization

Ultimately, the goal is to eliminate or reduce the response to acceptable levels. Using the conclusions from this analysis and confirmation from the sources discussed above, the structure can be altered to reduce the frequency response functions within the excitation bandwidth. This can be accomplished using several different methods, or, optimally, a combination of all.

First, using the NASTRAN model, structural modifications can be done that move the natural frequency, 11.6 Hz, of the horizontal stabilizer yaw mode. The focus of the changes should occur on the lower two-thirds of the vertical tail. Extensive work was done by Tobin [Ref. 12] and Shoop [Ref. 13] to increase torsional stiffness of the aft tailcone. The work attempted to stiffen the tail and move the aft fuselage lateral torsional mode away from MR 1P. Their analysis and strain energy diagrams provide insight to methods of altering the structure, specifically for the 11.6 Hz mode.

Second, changes are proposed to the design of the tail fold, spars of the vertical tail, and the tail fan gear box struts. Additionally, a trade study is being conducted by the

Comanche Program Management Office (PMO – Comanche) on the mounting of the tail landing gear bay. As these designs are finalized, the dynamics of the tail will change. The quantification of the flow determined through this analysis should aid in creating a dynamically “tuned” design.

Finally, modifying the flow around the main rotor hub and pylon has been investigated through the wind tunnel experiments previously discussed. Modifications to the structure must be done in conjunction with changes to the flow. Only through this integrated approach can an acceptable solution be obtained. In this manner, both the flow and structural response can be optimized for maximum reduction of the airframe vibratory response.

APPENDIX A: TEST FLIGHT PARAMETERS

Mnemonic	Parameter	Affected Components	Units
HBNORML1	Horz Stabilizer Flatwise Bending, LHS (near Root)	Horizontal Stabilizer	in-lb
HBNORMR1	Horz Stabilizer Flatwise Bending, RHS (near Root)	Horizontal Stabilizer	in-lb
HBNORML2	Horz Stabilizer Flatwise Bending, LHS (outboard)	Horizontal Stabilizer	N/A
HBNORMR2	Horz Stabilizer Flatwise Bending, RHS (outboard)	Horizontal Stabilizer	N/A
HSTBFWDB	Horz Stab Fwd Folding Joint Bending LHS	Horizontal Stabilizer	in-lb
HSVAFTL	Horz Stab Aft LHS Spar Shear Force – lb	Horizontal Stabilizer	N/A
HSVAFTR	Horz Stab Aft RHS Spar Shear Force – lb	Horizontal Stabilizer	N/A
HSVFWDL	Horz Stab Forward LHS Spar Shear Force – lb	Horizontal Stabilizer	N/A
HSVFWDR	Horz Stab Forward RHS Spar Shear Force – lb	Horizontal Stabilizer	N/A
VSFFTS1	Vert Stab Attach Fwd Ftg Outer Cap LHS	Vert / Shroud	u“/”
VSFFTS2	Vert Stab Attach Fwd Ftg Outer Cap RHS	Vert / Shroud	u“/”
VSAFTS1	Vert Stab Attach Aft Ftg Outer Cap LHS	Vert / Shroud	u“/”
VSAFTS2	Vert Stab Attach Aft Ftg Outer Cap RHS	Vert / Shroud	u“/”

Table A.1: Test Flight Parameters.

Mnemonic	Parameter	Affected Components	Units
BVSRTMX	Vertical Stab Root Roll Moment	Vert / Shroud	N/A
DHSDRAG	Horizontal Stab Drag – DP	Horizontal Stab	N/A
DHSTABMX	Net Stab Roll Moment –DP	Horizontal Stab	in-lb
DHYAWMZ	Horizontal to Vertical Stab Yaw Moment – DP	Horizontal Stab	in-lb
DHSTABVZ	Net Stabilizer Lift (lb) – DP	Horizontal Stab	N/A
DVSAFTLH	Derived Vert Load Aft LHS Lug - DP	Vert / Shroud	lb
DVSAFTRH	Derived Vert Load Aft RHS Lug - DP	Vert / Shroud	lb
DVSFWDLH	Derived Vert Load FWD LHS Lug - DP	Vert / Shroud	lb
DVSFWDRH	Derived Vert Load FWD RHS Lug - DP	Vert / Shroud	lb
DVSRTMX	Vertical Stab Root Roll MMT – DP	Vertical Stab Attachment	N/A
DVSRTMY	Vertical Stab Root Pitch MMT - DP	Vertical Stab Attachment	N/A
DVSTABVY	Derived Vertical Stab Lateral Force – DP	Vert / Shroud	N/A
HBEDGEL1	Horz Stab Edgewise Bending, LHS (near root)	Horizontal Stab	N/A
HBEDGER1	Horz Stab Edgewise Bending, RHS (near root)	Horizontal Stab	N/A

Table A.2: Test Flight Parameters.

APPENDIX B: PSD AND CSD PROGRAMS

```
% psd_flt_data.m

% Program reads the input flight data for a run and the computes the
% PSD for each accelerometer time history

% The input record is an 18,000 X n matrix with each column
% representing another transducer

% Input the data set you want to read, sampling rate, data set you
% want plotted

clear

run_labels_file

dt = 1/300;
string = ['run140'];
speed = ['140 Knots'];
eval(['load ',string,','.m']);
i = 0;

for col = 4:32
i = i + 1;
n = 1024;
noverlap = round(.67*n);
eval(['x = ',string,'_data(:,col);']);

% Using the SPEC command
% [Pxx,F] = spec(x,n,noverlap,hanning(n),1/dt);

% Using the PSD command
[Pxx,F] = psd(x,n,1/dt,hanning(n),noverlap);

% Normalize by multiplying by 2/frequency sampling rate
% To get the rms multiply by sampling rate/nfft then add
% This is from Parseval's theorem

Pxx = (2/(1/dt)) * Pxx;

% Another way to normalize so that the rms is just amplitudes add
% together
% With this method, the value from different length fft's is the same
%Pxx = (2/(1/dt)) * (300/n) * Pxx;
```

```

% Plotting Function

plot_max = round(25/((1/dt)/n));
ymax = max(Pxx(10:plot_max,1));
figure(i)
plot(F,Pxx(:,1));
grid;
axis([0 25 0 ymax]);
set(gca,'xtick',[0:1:25]);
eval(['title(''PSD ',deblank(run_labels(col,:)),' ', num2str(n),' Point
FFT''')']);
xlabel('Frequency - Hz');
ylabel('g`s^2/Hz');
eval(['text(5,.9*ymax,'Run ',speed,...
        ', Hanning Window, 67% Overlap'')']);

% Save the PSD data in another matrix for use in solving for forcing
functions

% Name of the matrix saved is psd_run24 (mat format) and has the
frequency and

% the psd for all accelerometer data we had for run24.

eval(['psd_',string,'(:,i) = Pxx(:,1);']);
end

%save frequency as a separate variable
psd_labels = run_labels(4:size(run_labels,1),:);

eval(['save psd_',string,' psd_',string,' F psd_labels']);

```

```

%   csd_flt_data.m
%   Program reads the input flight data for a run and the computes the
%   CSD (cross spectral density) between output accelerometer time
%   history

%   The input record is an 18,000 X n matrix with each column
%   representing another transducer

%   Input the data set you want to read, sampling rate, data set you
%   want plotted

dt = 1/300;
load run24
k = 0;

for col = 5:5
for i = 1:12
k = k + 1;
ii = i + 3;
n = 1024;
noverlap = round(.67*n);
x = run24_data(:,col);
y = run24_data(:,ii);

% Using the CSD command
[Pxy,F] = csd(x,y,n,1/dt,hanning(n),noverlap);

% Normalize by multiplying by 2/frequency sampling rate
% To get the rms multiply by sampling rate/nfft then add
% This is from Parseval's theorem

Pxy = (2/(1/dt)) * Pxy;

% Another way to normalize so that the rms is just amplitudes added
% together
% With this method, the value from different length fft's is the same

%Pxy = (2/(1/dt))* (300/n) * Pxy;

% Plotting Function
plot_min = round(5/((1/dt)/n));
plot_max = round(25/((1/dt)/n));
ymax = max(abs(Pxy(plot_min:plot_max,1)));
figure(k)
subplot(2,1,1);
plot(F,abs(Pxy(:,1)));
grid;
axis([5 25 0 ymax]);
set(gca,'xtick',[5:1:25]);
eval(['title(''CSD ',deblank(run24_labels(col,:)),' - ',
deblank(run24_labels(ii,:)),' ''')']);
xlabel('Frequency - Hz');
ylabel('g`s^2/Hz (Amplitude)');

```

```

subplot(2,1,2)
plot(F,180/pi * angle(Pxy(:,1)));
angle_max = max(180/pi * angle(Pxy(plot_min:plot_max,1)));
axis([5 25 -180 180]);
set(gca,'xtick',[5:1:25]);
set(gca,'ytick',[-180:60:180]);
grid;
xlabel('Frequency - Hz');
ylabel('Phase Angle - degrees')
eval(['title('Run ',num2str(run24_data(1,1)),...
      ', Hanning Window, 67% Overlap, ',num2str(n),' Point FFT')']);
%eval(['text(5,.89*angle_max,'Phase Angle
      ',num2str(run24_data(1,1)),...
      ', Hanning Window, 67% Overlap, ',num2str(n),' Point FFT')']);

% Save the CSD data in another matrix for use in solving for forcing
% functions
% Name of the matrix saved is psd_run24 (mat format) and has the
% frequency and the psd for all accelerometer data we had for run24.

eval(['csd_run24_',num2str(col-3),':,i) = Pxy(:,1);']);

end

%eval(['save psd_run24 csd_run24_',num2str(col-3),' F -append;']);

end

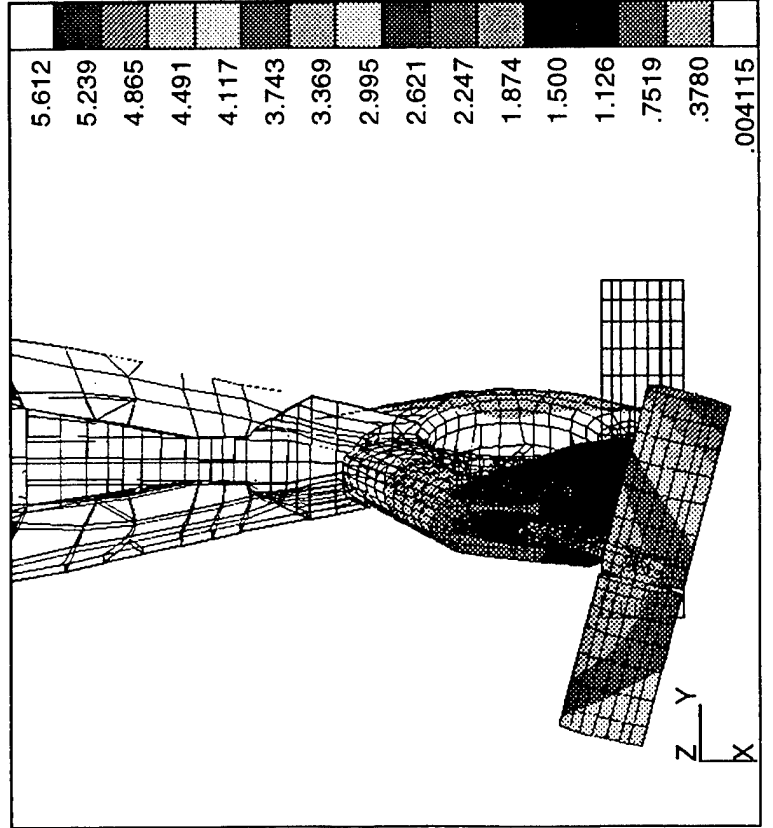
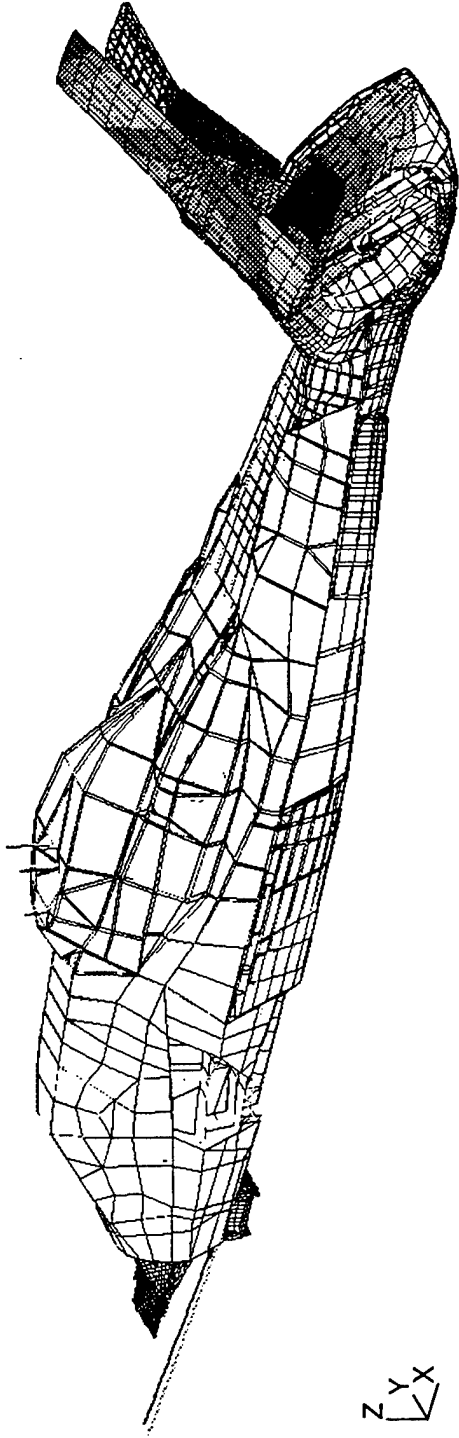
```

APPENDIX C: MODE SHAPES

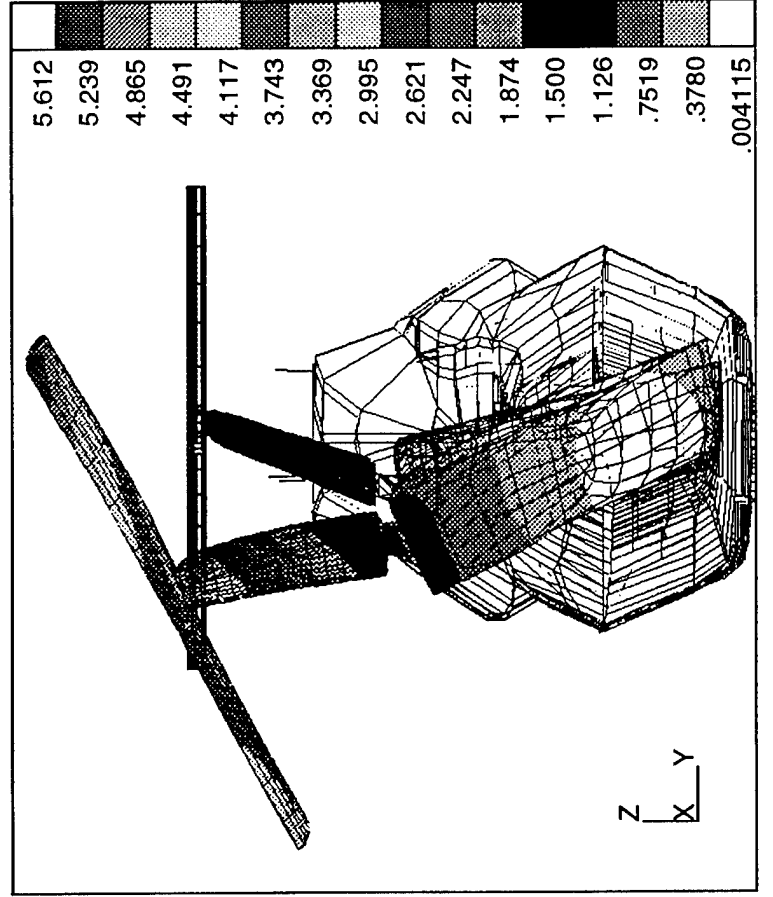
Mode shapes for selected modes are presented on the next eleven pages.

Aft Fuselage Lateral Torsional Mode, 6.00 Hertz

5.612
5.239
4.865
4.491
4.117
3.743
3.369
2.995
2.621
2.247
1.874
1.500
1.126
.7519
.3780
.004115

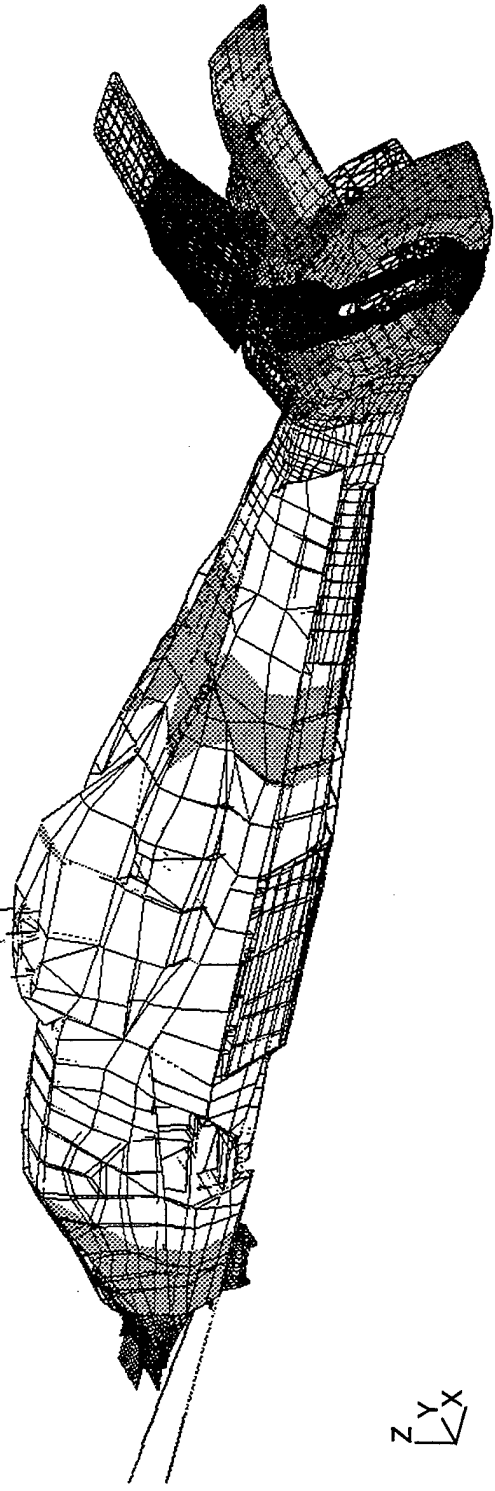


5.612
5.239
4.865
4.491
4.117
3.743
3.369
2.995
2.621
2.247
1.874
1.500
1.126
.7519
.3780
.004115

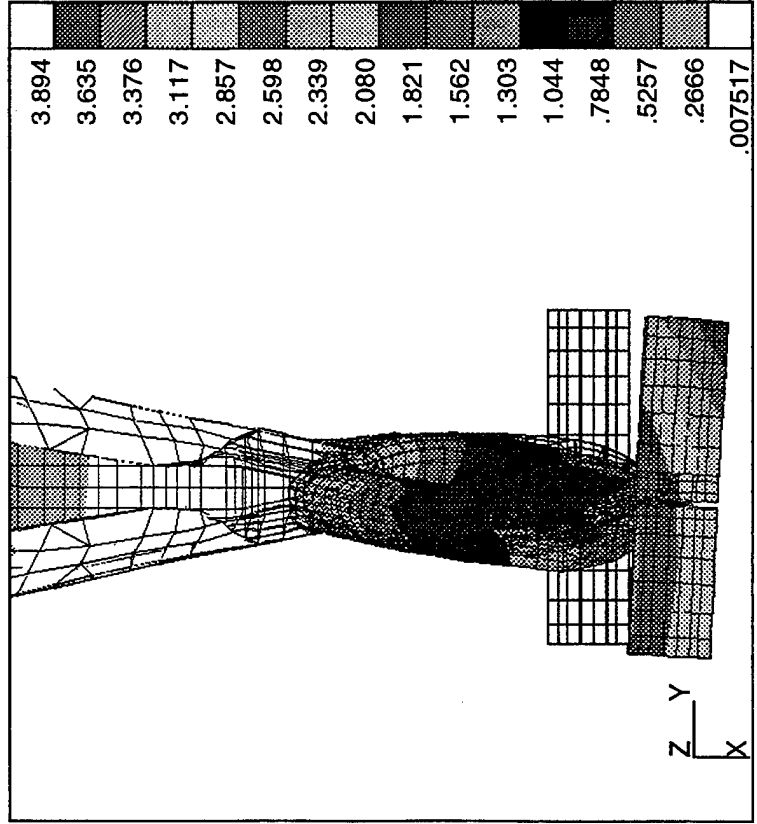


5.612
5.239
4.865
4.491
4.117
3.743
3.369
2.995
2.621
2.247
1.874
1.500
1.126
.7519
.3780
.004115

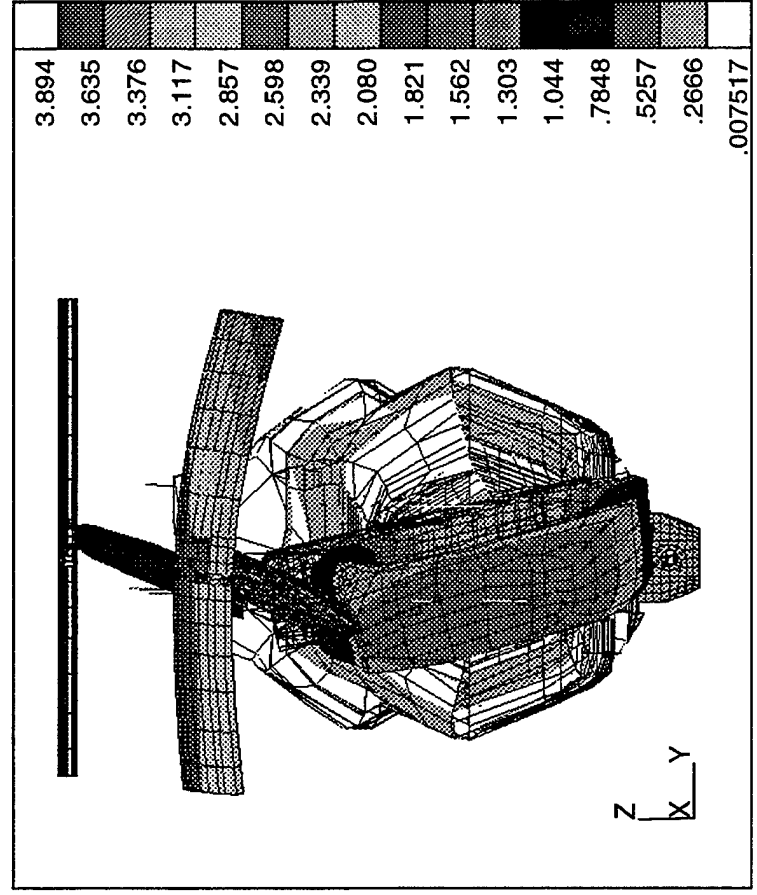
Fuselage First Vertical Bending Mode, 7.70 Hertz



3.894
3.635
3.376
3.117
2.857
2.598
2.339
2.080
1.821
1.562
1.303
1.044
.7848
.5257
.2666
.007517

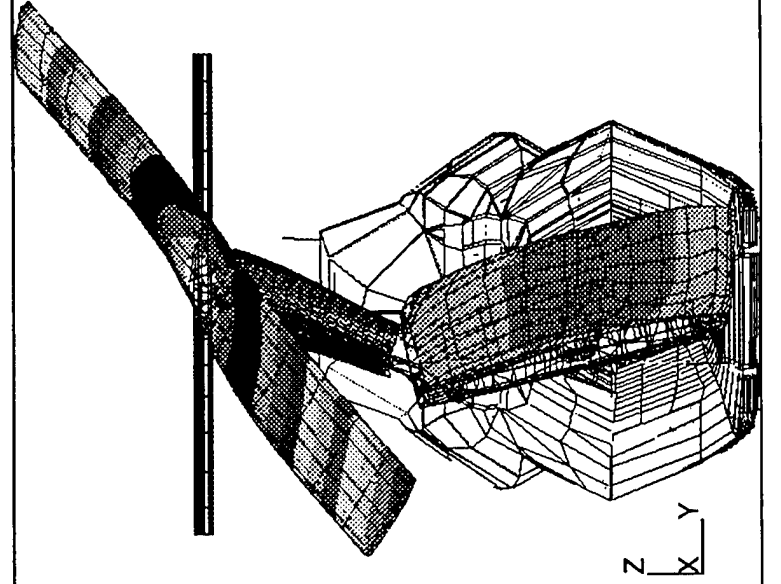
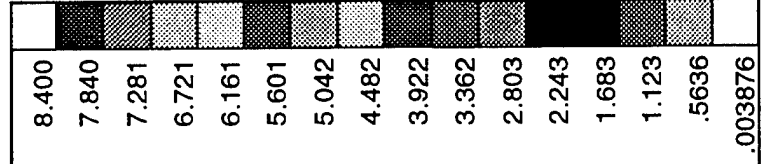
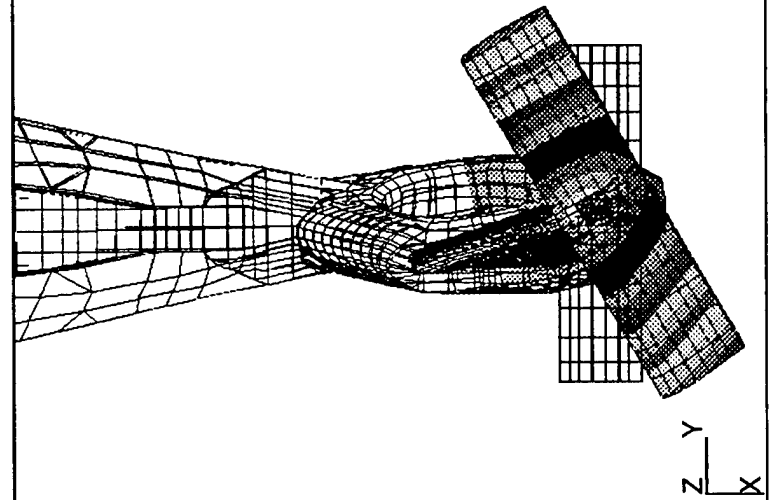
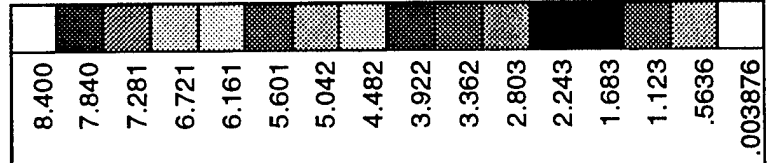
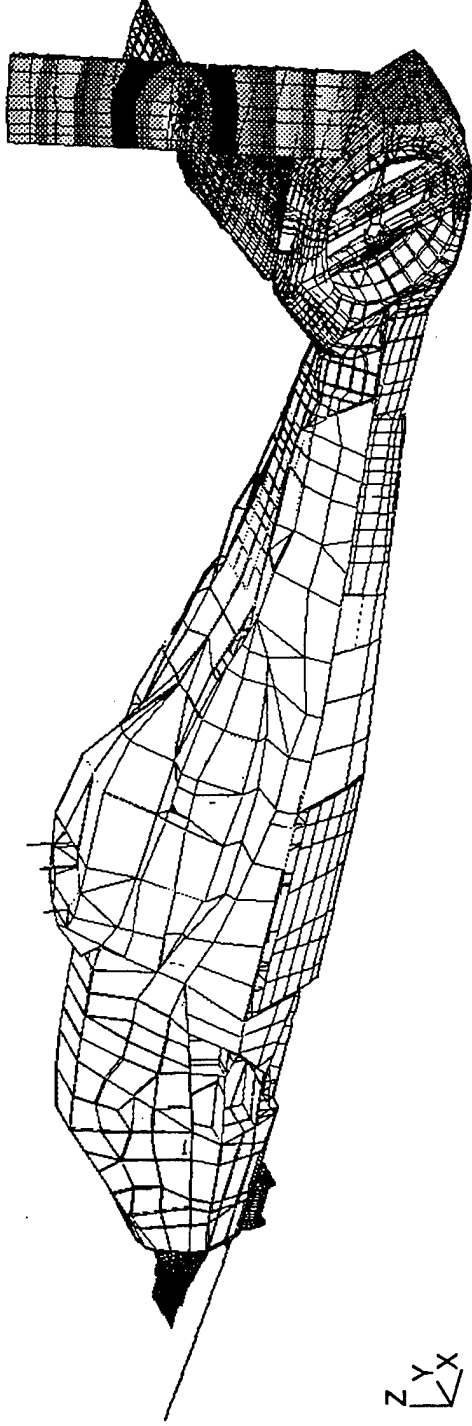
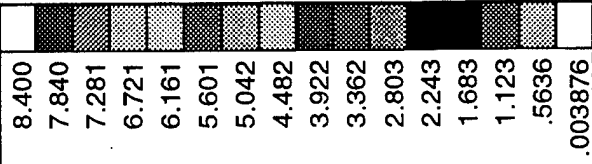


3.894
3.635
3.376
3.117
2.857
2.598
2.339
2.080
1.821
1.562
1.303
1.044
.7848
.5257
.2666
.007517

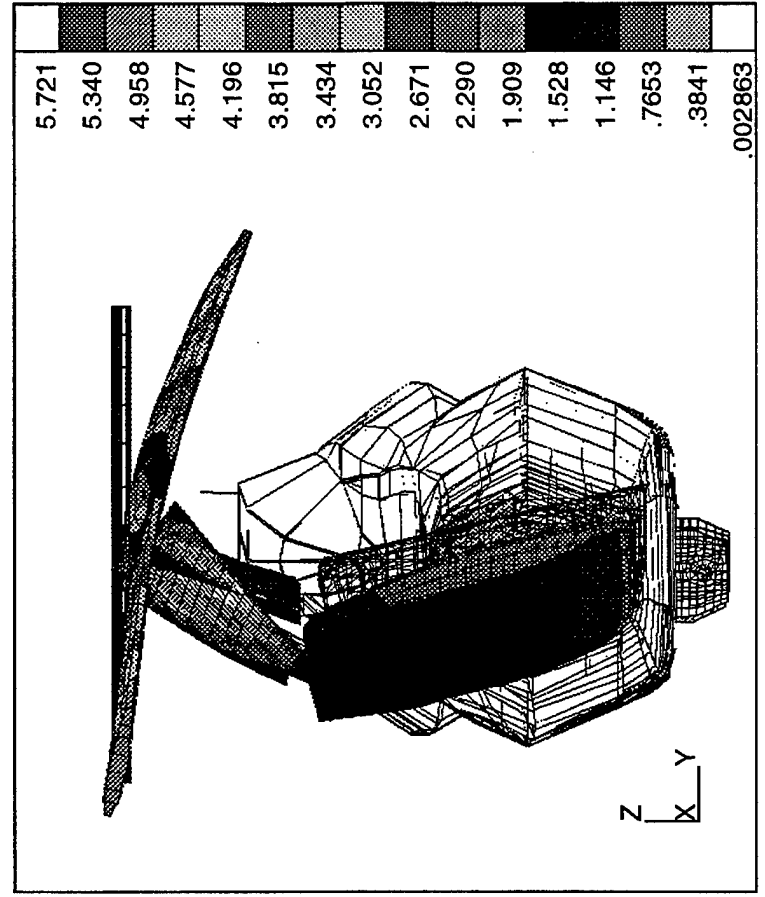
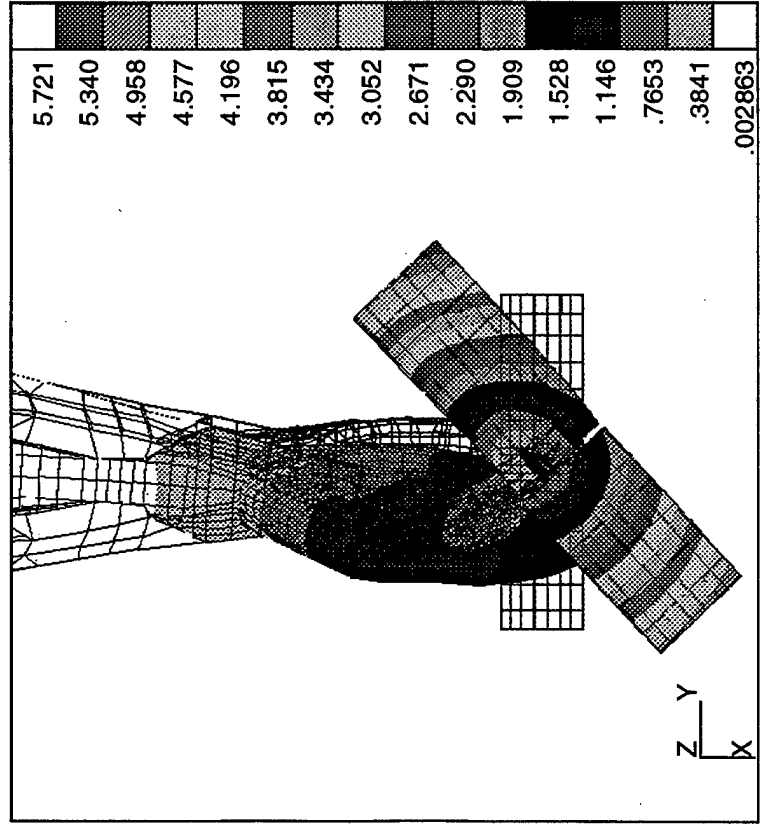
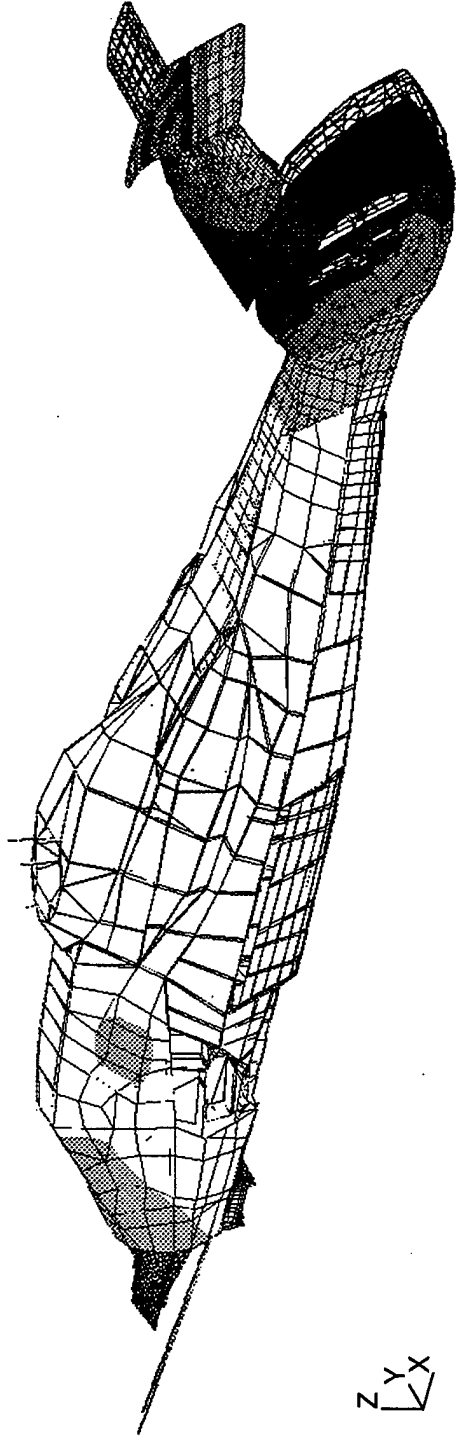


3.894
3.635
3.376
3.117
2.857
2.598
2.339
2.080
1.821
1.562
1.303
1.044
.7848
.5257
.2666
.007517

Horizontal Stab Roll Mode, 9.50 Hertz

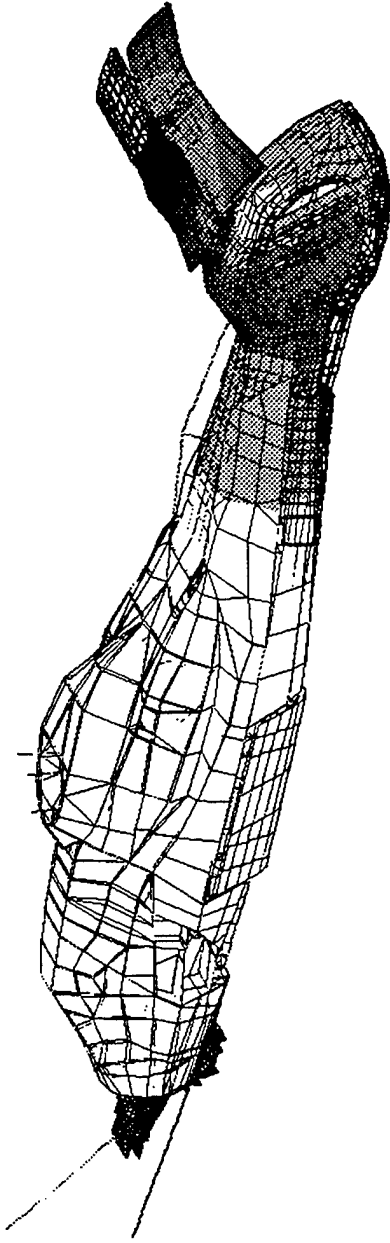


Horizontal Stab Yaw Mode, 11.60 Hertz

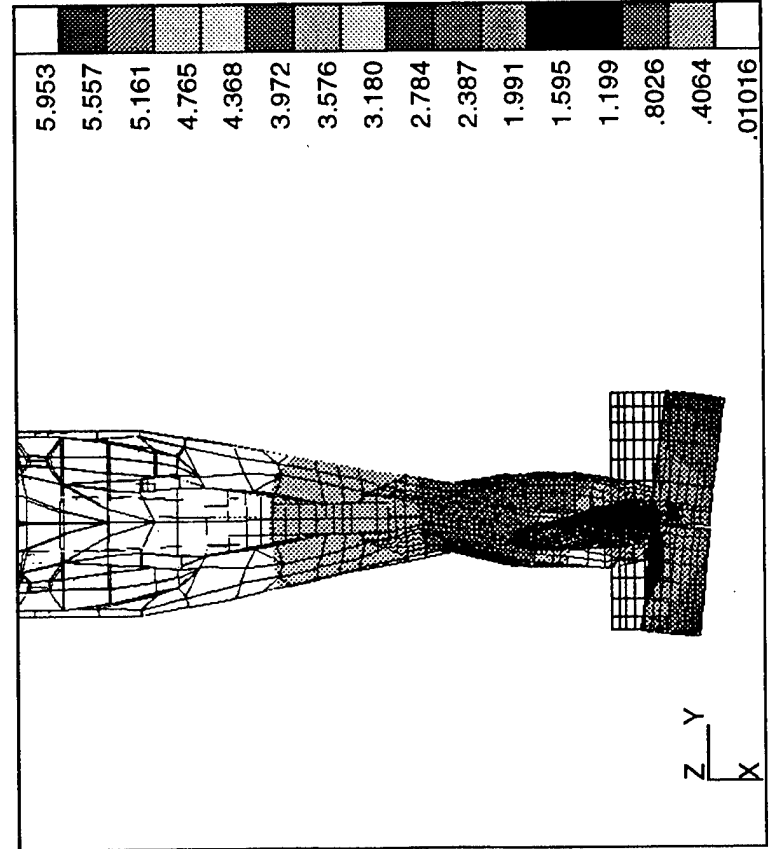


2nd Fuselage Vertical Bending Mode, 14.52 Hertz

5.953
5.557
5.161
4.765
4.368
3.972
3.576
3.180
2.784
2.387
1.991
1.595
1.199
.8026
.4064
.01016

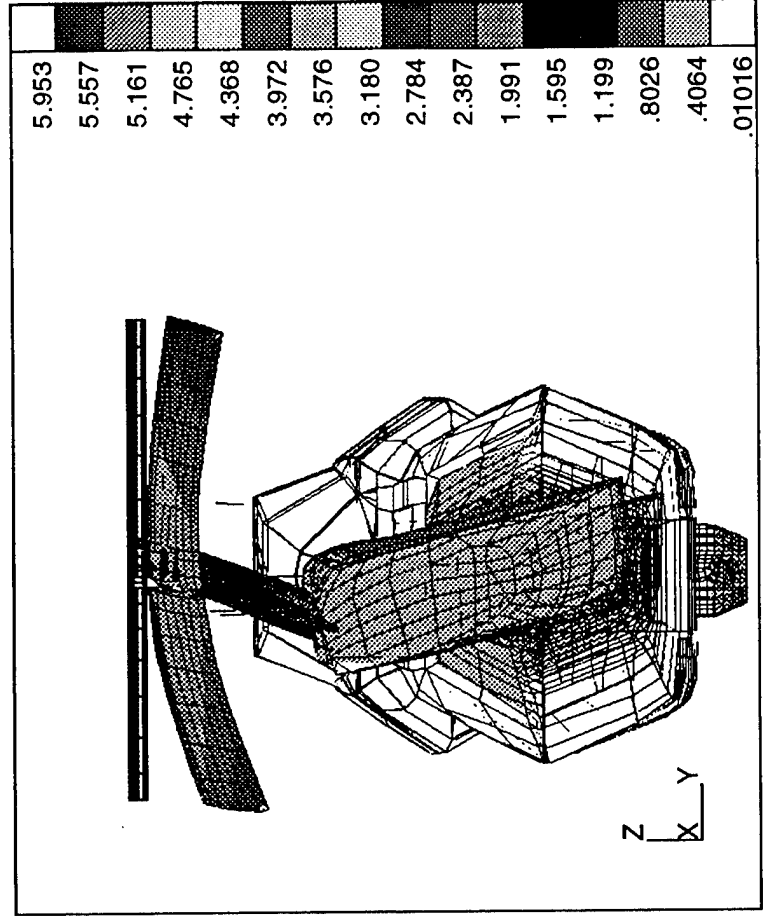


Z
Y
X



5.953
5.557
5.161
4.765
4.368
3.972
3.576
3.180
2.784
2.387
1.991
1.595
1.199
.8026
.4064
.01016

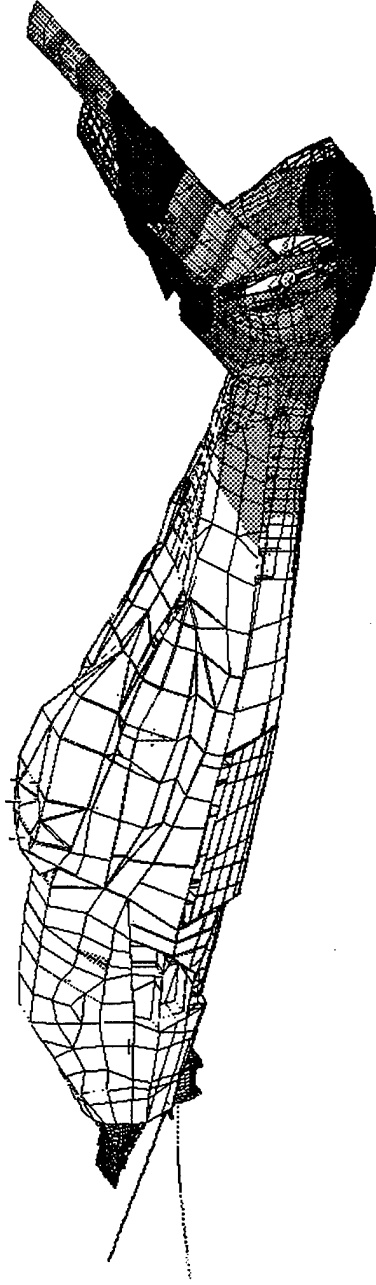
Z
Y
X



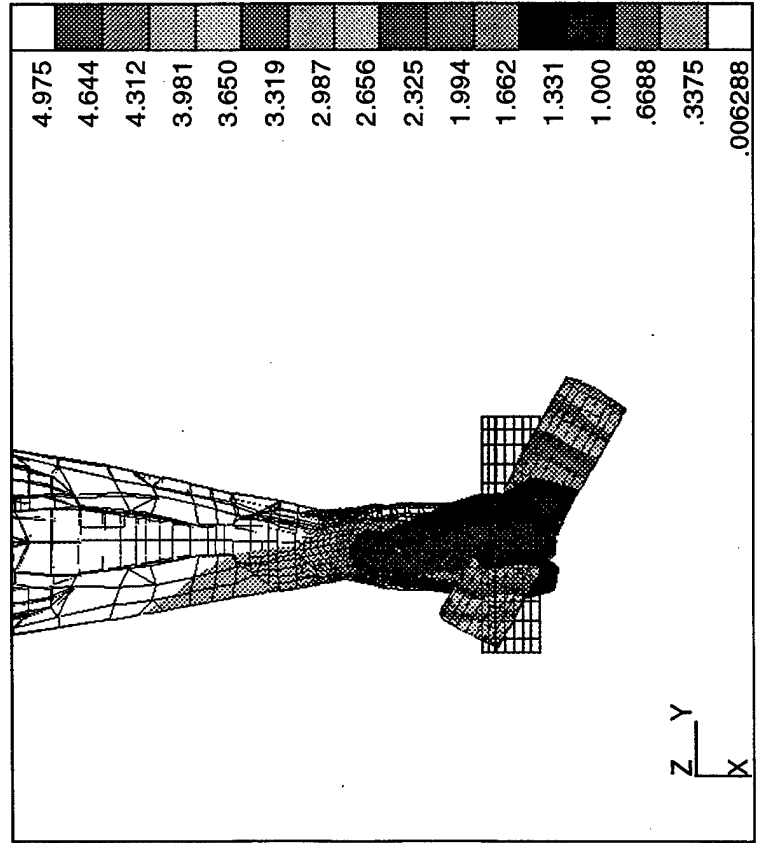
5.953
5.557
5.161
4.765
4.368
3.972
3.576
3.180
2.784
2.387
1.991
1.595
1.199
.8026
.4064
.01016

Z
Y
X

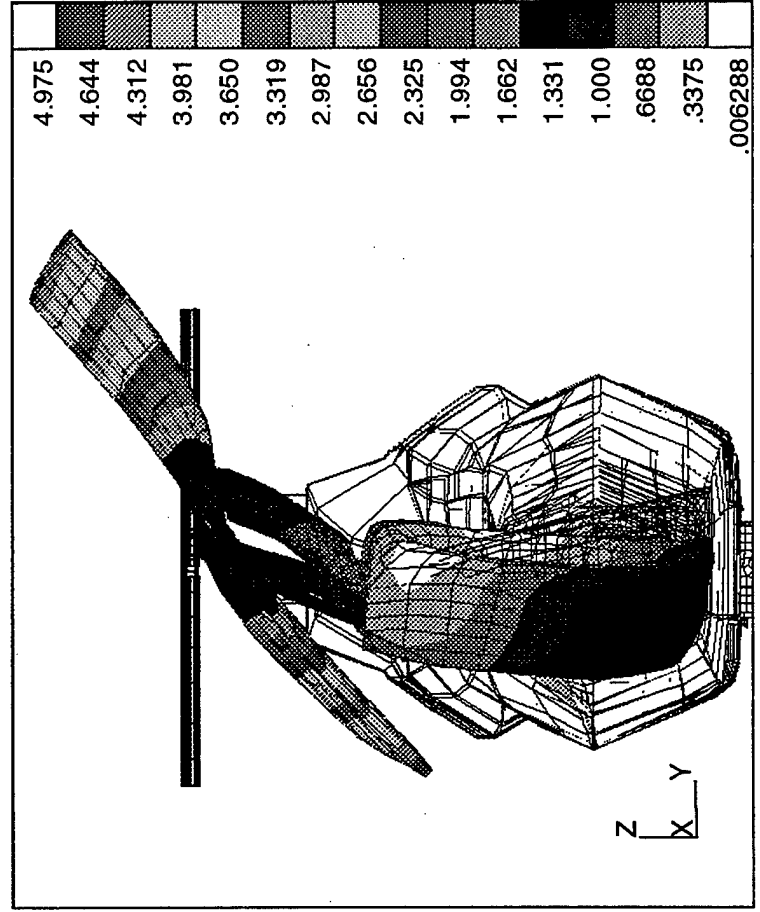
2nd Fuselage Lateral Mode, 16.07 Hertz



Z
Y
X

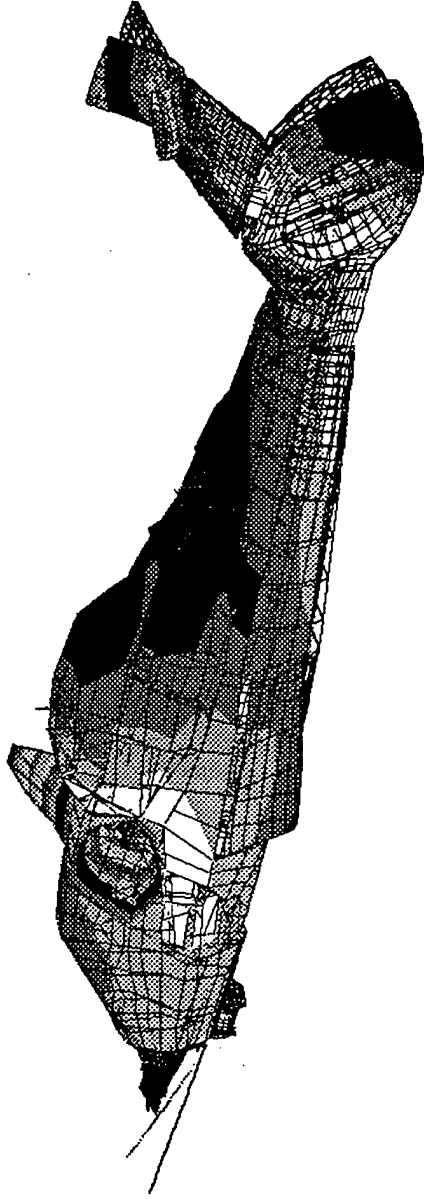


Z
Y
X



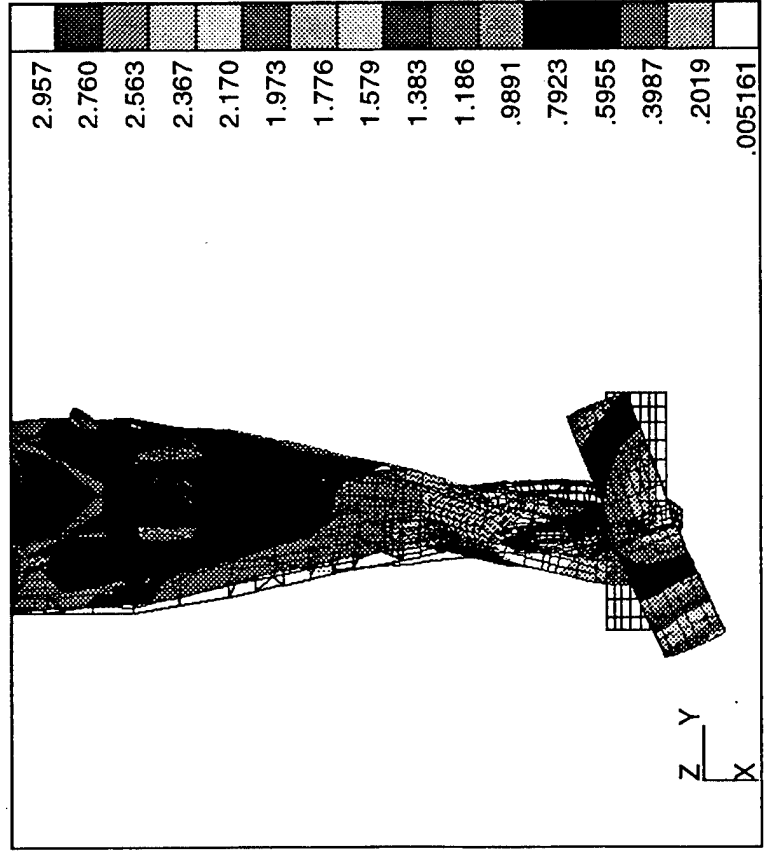
Z
Y
X

Fuselage Mode, 20.45 Hertz



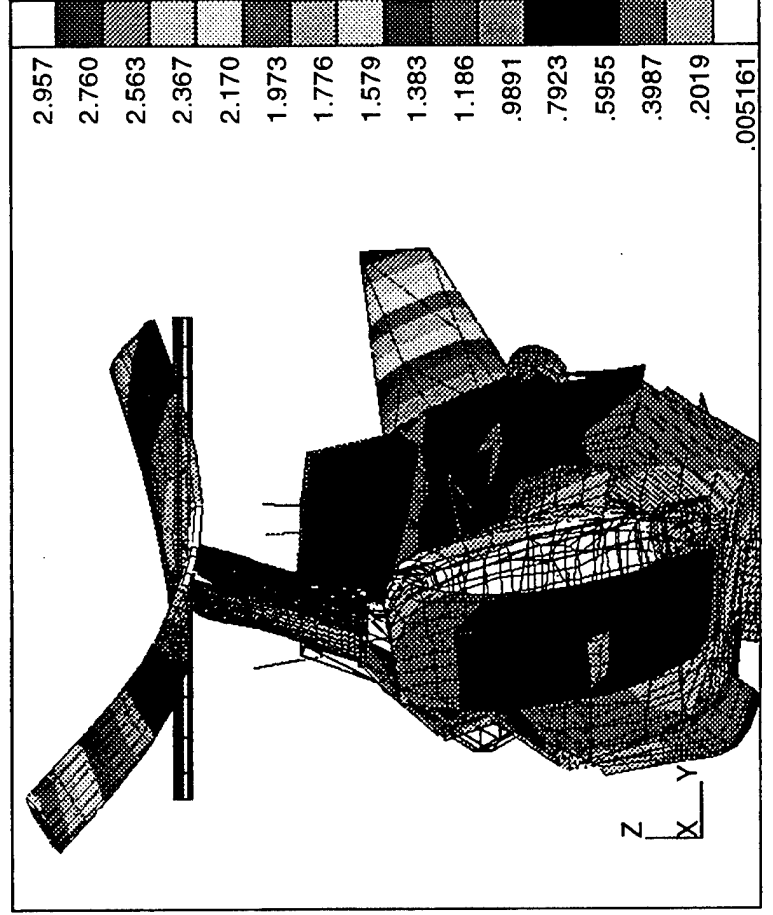
2.957
2.760
2.563
2.367
2.170
1.973
1.776
1.579
1.383
1.186
.9891
.7923
.5955
.3987
.2019
.005161

Z
Y
X



2.957
2.760
2.563
2.367
2.170
1.973
1.776
1.579
1.383
1.186
.9891
.7923
.5955
.3987
.2019
.005161

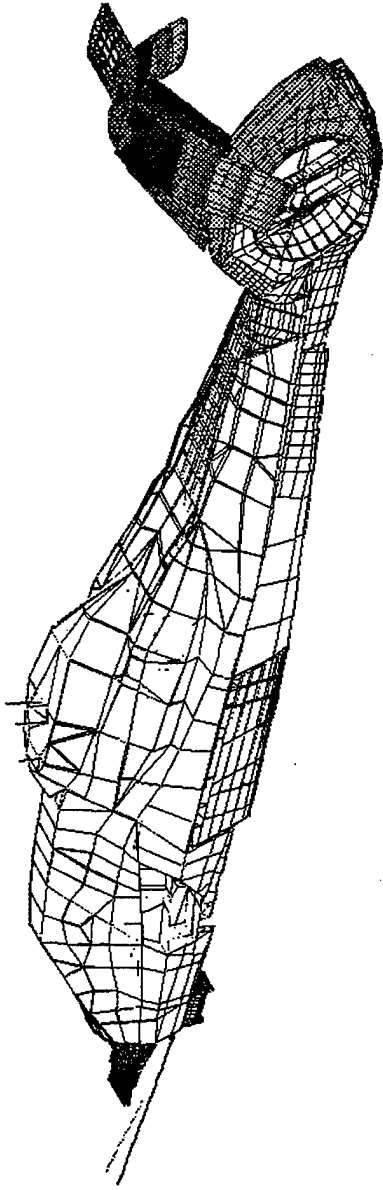
Z
Y
X



2.957
2.760
2.563
2.367
2.170
1.973
1.776
1.579
1.383
1.186
.9891
.7923
.5955
.3987
.2019
.005161

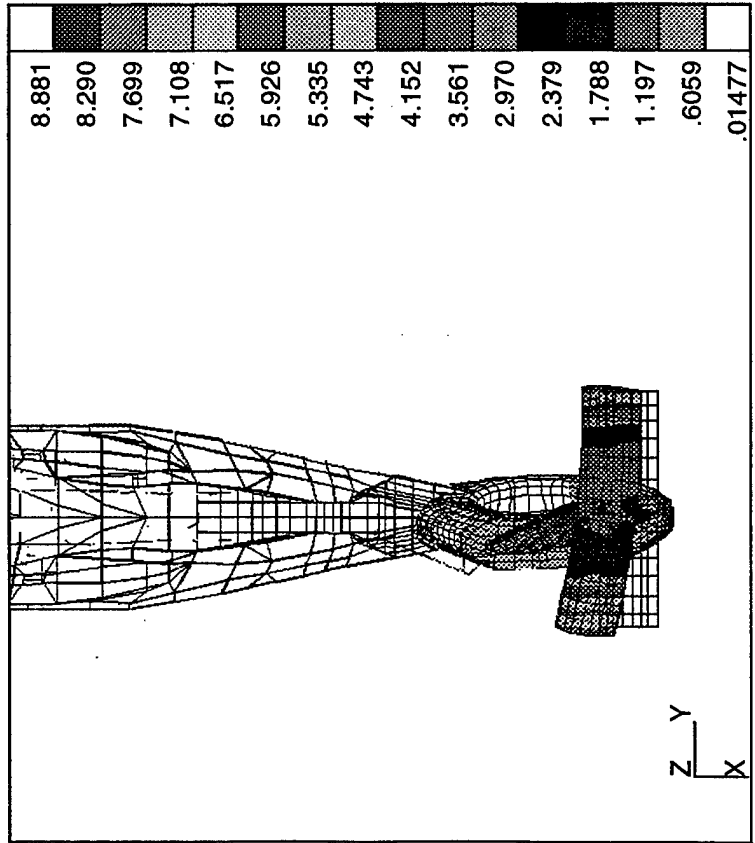
Z
Y
X

Stab Vertical Bending Mode, 21.56 Hertz



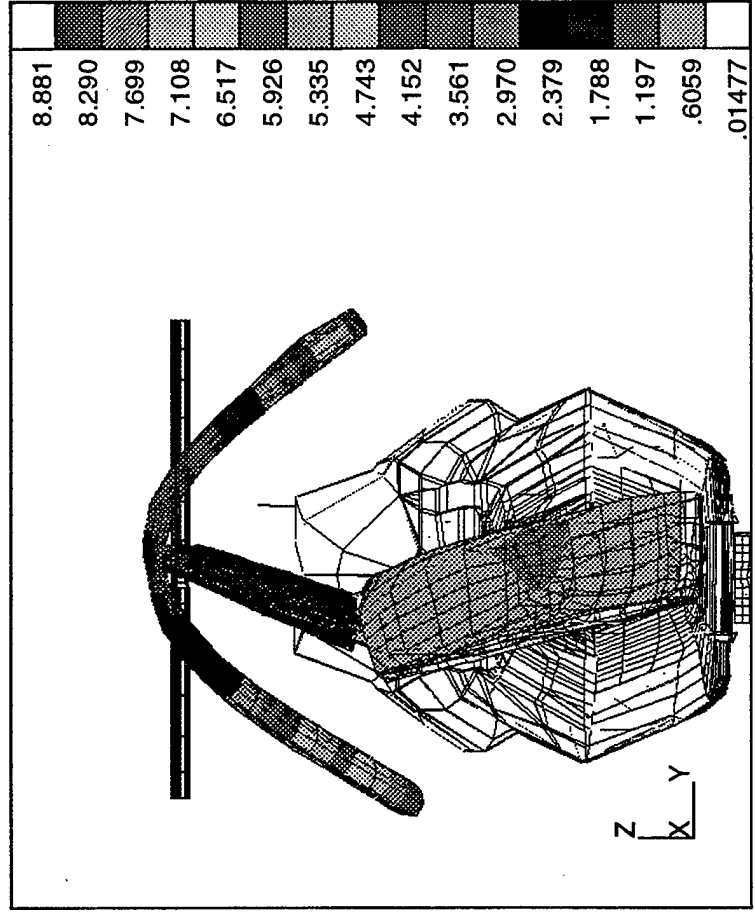
Z
Y
X

8.881
8.290
7.699
7.108
6.517
5.926
5.335
4.743
4.152
3.561
2.970
2.379
1.788
1.197
.6059
.01477



Z
Y
X

8.881
8.290
7.699
7.108
6.517
5.926
5.335
4.743
4.152
3.561
2.970
2.379
1.788
1.197
.6059
.01477

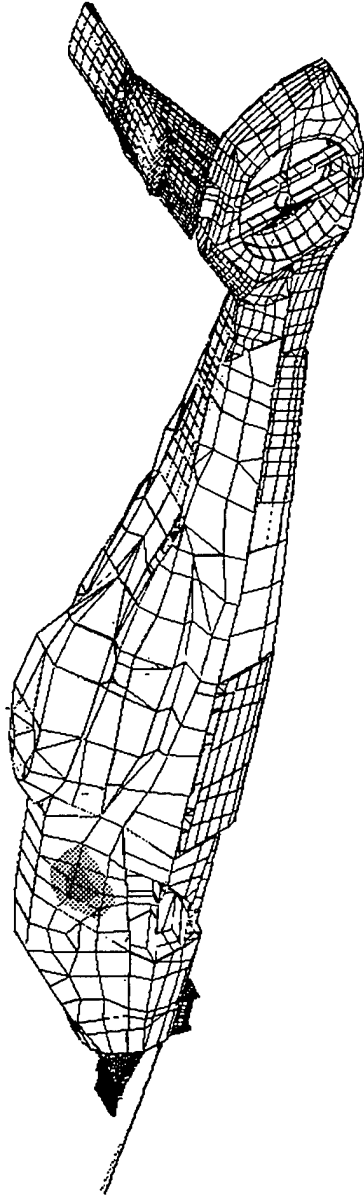


Z
Y
X

8.881
8.290
7.699
7.108
6.517
5.926
5.335
4.743
4.152
3.561
2.970
2.379
1.788
1.197
.6059
.01477

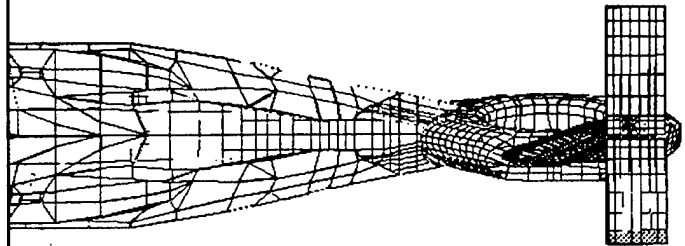
Copilot Sidearm Mode, 23.05

5.894
5.501
5.109
4.716
4.323
3.930
3.538
3.145
2.752
2.359
1.967
1.574
1.181
.7885
.3958
.003028



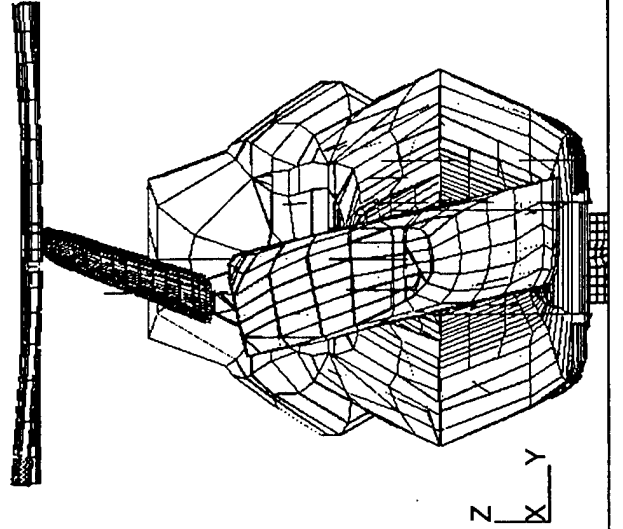
Z
Y
X

5.894
5.501
5.109
4.716
4.323
3.930
3.538
3.145
2.752
2.359
1.967
1.574
1.181
.7885
.3958
.003028



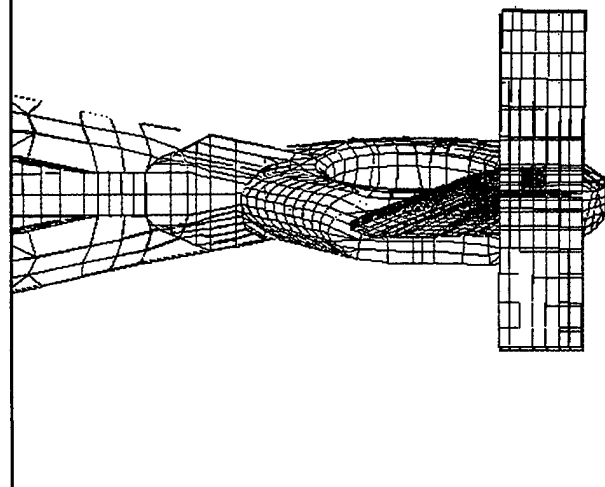
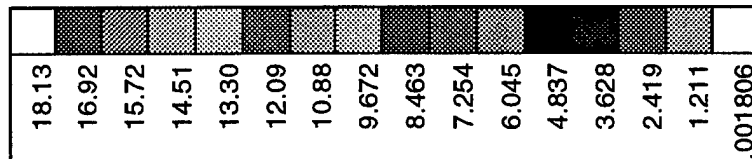
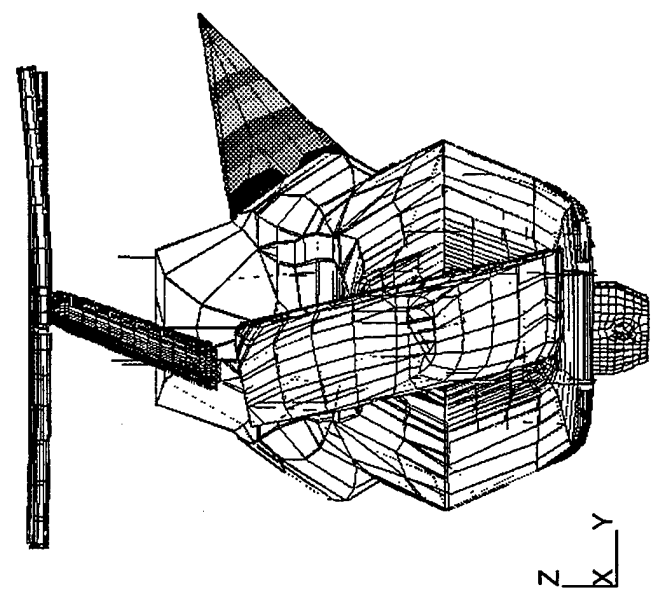
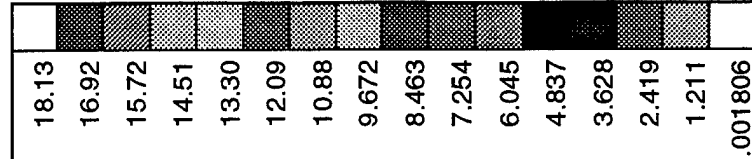
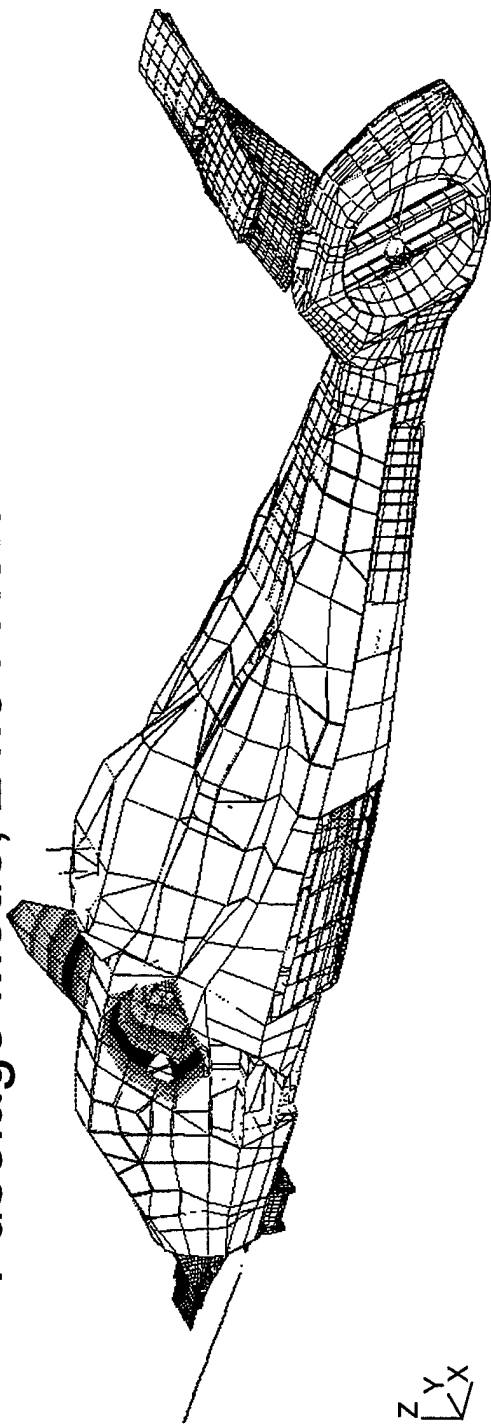
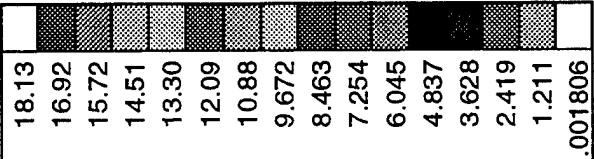
Z
Y
X

5.894
5.501
5.109
4.716
4.323
3.930
3.538
3.145
2.752
2.359
1.967
1.574
1.181
.7885
.3958
.003028

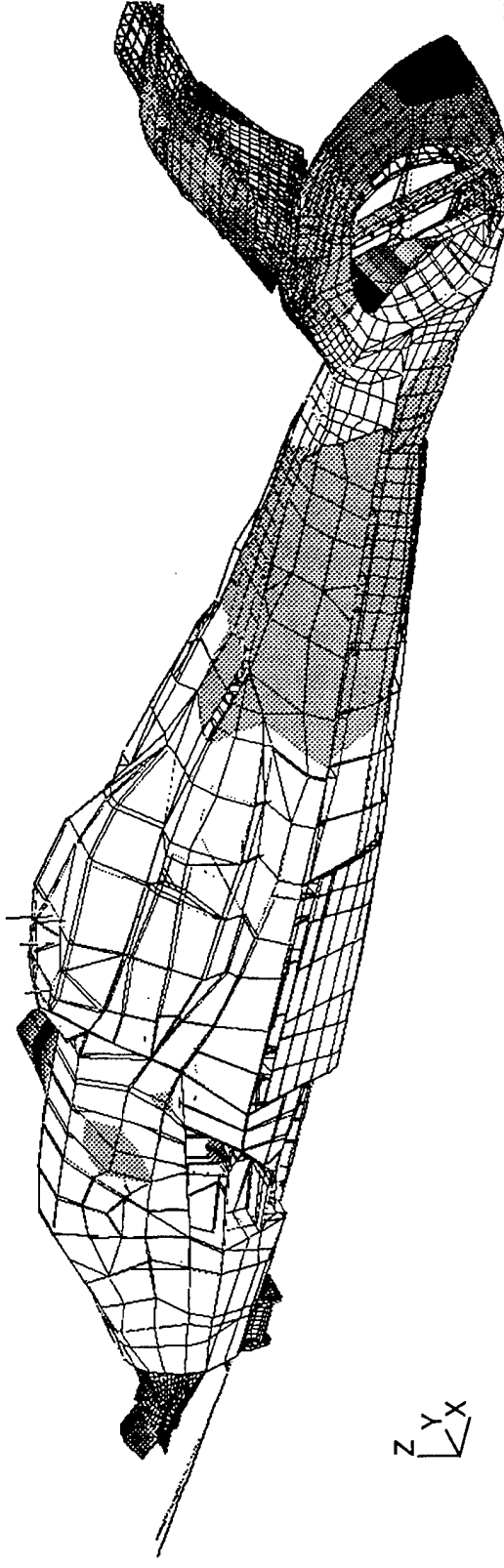


Z
Y
X

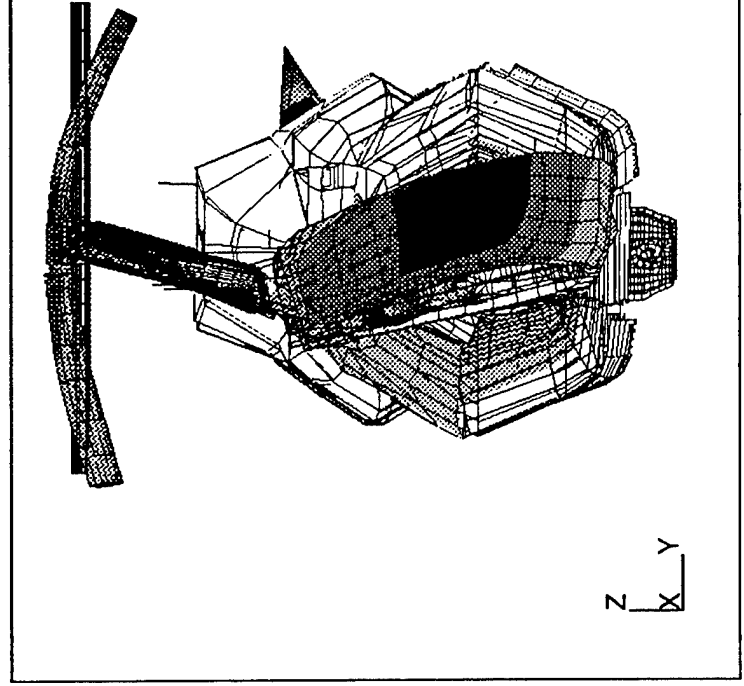
Fuselage Mode, 24.04 Hertz



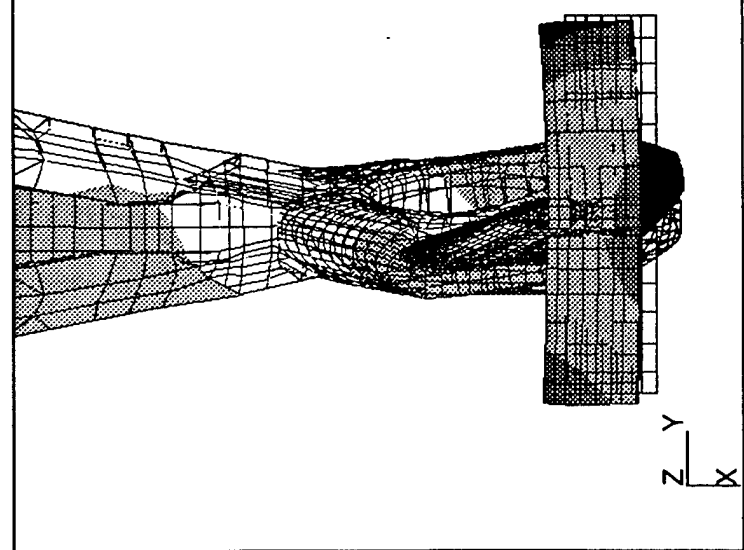
Horizontal Stab Vertical Bending Mode, 26.02 Hertz



7.622
7.114
6.607
6.100
5.592
5.085
4.578
4.070
3.563
3.056
2.548
2.041
1.534
1.027
.5193
.01196



7.622
7.114
6.607
6.100
5.592
5.085
4.578
4.070
3.563
3.056
2.548
2.041
1.534
1.027
.5193
.01196



7.622
7.114
6.607
6.100
5.592
5.085
4.578
4.070
3.563
3.056
2.548
2.041
1.534
1.027
.5193
.01196

APPENDIX D: ACCELEROMETER LOCATIONS & NASTRAN GRIDS

RAH66- MODEL J yrahj194.dat 4/17/98 sp
 COMPARISON OF KEY FLIGHT TEST LOCATIONS WITH SUGGESTED NASTRAN APPROXIMATE LOCATIONS

ITEM No.	LOCATION	Mnemonic	FLIGHT TEST Approximate Location			NASTRAN Location			NASTRAN GRID POINT
			STA mm	BL mm	WL mm	STA mm	BL mm	WL mm	
1	NOSE	VNOSE:D:300 LNOSE:D:300 LONOSE:D:300	5286.00	0.00	2720.00	5298.00	0.00	2720.00	61641
2	PILOT HEEL	LPHEEL:D:300 VPHEEL:D:300	6452.00	150.00	2720.00	6306.00	300.00	2720.00	6205
						6306.00	122.00	2720.00	6245
						6692.00	300.00	2720.00	6505
						6692.00	122.00	2720.00	6545
3	PILOT FLOOR	LPF:D:300 LOPF:D:300 VPF:D:300	7450.00	0.00	2720.00	7525.00	0.00	2720.00	7600
						7340.00	122.00	2720.00	7245
						7340.00	-122.00	2720.00	7246
						7525.00	110.00	2720.00	7645
						7525.00	-110.00	2720.00	7646
4	COPILOT HEEL	VCOPHEEL:D:300	7740.00	150.00	2980.00	7557.00	110.00	2838.00	7659
						7589.00	300.00	2956.00	7607
						7589.00	-300.00	2956.00	7608
						8084.00	300.00	3025.00	7907
						8084.00	-300.00	3025.00	7908
5	COPILOT FLOOR	VCOFF:D:300	8900.00	0.00	3130.00	9050.00	0.00	3160.00	9100
						8871.00	140.00	3135.00	8947
						8871.00	-140.00	3135.00	8948
						8960.00	140.00	3147.00	9047
						8960.00	-140.00	3147.00	9048
6	PILOT OVERHEAD	LPOVRHD:D:300	7420.00	0.00	4100.00	7349.00	176.00	4153.00	7513
						7349.00	-176.00	4153.00	7514
						7733.00	227.00	4229.00	7713
						7733.00	-227.00	4229.00	7714
7	COPILOT OVERHEAD	LCPOVRHD:D:300	8795.00	200.00	4200.00	8602.00	250.00	4323.00	8613
						8602.00	-250.00	4323.00	8614
						8849.00	251.00	4343.00	8713
						8849.00	-251.00	4343.00	8714
8	VERTICAL PYLON TOP	LVPYLNT:D:300	17737.00	185.00	5360.00	17737.10	151.15	5360.00	32338
						17737.10	159.90	5360.00	32341
						17743.30	162.40	5367.97	91225
						17715.30	164.67	5370.54	91236
9	HOR. STABILIZER LEFT TIP	VSTABTLT:D:300 LOSTABTL:D:300	17670.00	-1100.00	5463.00	17670.10	-1219.20	5463.39	41008
						17774.40	-1219.20	5463.20	41007
						17670.10	-1068.90	5463.39	41108
						17774.40	-1068.90	5463.20	41107
10	HOR. STABILIZER RIGHT TIP	VSTABTRT:D:300 LOSTABTR:D:300	17670.00	1580.00	5463.00	17670.10	1400.77	5463.39	49008
						17774.40	1400.77	5463.20	49007
						17666.70	1400.77	5374.97	49001
						17770.70	1400.77	5364.18	49002
11	HOR. STABILIZER VERTICAL BEND. LT SIDE	HBNORM1:D:300		-275.00		17670.10	-281.41	5463.39	43108
						17666.70	-281.41	5374.97	43101
						17982.30	-281.41	5444.27	43105
						17979.90	-281.41	5367.95	43104

Table D.1: Accelerometer - NASTRAN Locations.

ITEM No.	LOCATION	Mnemonic	FLIGHT TEST Approximate Location			NASTRAN Location			NASTRAN GRID POINT
			STA mm	BL mm	WL mm	STA mm	BL mm	WL mm	
12	HOR. STABILIZER VERTICAL BEND. LT SIDE	HBNORML2:D:300		-660.00	17670.10	-648.36	5463.39	42108	
					17666.70	-648.36	5374.97	42101	
					17982.30	-648.36	5444.27	42105	
					17979.90	-648.36	5367.95	42104	
13	HOR. STABILIZER VERTICAL BEND. RT SIDE	HBNORMR1:D:300		380.00	17670.10	341.60	5463.39	45308	
					17666.70	341.60	5375.00	45301	
					17982.40	415.31	5444.25	45305	
					17980.00	415.31	5367.95	45304	
14	HOR. STABILIZER VERTICAL BEND. LT SIDE	HBNORMR2:D:300		770.00	17670.10	656.83	5463.39	46008	
					17666.70	656.83	5374.97	46001	
					17982.60	656.83	5444.24	46005	
					17979.90	656.83	5367.95	46004	
15	HOR. STABILIZER EDGE BEND. LT SIDE	HBEDGEL1:D:300		-240.00	17670.10	-281.41	5463.39	43108	
					17666.70	-281.41	5374.97	43101	
					17982.30	-281.41	5444.27	43105	
					17979.90	-281.41	5367.95	43104	
16	HOR. STABILIZER EDGE BEND. RT SIDE	HBEDGER1:D:300		350.00	17670.10	341.60	5463.39	45308	
					17666.70	341.60	5375.00	45301	
					17982.40	415.31	5444.25	45305	
					17980.00	415.31	5367.95	45304	
17	LT AFT SHROUD/V.TAIL INTERFACE FITTING	VSAFTS1:D:300			17002.00	-294.50	4400.00	21326	
18	RT AFT SHROUD/V.TAIL INTERFACE FITTING	VSAFTS2:D:300			17002.00	-176.00	4400.00	21327	
19	LT FWD SHROUD/V.TAIL INTERFACE FITTING	VSFFTS1:D:300			16635.00	-294.50	4400.00	24621	
20	LT AFT SHROUD/V.TAIL INTERFACE FITTING	VSFFTS2:D:300			16635.00	-176.00	4400.00	24620	
21	FWD H. STAB/V.TAIL FITTING CL	DHSTABMX:D300 DHSTABMZ:D300 DHSTABVZ:D300			17730.00	62.85	5404.00	32391	
					17730.00	151.15	5404.00	32394	
					17737.10	104.55	5360.00	32336	

Table D.2: Accelerometer - NASTRAN Locations.

APPENDIX E: LOAD CALCULATIONS PROGRAM

```
% ff_solve_nonsym_inter.m
% Program that solves for the forcing functions, in PSD by using the
% techniques discussed by Bendat and Pierson for multiple input
% single output

%  $G_{xx} = (H_{xy}^*)^{-1} * G_{yy} * (H_{xy})^{-1}$ 

% First must identify the location (nodes) of the forcing function
% the location of the response (nodes), and the direction of the
% response

% The directions are somewhat backwards - due to the way I had Nastran
% write out the punch files ( which became .mat files)

% x = 3 (longitudinal)
% y = 2 (lateral)
% z = 1 (vertical)

% The response data uses the following script:
% First is node in Nastran Mode.1, next is direction and last is the
% pointer into the psd matrix (which column)

ncl = [61641 2 1]; % Nose Cone Lateral
phl = [6505 2 2]; % Pilot Heel Lateral
pfl = [7246 2 3]; % Pilot Floor Lateral
pol = [7514 2 4]; % Pilot Overhead Lat
cpol = [8614 2 5]; % CPG Overhead Lat
ncv = [61641 1 6]; % Nose Cone Vertical
pfv = [7246 1 7]; % Plt Floor Vertical
vptl = [32341 2 8]; % Vert Pylon Top Lat
hrtv = [48108 1 9]; % HorStab Rt Tip Vert
hltv = [41108 1 10]; % HorStab Lt Tip Vert
hrtlo = [48108 3 11]; % HorStab Rt Tip Long
hltlo = [41108 3 12]; % HorStab Lt Tip Long

% Use the following format to enter the input-ouput locations and
% specify which run set

run = 24;
%no_fft = 4096;

% force = [32311 46008 ]
% response = [ pol
%             phl];

force = [ 42008 44008 46008 31844 31840 31836 ];
```

```

response = [ phl
             pfv
             cpol
             ncl
             ncv
             vptl
             hrtv
             hltv
             hrtlo
             hltlo ];

% Assumptions is that loads are correlation - are the loads correlated?

% If the loads are completely uncorrelated then set corr = 0
% If it is something inbetween then define the matrix relate

force_corr = 1;
response_corr = 1;

% Use the following format for relate - forcing function(load) to load
% (which are correlated)
% force_relate = [1 1 0
%                1 1 0
%                0 0 1] This tells us force 1 is related to force 2,
% all others are not

% force_relate = [1 0
%                0 1];

% Load the frequency response function matrix
% Counter to use for matrix index

k = 0;

[no_row,force_num] = size(force);
[response_num,no_col] = size(response);

for f = 1:force_num

    % frf file must have the name format frfnode

        for r = 1:response_num
            k = k+1;
            eval(['load frf',num2str(force(1,f)),'; '])
            eval(['frf_sel = frf_',num2str(response(r,1)),'; '])
            y = [(frf_sel(:,1) + frf_sel(:,2) .*i) (frf_sel(:,3) +
                frf_sel(:,4) .*i) (frf_sel(:,5) + frf_sel(:,6) .*i)];
            H(:,k) = y(:,response(r,2));
        end

end

```

```

% H (frf matrix has now been loaded in the following format; from our
% example nodes -
% H = [H11 H12 H13 H21 H22 H23 H31 H32 H33];
%

% Because of the weird way I saved the pch files, the vector {time} is
% actually frequency

% Now we need to load the response data from the PSD and CSD we have
% done before

eval(['load psd_run',num2str(run),'; '])

    if exist ('no_fft') == 1
        eval(['load psd_run',num2str(run),'_',num2str(no_fft),'; '])
    end

k = 0;

for f = 1:response_num

    for r = 1:response_num
        k = k+1;
        if f == r
            G(:,k) = psd_run24(:,response(r,3));
        else
            eval(['G(:,k) = ...
            csd_run24_',num2str(response(f,3)),':(:,response(r,3)); '])
        end
    end

end

% Form the Hxy and Gyy matrix for each individual frequency,
% solve for Gxx
% and save in another matrix

kk = 0;

start_freq = 5.50;
end_freq = 24.00;

[f_diff,f_index_start] = min(abs(start_freq - F));
[f_diff,f_index_end] = min(abs(end_freq - F));

for ff = f_index_start : f_index_end

G_count = 0;
k = 0;
kk = kk + 1;

    for l = 1:response_num
        for m = 1:response_num

```

```

% Load the Gyy square matrix
Gyy(l,m) = G(ff,G_count+m);
end
G_count = G_count + response_num;
end

for l = 1:force_num
for m = 1:response_num

% Load the Hxy square matrix
[min_dif,val_index] = min(abs(F(ff) - time'));
% Cubic Spline Interpolation
% Hxy(l,m) = interp1(time,H(:,k+m),F(ff),'spline');
% Linear Interpolation
% Hxy(l,m) = interp1(time,H(:,k+m),F(ff),'spline');
end

k = k + response_num;
end

if exist('force_relate') == 1
Hxy = force_relate .* Hxy;
end

if exist('response_relate') == 1
Gyy = excite_relate .* Gyy;
end

if response_corr == 0
Gyy = eye(size(Gyy)) .* Gyy;
end

% Now we have to solve for the Gxx matrix via the technique
% discussed above

if force_corr == 0 & response_corr == 0
Gyy = diag(Gyy);
Gxx = ((abs(Hxy')).^2) \ Gyy;
else
Gxx = Hxy' \ Gyy / Hxy;
end

% Saving the output data Gxx to a matrix of the following form
% Gxx = [G11 G12 G13 G21 G22 G23 G31 G32 G33]
% Also outputs a vector, Freq, that has the frequencies
% each row represents

[Gxx_row,Gxx_col] = size(Gxx);

if Gxx_col == 1
G_output(kk,:) = Gxx';

else
k = 0;

```

```
    for ll = 1:Gxx_row
      for mm = 1:Gxx_col

        G_output(kk,k+mm) = Gxx(ll,mm);
      end
      k = k+ force_num;
    end
  end
  frequency(kk) = F(ff);
  cond_Hxy(kk) = cond(Hxy);
  rank_Hxy(kk) = rank(Hxy);
end

big_Kahuna = [frequency' G_output cond_Hxy' rank_Hxy'];
```


LIST OF REFERENCES

1. *Performance Weapon System Specification: Helicopter, Light/Attack Reconnaissance Helicopter, RAH-66*. Headquarters, Department of the Army, Washington, D.C. 1996.
2. Wood, E. R. Class Notes: "An Introduction to Helicopter Dynamics." *An Introduction to Helicopter Engineering*. Naval Postgraduate School, Monterey, CA. May 1997.
3. Helicopter Program (LH). *Air Vehicle Characteristics, Vibration and Dynamics*. United Technologies Sikorsky Aircraft, Stratford, CT. 1987.
4. Leishman, J. and Moedersheim, E. "Investigation of Aerodynamic Interactions Between a Rotor and a T-Tail Empennage," *Journal of the American Helicopter Society*. January 1998. Pp. 37-46.
5. Schlichting, H. *Boundary Layer Theory*. McGraw Hill Book Company. New York, NY. 1979.
6. Small, J. Hebbbar, S. and Platzler, M. *AIAA Report 92-0155: Flow Visualization and Wake Analysis for Complex Three-Dimensional Bluff Bodies at Subcritical through Critical Reynolds Numbers*. Naval Postgraduate School, Monterey, CA. January 1992.
7. Thomson, W. T. *Theory of Vibration With Applications*. Prentice-Hall Inc. Upper Saddle River, NJ. 1998.
8. Bendat, J. S. and Piersol, A. G. *Random Data, Analysis and Measurement Procedures*. John Wiley and Sons, Inc. New York, NY. 1986.
9. Gordis, J. H. Class Notes: ME4522 Shipboard Vibration and Noise. Naval Postgraduate School, Monterey, CA. October 1997.

10. *MSC/NASTRAN Quick Reference Guide, Version 70*. Reymond, M. and Miller, M., Ed. MacNeil-Schwendler Corporation. Los Angeles, CA. 1997.
11. *Craig, R. R. Jr. Structural Dynamics, An Introduction to Computer Methods*. John Wiley and Sons, Inc. New York, NY. 1981.
12. Tobin, V. *Analysis of Potential Structural Design Modifications for the RAH-66 Comanche Helicopter*. Masters' Degree Thesis. Naval Postgraduate School, Monterey, CA. June 1997.
13. Shoop, B. *Structural Design Analysis of the Tail Landing Gear Bay and the Vertical/Horizontal Stabilizers of the RAH-66 Comanche Helicopter*. Masters' Degree Thesis. Naval Postgraduate School, Monterey, CA. September 1997.

INITIAL DISTRIBUTION LIST

	No. Copies
1. Defense Technical Information Center.....	2
8725 John J. Kingman Rd., STE 0944	
Fort Belvoir, VA 22060-6218	
2. Dudley Knox Library.....	2
Naval Postgraduate School	
411 Dyer Rd.	
Monterey, CA 93943-5101	
3. Department of Aeronautics and Astronautics, Code AA.....	2
Naval Postgraduate School	
Monterey, CA 93943-5000	
4. Professor E. Roberts Wood, Code AA/Wd.....	3
Department of Aeronautics and Astronautics	
Naval Postgraduate School	
Monterey, CA 93943-5000	
5. Professor Donald A. Danielson, Code MA/Dd.....	1
Department of Mathematics	
Naval Postgraduate School	
Monterey, CA 93943-5000	
6. Professor Joshua H. Gordis, Code ME/Go.....	1
Department of Mechanical Engineering	
Naval Postgraduate School	
Monterey, CA 93943-5000	

7. Robert L. Tomaine.....1
Comanche Program Manager's Office
Attn.: SFAE-AV-RAH-TV (Tomaine)
Redstone Arsenal - Bldg. 5681
Huntsville, AL 35898-5000
8. Robert Blackwell.....1
103 Old Zoar Road
Monroe, CT 06468-1435
9. MAJ Patrick H. Mason.....1
102 Kettering Drive
Hunstville, AL 35824